Developments of Thick-Metal Inductors and Applications to Reactive Lumped-Element Low-pass Filter Circuits

A Thesis Submitted to the

College of Graduate Studies and Research

in Partial Fulfillment of the Requirements for the Degree of

Master of Science

in the Department of Electrical and Computer Engineering

University of Saskatchewan

Saskatoon, Saskatchewan

by

Edwin G. Gono Santosa

November 2009

PERMISSION TO USE

In presenting this thesis in partial fulfillment of the requirements for a Postgraduate degree from the University of Saskatchewan, I agree that the Libraries of this University may make it freely available for inspection. I further agree that permission for copying of this thesis in any manner, in whole or in part, for scholarly purposes may be granted by the professor who supervised my thesis work or, in his absence, by the Head of the Department or the Dean of the College in which my thesis work was done. It is understood that any copying or publication or use of this thesis or parts thereof for financial gain shall not be allowed without my written permission. It is also understood that due recognition shall be given to me and to the University of Saskatchewan in any scholarly use which may be made of any material in my thesis.

Requests for permission to copy or to make other use of material in this thesis in whole or in part should be addressed to:

Head of the Department of Electrical and Computer Engineering
57 Campus Drive
University of Saskatchewan
Saskatoon, Saskatchewan, Canada
S7N 5A9

ABSTRACT

Strong demands for smaller, cheaper, and multifunction wireless systems have put very stringent requirements on passive devices, such as inductors and capacitors. This is especially true considering the size and weight of most radio frequency (RF) transceivers are mainly due to passives. RF micro-electro-mechanical-systems (MEMS) passives are addressing this issue by offering lower power consumption and losses, higher linearity and quality (Q)-factors, potential for integration and miniaturization, and batch fabrication. These advantages position RF MEMS passives as good candidates to replace conventional passives. Further, they also open an opportunity for using the passives as building blocks for lumped element-based RF circuits (e.g. filters, couplers, etc.) which could replace the more-bulky distributed-element circuits.

This thesis presents the design, simulation, fabrication using the deep X-ray lithography process, and testing of thick-metal RF inductors and their applications to lumped-element low-pass filter (LPF) circuits. The 70-μm tall single-turn loop inductors are structurally compatible to a pre-existing RF MEMS capacitor concept and allow the two device types to be fabricated together. This compatibility issue is crucial if they would be used to construct more complex RF circuits.

At a 50-Ω inductive reactance point, test results show Q-factors of 17- 55, self-resonant frequencies (SRF) exceeding 11 GHz, and nominal inductances of 0.4- 3 nH for 1-loop inductors and Q-factors of 11- 42, SRFs of 4- 22 GHz, and inductances of 0.8- 5.5 nH for 2-loop inductors. Further, test results reveal that high conductivity metals improve the Q-factors, and that low dielectric-constant substrates increase the SRFs.

In terms of LPFs, measurements show that they demonstrate the expected third-order Chebyshev response. Two nickel filters on a quartz glass substrate show a

0.6-dB ripple with 3-dB frequencies (f_{3dB}) of 6.1 GHz and 11.9 GHz respectively. On an alumina substrate, they exhibit a 1.4-dB ripple with f_{3dB} of 5.4 GHz and 10.6 GHz respectively. The filters are 203- 285 μm tall and feature 6- 6.5 μm wide capacitance air gaps. These dimensions are different than the original designs and the filter performances were shown to be somewhat sensitive to these discrepancies. Compared to a distributed approach, the lumped-element implementations led to an area reduction of up to 95%.

ACKNOWLEDGEMENTS

I owe my deepest gratitude to my supervisor, Dr. David M. Klymyshyn for his support and assistance during my M.Sc program at the University of Saskatchewan. Dr. Klymyshyn has guided me throughout the research and preparation of this thesis with his patience and knowledge while still giving me the opportunity to work in my own way. It has been a privilege to work under him. I would also like to thank Dr. Ron Bolton, Dr. Sven Achenbach, Dr. Anh Dinh for serving as my advisory committee and Dr. Ikechukwuka Oguocha for serving as my external examiner.

I would like to thank all personnel at the Institute for Microstructure Technology (IMT), Karlsruhe Institute of Technology in Germany, in particular Dr. Martin Börner, for making possible the fabrication of my inductor and low-pass filter designs.

I am grateful for the financial support, personnel, and research equipments that TRLabs has generously provided. In particular, I would like to thank Darcy Haluzan and Garth Wells for their contributions to the testing of the devices.

Finally, I would like to extend my heart-felt gratitude to my parents, Budiono Gono Santosa and Mulianingsih Tanu, my sister, Karina Kurniasih, and my friends, in particular Monica Purnama, for their persistent encouragement and support throughout my M.Sc program.

TABLE OF CONTENTS

LIST OF TABLES

LIST OF FIGURES

LIST OF ABBREVIATIONS

ADS	Advance Design System
BST	barium strontium titanate
C	capacitance
CPW	coplanar waveguide
DGS	defected ground structure
DXRL	deep X-ray lithography
f_{ripple}	frequency of the last pass-band ripple point
$f_{3\text{dB}}$	frequency when $\|S_{21}\|$ is equal to -3 dB
GMD	geometric mean distance
GSG	ground-signal-ground
HF	hydrofluoric
HFSS	High Frequency Structure Simulator
IMT	Institute for Microstructure Technology
ISS	impedance standard substrate
L	inductance
LIGA	German acronym for Lithografie, Galvanoformung, Abformung
LPF	low-pass filter
MEMS	micro-electro-mechanical systems
MIM	metal-insulator-metal
MOS	metal-oxide-semiconductor
OCPW	overlay coplanar waveguide
OPS	oxidized porous silicon
PEC	perfect electric conductor
PMMA	poly(methyl methacrylate)

Q	quality factor
R	resistance
RF	radio frequency
SiO_2	silicon dioxide
SEM	scanning electron microscope
SOL	short-open-load
SOLT	short-open-load-thru
SRF	self-resonant frequency
VNA	vector network analyzer
XRL	X-ray lithography

1. INTRODUCTION

1.1 Motivation

A large portion of most radio frequency (RF) transceivers is composed of passive devices [1] such as inductors and capacitors. Strong demands for smaller, cheaper, multifunction, and multiradio wireless systems have put more stringent requirements on passives. RF micro-electro-mechanical-systems (MEMS) passive devices are addressing this issue by offering lower power consumption, lower losses, higher linearity, higher Q-factors, potential for integration and miniaturization [2], and cost-effective batch fabrication. All these advantages position RF MEMS passives as good candidates to replace conventional passive devices, such as the ones produced using silicon technology.

Many RF circuits, such as filters, diplexers, and couplers, use distributed passive elements where physical size is wavelength-dependent which tends to make the circuit size big (mm to cm range). Such RF circuits are not the ideal choices for small, multifunction wireless systems and can really benefit from miniaturization through lumped element-based implementations [3, 4, 5, 6]. This provides an opportunity for RF MEMS passives to make another valuable contribution, namely, using these passives to produce compact and highly-integrated lumped element-based circuits as possible replacements for the more bulky distributed element-based RF circuits. However, to be considered as viable replacements, lumped-element RF circuits need to contain structurally compatible inductors and capacitors and also have comparable performances to that of the distributed circuits.

Common approaches for realizing RF capacitors and inductors are often based on surface or bulk micromachining [7], adopted from silicon technology. The silicon

technology is a matured technology, one in which significant expertise and resources are already available. Therefore, using techniques from the silicon technology, in an attempt to leverage mainstream fabrication process, to produce RF MEMS devices does make sense. Unfortunately, these approaches have a couple of limitations such as limited choice of substrate material and limited metal thickness, constraining the devices to planar 2D geometries. A different approach in realizing RF MEMS passive devices is to use the vertical dimension. The use of the vertical dimension reduces the lateral physical size of the devices, saving lateral space and allowing operation at higher frequencies. One of the best techniques for producing very tall structures is deep X-ray lithography (DXRL) and subsequent metal electroplating.

1.2 LIGA/DXRL Process

In 1975, Romankiw *et al.* of IBM combined X-ray lithography and electroplating to produce gold structures with high aspect ratios (ratio of the maximum height to the minimum horizontal dimension of a structure) [8]. The requirement for an X-ray radiation source made this procedure expensive and less ideal for large-scale production. In an effort to bring down the fabrication cost, Ehrfeld *et al.* at the Karlsruhe Nuclear Research Centre (now Karlsruhe Institute of Technology) added a third procedure known as plastic molding that allows, in principle, large-scale production [9, 10]. The combination of the three procedures was then called LIGA, a German acronym for X-ray lithography (X-ray Lithographie), electroplating (Galvanoformung), and molding (Abformung) [11]. X-ray lithography typically uses X-rays with a wavelength of $0.2 - 1$ nm as a radiation source. However, the desire to produce deep trenches and 3D structures calls for X-ray radiations with more penetrating capability, leading to the use of X-rays with higher energies and shorter wavelengths on the order of 0.1 nm in a process known as deep X-ray lithography (DXRL).

The deep X-ray lithography/electroplating process starts with the application of a thin metal film on a substrate. This metal film is known as the seed layer and serves as the cathode in the subsequent electroplating procedure. When the

substrate is metallic, the seed layer requirement can be omitted. Next, a thick X-ray sensitive layer is applied on top of the seed layer. There are two types of X-ray resist, namely, *negative* and *positive resist*. Upon exposure to X-ray radiation, a negative resist hardens and becomes less soluble in a suitable developer, while the opposite is true for a positive resist. Examples of negative and positive resists are SU-8 and Poly(methyl methacrylate) (PMMA) respectively. The resist layer is then exposed to an X-ray radiation through a mask, which can be made of gold absorbers on a titanium mask membrane. Some of the X-ray radiation is absorbed by the gold absorbers while some passes through the X-ray-transparent areas of the mask and reaches the resist. In the case of PMMA, upon reaching the resist, the X-ray radiation is absorbed, leading to chemical-bond scission in the molecular chain of the polymer and thus, making it soluble in a suitable developer. The sample is then developed to remove the exposed resist. The resulting three-dimensional resist structure is electroplated with a metal to fill the void spaces in the resist. Once the electroplating is done, the remaining resist is removed by X-ray flood irradiation, followed by another step of resist development. To produce free-moving or electrically isolated components, the metal seed layer is then locally etched away using either wet or dry etching process [12]. If desired, multiple copies of the primary components obtained from the DXRL/electroplating procedures can be generated in a cost-effective manner using one of the molding techniques: hot embossing or injection molding. Details of these techniques can be found in [11].

Due to the application of an extremely parallel and highly penetrating X-ray radiation, the deep X-ray lithography, as an integral part of the complete LIGA process, has the ability to produce vertical structures with aspect ratios of up to 100 [13, 14]. As a comparison, deep ultraviolet lithography process typically gives an aspect ratio of about 22 [8]. In addition, the DXRL process is also capable of producing sidewalls with slopes better than 89.9° [15, 16] and surface roughness, R_a, of less than 50 nm [15, 17]. It also stands out with its achievable minimum feature size in the sub-micrometer range.

The unique capability of DXRL to produce tall vertical structures is beneficial in

the realization of passive devices/circuits [12, 16, 18, 19, 20, 21]. In [18], a vertical RF MEMS variable capacitor was successfully realized and its top view is shown in Figure 1.1. The vertical parallel-plate capacitor is 100-μm tall and features a thin movable cantilever beam and a capacitance gap of 2.5 μm. The 0.8-pF capacitor operates in the 1-5 GHz range and has a capacitance ratio of 1.24:1 over a 20-V tuning range. Benefiting from a vertical architecture, it has quality (Q) factors of 133 and 36 at 2 and 4 GHz respectively and shows good RF performance. However, the compelling use of this capacitor in compact, integrated, reactive lumped-element circuits calls for structurally compatible inductors.

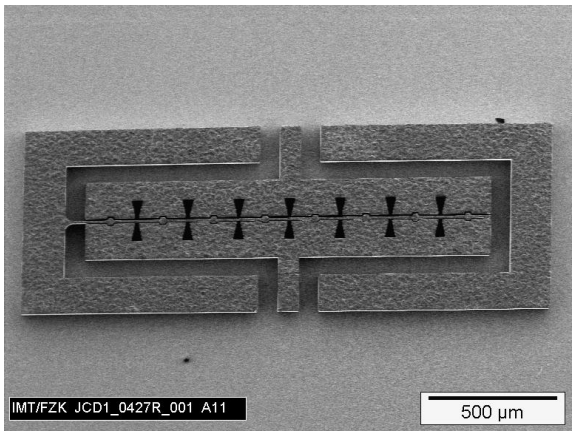

Figure 1.1. Vertical capacitor fabricated using DXRL [18].

1.3 Literature Review of Inductors

Conventionally, on-chip RF inductors were realized as planar multi-turn spirals or meander structures [22, 23] using a thin metal layer on a semiconductor substrate. Unfortunately, they suffered from metal and substrate losses and parasitic capacitances which resulted in relatively low Q-factors and low self-resonant frequency (SRF) [24, 25]. Recent progress in micro-fabrication techniques has led to new approaches in RF inductor design to address these limitations.

A relatively simple technique to produce a high Q-factor inductor is to use a thicker metal layer such as demonstrated by Choi *et al.* [26]. Choi *et al.* reported that the Q-factor of a 5-nH spiral inductor increased from 40 to 50 and to about 57 when the copper metal thickness was increased from 5 μm to 10 μm, and to 20 μm respectively.

Another technique is to use a thick insulating layer between the inductor and the semiconductor substrate such as shown in [27, 28]. Rais-Zadeh *et al.* [27] reported that the maximum Q-factor for a 1-nH inductor increased from approximately 40 at 1 GHz to about 49 at 1.5 GHz when the thickness of silicon dioxide insulating layer was increased from 4 to 20 μm.

A different technique is to create an air gap between the inductor and the substrate, either by partially removing the substrate underneath the inductor, such as [29, 30], or by suspending the inductor above the substrate [31, 32]. Reference [30] developed a 2-nH nickel spiral inductor on top of a 25-μm-deep trench in the silicon substrate with a peak Q-factor of 12 at 4 GHz and SRF of 9.8 GHz. Using an SU-8 UV lithography process, Park *et al.* [32] developed a 3.1-nH inductor, suspended 50-μm above a silicon substrate with a peak Q-factor of 13 at 1.7 GHz and SRF of 17 GHz.

A more advanced technique is to tilt the inductor away from the substrate to make the magnetic fields parallel to the substrate. Lubecke *et al.* [33] developed a semi-vertical-positioned 1.2-nH inductor with a Q-factor of 13 and SRF exceeding 20 GHz. Using a similar concept, Zou *et al.* [34] also observed an improvement in the peak Q-factor and SRF of his vertically-tilted inductor design.

Many of the existing RF inductors are of the multi-turn spiral inductor type. While the multi-turn spiral design enhances magnetic flux, it requires a connection to its centre using an overpass (or underpass) or a wire bond, which, unfortunately, introduces parasitic capacitances. A meander-type inductor does not have this problem, but it suffers from a negative mutual inductance between adjacent turns, lowering its inductance [35]. In terms of Q-factor and SRF enhancements, suspending or tilting the inductors off the substrate have been shown to be helpful. Unfortunately,

the majority of the existing inductor designs require multiple metal-deposition steps and/or etching of the substrate. This not only complicates the inductor fabrication process but also leads to non-structurally compatible inductors to the pre-existing capacitor concept presented earlier.

Therefore, there is a need for an RF inductor, with a relatively high Q-factor and SRF, that can be realized using a single metal-deposition step without the need for an overpass or wire bond connection. Such a design will make the inductor structurally compatible to the pre-existing capacitor concept presented earlier and allow the two types of devices to be fabricated together using a simple single metal layer, common-height process.

1.4 Literature Review of Low-pass Filters

Conventionally, RF low-pass filters (LPF) were widely implemented using shunt open stubs [36, 37] or stepped impedance transmission lines [38]. In [36] the authors presented a 5^{th}-order Chebyshev LPF with a pass-band ripple of 1.5 dB and a 3-dB cut-off frequency of $f_{3\text{dB}}$= 3 GHz using shunt open coplanar waveguide (CPW) stubs. In [38] the authors developed stepped impedance Butterworth low-pass filters with $f_{3\text{dB}}$= 9.2 GHz and 12.7 GHz using thick microstrip lines. Since these two approaches are transmission-line based, the size of the filter circuits is rather big (mm to cm range). This can be worse in microstrip filters, since they normally require certain substrate area in their surroundings to accomodate some fringing fields. In addition to the size, transmission line-based filters typically consist of high-impedance lines. These high-impedance lines typically appear as narrow transmission lines, which tends to limit the power handling capability and can be challenging to fabricate.

Fairly recently, defected ground structures (DGS) have been added to the conventional transmission line low-pass filters as an effort to address the size issue. A dumbbell-shape DGS section gives rise to increasing effective capacitance and inductance of a standard transmission line and can be represented by an LC equivalent circuit and provide a cut-off frequency as well as attenuation poles at a certain frequency. Using a T-junction microstrip line with a couple of DGS sections having

different dimensions, Ahn *et al.* [39] developed a three-pole low-pass filter with 0.01-dB ripple and an f_{3dB}= 1.3 GHz. The three-pole LPF using DGS concept is then extended to a five-pole DGS LPF by Lim *et al.* in [40]. In addition to the reduction in size, transmission line low-pass filters with DGS do not require high-impedance lines. Consequently, wider transmission lines can be used which simplifies the fabrication and increases the power-handling capability of the filters [40]. Additional efforts using this approach can be found in [41, 42].

In [43], Kim *et al.* also used DGS but in combination with an overlay coplanar waveguide (OCPW). In the OCPW, the edge of the signal line is extended partially above both ground structures to distribute the electric field in the overlap region, reducing conductor and substrate losses of the CPW. Kim *et al.* argue that OCPW line together with necessary DGS sections can realize a low-impedance line with slow wave effect, reducing the length of the low-impendence line. Using this approach, Kim *et al.* developed a five-section stepped-impedance LPF with an f_{3dB} of about 3.7 GHz. The proposed filter occupied an area of (1.56 x 3.34) mm^2 compared to (1.56 x 4.52) mm^2 of a similar LPF without the OCPW.

While DGS has been shown to be useful in reducing circuit size, the use of lumped elements as building blocks for low-pass filters is also an efficient way to reduce the circuit size [43]. An example of the lumped-element approach can be found in [44] in which the authors present a five-pole Butterworth LPF using lumped-element inductors and metal-oxide-semiconductor (MOS) capacitors. The LPF had a 3-dB frequency of f_{3dB}= 845 MHz with a mid-band insertion loss of 2.4 dB. More recently, Fang *et al.* [45] developed a higher cut-off frequency lumped-element low-pass filter. The third-order low-pass filter employed planar spiral inductors and a metal-insulator-metal (MIM) capacitor on a silicon substrate that was locally modified with oxidized porous silicon (OPS) technology. The low-pass filter occupied an area of (1350 x 550) μm^2 and had an f_{3dB}= 2.9 GHz and a mid-band insertion loss of 0.87 dB.

Despite some lumped-element low-pass filter designs, the majority of the RF low-pass filters are still distributed circuits where physical size is wavelength-dependent.

This tends to make the circuit size big (mm to cm range). On the other hand, trends toward smaller, cheaper, and more multifunction wireless products put severe limitations on chip area. Therefore, there is much potential for lumped-element low-pass filters.

1.5 Objectives

This research aims to realize a lumped-element low-pass filter using the deep X-ray lithography (DXRL) process. The concept of the pre-existing vertical RF MEMS capacitor [18] shown earlier would be adopted and structurally compatible thick-metal inductors would be introduced. These two types of devices would then be used as building blocks for the lumped-element low-pass filter. The specific objectives of the research are as follow.

1. To develop a thick-metal inductor which is structurally compatible with the pre-existing vertical capacitor [18] concept. The inductor design should allow both device types to be fabricated together using a simple, single metal layer, common height DXRL process.

2. To develop a lumped-element low-pass filter which would incorporate the structurally compatible inductor and capacitor elements. The low-pass filter would have a 3^{rd}-order 0.5-dB ripple Chebyshev response and operate in the 1-10 GHz range. A 3^{rd}-order filter circuit is chosen because it offers sufficient complexities to demonstrate the concept of using both the inductor and capacitor elements in realizing a lumped-element low-pass filter circuit.

3. To fabricate both the inductor and low-pass filter designs using the deep X-ray lithography process.

4. To test the inductors and low-pass filters and compare the results against simulated results.

1.6 Thesis Organization

This thesis consists of six chapters. Chapter 1 provides an introduction to the research. This mainly consists of the motivations, brief history/overview of the deep X-ray lithography process, and literature reviews of inductors and low-pass filters. Chapter 2 presents background theories related to inductors and Chebyshev low-pass filters. Chapter 3 illustrates the parasitic effects on the general performance of an inductor and low-pass filter. Chapter 4 describes the design and fabrication details of the inductor and low-pass filter. Chapter 5 presents the simulation and test results of both the inductor and low-pass filter. Finally, Chapter 6 provides conclusions determined from the research along with suggestions for future work.

2. BACKGROUND THEORY

2.1 Loop Inductors

2.1.1 Inductor Principle

An inductor is an electronic device that stores energy from a magnetic field and it can be thought of as the magnetic counterpart of a capacitor [46]. Assume the two wire loops, C_1 and C_2, in Figure 2.1 are in free space.

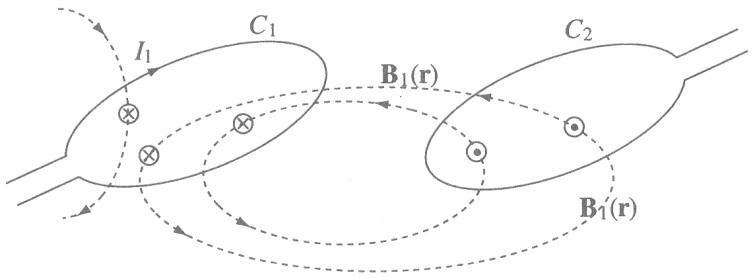

Figure 2.1. Loop C_1 produces magnetic flux part of which passes through C_2 [47].

If a steady current I_1 flows in loop C_1, a magnetic flux density B_1 is produced around loop C_1. Since loop C_1 produces B_1, all flux lines pass through loop C_1, but only some of them actually pass through loop C_2. Assuming B_1 is known, the magnetic fluxes can be found as follows [47]:

$$\psi_{11} = \int_{S_1} B_1 \bullet dS_1 \tag{2.1}$$

$$\psi_{12} = \int_{S_2} B_1 \bullet dS_2 \tag{2.2}$$

where, ψ_{11} is the magnetic flux, produced by loop C_1, that passes through loop C_1 (Wb), ψ_{12} is the magnetic flux, produced by loop C1, that passes through loop C_2 (Wb), B_1 is the magnetic flux density produced by loop C_1 (T), and S_1 and S_2 are the surface areas of loop C_1 and C_2 respectively (m^2).

If the current I_1 is assumed to be constant, the Biot-Savard law gives [48]:

$$B_1 = I_1 \left(\frac{\mu_0}{4\pi} \oint_{loop} \frac{\mathrm{d}\mathbf{L} \times \mathbf{R}}{|\mathbf{R}|^3} \right) \tag{2.3}$$

where d$\mathbf{L}$ is a differential current element along the wire and $\mathbf{R}$ is the position vector of the point at which B_1 is evaluated.

If the flux density B_1 from equation (2.3) is substituted into equation (2.1) and (2.2) and the corresponding integrations are performed, the results are the magnetic fluxes ψ_{11} and ψ_{12} that are proportional to current I_1:

$$\psi_{11} = L_{11} I_1 \tag{2.4}$$

$$\psi_{12} = M_{12} I_1 \tag{2.5}$$

The constant L_{11} is referred to as the *self-inductance* of loop C_1, while M_{12} is known as the *mutual inductance* between loop C_1 and C_2 and can be defined as

$$L_{11} = \frac{\psi_{11}}{I_1} \tag{2.6}$$

$$M_{12} = \frac{\psi_{12}}{I_1} \tag{2.7}$$

The unit of inductance is known as the Henry (H). Notice that inductance (self or mutual) is a parameter that depends only on the geometrical configuration of the inductor [47].

2.1.2 Loop Inductor Model

It is desirable to be able to physically model the inductors using lumped elements. A lumped-element inductor model reduces the electromagnetic field analysis complexity and is helpful in understanding the effects of various losses and parasitics on the inductor performance, such as quality (Q)-factor and self-resonant frequency.

However, from the accuracy point of view, a lumped-element inductor model still cannot replace electromagnetic field simulation software packages such as Ansoft HFSS^{TM}.

In order to accurately model inductors, it is necessary to identify relevant parasitic effects. Inductors are magnetic energy-storing elements and consequently the inevitable resistance and capacitance are counter-productive and can be considered parasitics. This current study deals with thick-metal loop inductors on a dielectric substrate of which the top views are shown in Figure 2.2.

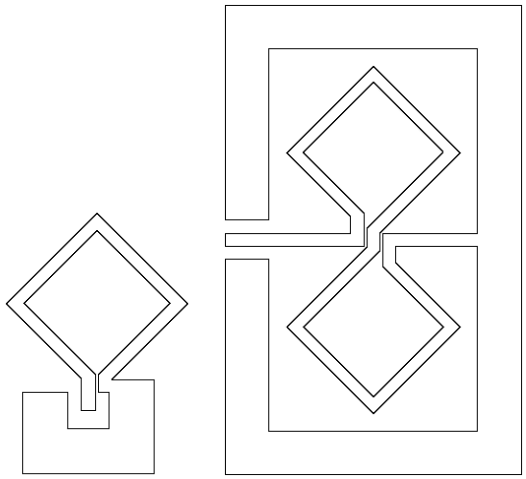

(a) 1-loop. (b) 2-loop.

Figure 2.2. Top view of two loop inductor types.

A lumped-element model of a loop inductor on a dielectric substrate is shown in Figure 2.3. The model is adapted from the multi-turn spiral inductor on silicon model [49, 50]. The oxide capacitance is absent in Figure 2.3 because no oxide layer exists in the inductor on dielectric case. Further, in the case of a spiral inductor on silicon, there is a metal layer on the back side of the substrate that is kept at zero (i.e. ground) potential, leading to substrate parasitic capacitances and resistances to ground. In the case of the loop inductor on a dielectric substrate, this back-side ground metal layer does not exist. The inductors, instead, have coplanar ground

structures. Although the coplanar configuration causes the majority of electric fields between the loop inductor and ground structure to be parallel to the substrate, a finite portion of the fields still passes through the substrate before reaching the ground structures. This fringing fields are assumed to introduce finite substrate parasitic capacitances and resistances, parallel to ground, and are represented by C_{shunt} and R_{sub}.

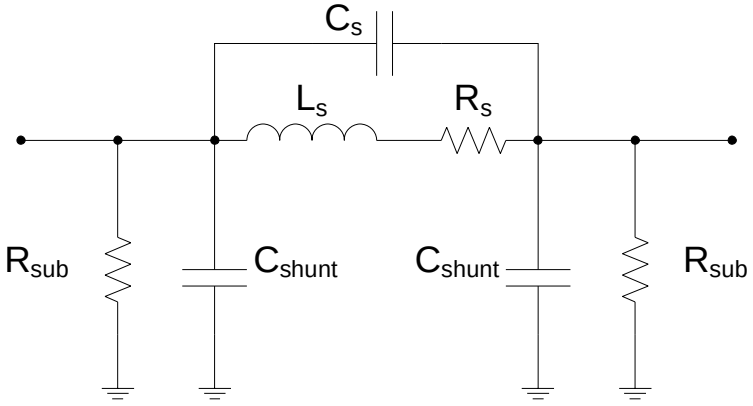

Figure 2.3. Lumped-element model of a loop inductor on a dielectric substrate adapted from [49].

The model consists of a series inductance, L_s, and a series resistance, R_s, which represent the desired inductance and the parasitic resistance of the loop inductor respectively. In addition, a capacitance, C_s, exists between the input and output terminals of the inductor. This capacitance represents the combination of capacitive coupling between loop segments and capacitive coupling in the gap closing the loop. In a multi-turn spiral inductor, C_s represents the inter-turn capacitive coupling and the spiral turns-to-overpass overlap capacitive coupling. Next, there also exists parasitic capacitance between the loop inductor and ground structures, represented by C_{shunt}. Additionally, the model also incorporates resistors, R_{sub}, that represent energy loss sustained by electric fields, generated by magnetic fields penetrating the

substrate, in the lossy dielectric substrate.

Series Inductance, L_s

A loop inductor can be considered as a simplified version of a multi-turn spiral inductor. Therefore, the method to calculate L_s for a spiral inductor is still relevant to the loop inductor case. Based on formulas for inductance calculation presented by Grover in [51], Greenhouse developed a method to compute the inductance of rectangular spiral inductors [52] This technique divides a spiral into straight segments and states that the overall inductance of the spiral is computed by summing the self inductance of each segment and the positive as well as the negative mutual inductance between all possible segment pairs. The mutual inductance is positive if the currents in two conductor segments have the same direction and negative for opposite currents. The Greenhouse method is mathematically expressed as [52]

$$L_s = L_{self} + \sum M_+ - \sum M_- \tag{2.8}$$

L_s = overal series inductance of a spiral inductor (H)
L_{self} = total self-inductance of all straight segments (H)
$\sum M_+$ = sum of the positive mutual inductances (H)
$\sum M_-$ = sum of the negative mutual inductances (H)

An approximation to the direct current (DC) self-inductance of a conductor with a rectangular cross-section can be expressed as follow [49, 52]

$$L_{self} = 2l\left(\ln\frac{2l}{w+t} + 0.50049 + \frac{w+t}{3l}\right) \tag{2.9}$$

where L_{self} is the self-inductance (nH), l is the conductor length (cm), and w and t are the conductor width and thickness (cm) respectively. Inductance is mainly governed by the external magnetic flux to the conductor. Consequently, variations in the conductor cross-section dimensions have little effect on the self-inductance. This being said, in general, inductance increases slightly with smaller cross-section area due to the enhanced magnetic flux external to the wire [49]. Dependency of inductance on conductor length is also shown in [49] to be slightly more than linear.

Following [52], the mutual inductance of two parallel conductor segments can be evaluated using

$$M = 2lq \tag{2.10}$$

where M is the mutual inductance (nH), l is the conductor length (cm), and q is the mutual inductance parameter (unitless).

The mutual inductance parameter, q, of a conductor is determined by its length and geometric mean distance (GMD) between itself and the adjacent parallel conductor. The expressions for q and GMD are given as

$$q = \ln\left[\frac{l}{GMD} + \sqrt{1 + \left(\frac{l}{GMD}\right)^2}\right] - \sqrt{1 + \left(\frac{GMD}{l}\right)^2} + \frac{GMD}{l} \tag{2.11}$$

$$\ln GMD = \ln d - \frac{w^2}{12d^2} - \frac{w^4}{60d^4} - \frac{w^6}{168d^6} - \frac{w^8}{360w^8} - \ldots \tag{2.12}$$

where w is the conductor width (cm) and d is the pitch (centre-to-centre distance) between adjacent conductors (cm). A narrower separation between parallel conductors leads to larger mutual inductance due to enhanced magnetic coupling [49]. Further, for a constant pitch, mutual inductance does not vary with conductor width. Also notice that two orthogonal conductors do not have mutual inductance since their magnetic fluxes are not linked together.

Series Resistance, R_s

When a metal conductor is exposed to a time-varying magnetic field, such as that from an alternating current (ac), an eddy current is produced. Eddy currents, which can come in the form of proximity and skin effects, induce magnetic fields following Lenz's law and lead to a non-uniform current density in the conductor. The proximity effect takes place when eddy currents are induced in a conductor by time-varying magnetic fields from nearby conductors that carry time-varying currents. On the other hand, the skin effect arises from eddy currents induced by changing magnetic fields from an alternating current flowing in the conductor itself. In either form, eddy currents limit the capability of a conductor to carry high-frequency currents, increasing the ac resistance.

At high frequencies, alternating currents tend to flow at the surface ("skin") of a conductor, leading to a non-uniform current density in the conductor's cross-section. This is known as the skin effect. The *skin depth*, δ, is the depth below the surface of a conductor at which the current density decays to 1/e of the current density at the surface, J_s [53, 54]. For good conductors, the skin depth is [54]

$$\delta = \sqrt{\frac{1}{\pi f \sigma \mu_r \mu_0}} \tag{2.13}$$

where μ_r is relative permeability of the conductor, μ_0 is the free-space permeability ($4\pi \times 10^{-7}$H/m), σ is the conductivity (S/m), and f is the frequency of interest (Hz).

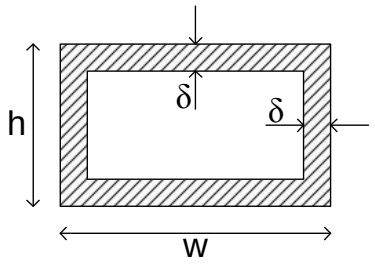

Figure 2.4. Effective cross-section of a rectangular conductor under skin effect.

In loop inductors with tall rectangular conductors, the skin effect causes the conductors to effectively behave like rectangular tubes with a thickness of the skin depth, δ as illustrated in Figure 2.4. The effective cross-section of the rectangular conductor in the loop inductors can be estimated by

$$A_{eff} = wh - (w - 2\delta) \cdot (h - 2\delta) \approx 2\delta(w + h) \tag{2.14}$$

where $4\delta^2$ is neglected ($4\delta^2 \ll 2\delta(w + h)$). Therefore, the series resistance, R_s, is approximately

$$R_s = \frac{l\rho}{A_{eff}} \approx \frac{l\rho}{2\delta(w + h)} \tag{2.15}$$

where ρ is the conductor resistivity (Ωm), l is the conductor length (m), w and h are the conductor width and height (m) respectively, and δ is the skin depth (m).

Capacitance, C_s

In a tall loop inductor, the parasitic capacitance, C_s, comes from capacitive coupling in the gap closing the loop and also from the capacitive coupling between the loop segments. Due to the considerable metal height, this parasitic capacitance is essentially parallel-plate capacitance with air dielectric. This is expressed as

$$C_s = \frac{\epsilon_0 A}{d} \tag{2.16}$$

where ϵ_0 is the free-space permittivity (8.85×10^{-12} F/m), A is the surface area of the metal segments facing each other (m^2), and d is the separation between the metal segments (m).

Substrate Loss Effect, R_{sub}

In a loop inductor, magnetic field penetrates perpendicularly the substrate. Following a Maxwell's equation [55],

$$\nabla \times \mathbf{E} = -\frac{\partial \mathbf{B}}{\partial t} \tag{2.17}$$

this time-varying magnetic field generates a time-varying electric field in the surrounding area, including inside the substrate. In a substrate medium with non-zero conductivity, σ, this electric field causes a conduction current of $J_c = \sigma \mathbf{E}$ to flow, which leads to some energy dissipation as heat inside the substrate medium.

In the case of a dielectric that is a good insulator, the direct conduction current due to finite conductivity is negligible. But at high frequencies, the rapidly varying electric field polarizes bound electrons inside the dielectric, thus doing work against the internal molecular forces, and generates an alternating current in phase with the field. As a result, a dielectric, which would be an insulator at low frequencies or DC, can consume substantial energy under high frequency fields and dissipate the energy as heat. This high-frequency dielectric loss can be attributed to the complex dielectric constant (complex relative permittivity) defined as [55]

$$\epsilon_{r,c} = \epsilon'_r - j\epsilon''_r \tag{2.18}$$

Usually, the dielectric constant of a material is given in terms of its real component and a dielectric loss tangent, defined as [55]

$$\tan \delta_c = \frac{\epsilon_r''}{\epsilon_r'} \tag{2.19}$$

The effect of the complex dielectric constant to a zero-conductivity dielectric material is as follow:

$$\nabla \times \mathbf{H} = (\omega \epsilon_0 \epsilon_r'') \, \mathbf{E} + j\omega \epsilon_0 \epsilon_r' \mathbf{E} \tag{2.20}$$

where ϵ_0 is the free-space permittivity. It can be seen that ϵ_r'' generates a volume current density term that is in phase with the electric field. Although ϵ_r'' is small, at high frequencies ($\omega \epsilon_0 \epsilon_r''$) becomes considerable and gives the same macroscopic effect as a material with an effective conductivity of [55]

$$\sigma_{eff} = \omega \epsilon_0 \epsilon_r'' = \omega \epsilon_0 \epsilon_r' \tan \delta_c \tag{2.21}$$

At such high frequencies, an alternating current density of $(\omega \epsilon_0 \epsilon_r'')\mathbf{E}$ flows in response to the electric field, which leads to some energy dissipation in the form of heat inside the dielectric.

This energy loss inside the dielectric can be represented by resistors, R_{sub}, of which values can be calculated using [50, 56]

$$R_{sub} = 2 \, \frac{t_{eff}}{\sigma_{eff} \, lw} \tag{2.22}$$

$$t_{eff} = \frac{w}{2\pi} \ln \left(\frac{8t}{w} + \frac{4w}{t} \right) \tag{2.23}$$

where w is the width of the metal-trace (m), l is the length of the metal trace (m), t is the thickness of the substrate (m), and t_{eff} is the effective thickness of the substrate (m). The factor of two in equation (2.22) is included because the substrate resistance is assumed to be distributed evenly at the two inductor terminals.

Stray Capacitance to Ground, C_{shunt}

Both loop inductor types have additional ground structures configured to facilitate testing with ground-signal-ground (GSG) wafer probes. Unfortunately the potential

difference between the ground structures and the inductance loop leads to stray capacitance to ground, C_{shunt}. Since the metal conductor has a considerable height, the stray capacitance is an air-dielectric parallel-plate capacitance which, in theory, could possibly be calculated using a parallel-plate capacitor formula. However the non-constant separation between the loop and the ground structures complicates the calculation. More study is needed to determine the exact expression for C_{shunt}.

2.1.3 Quality Factor and Self-resonant Frequency

Quality (Q) factor and self-resonant frequency (SRF) originate from resonant circuits. They are relevant to loop inductors as the inductors exhibit finite parasitic capacitances.

In general, Q-factor of a passive device is proportional to the ratio of energy stored to the energy lost in a cycle. However, because inductors are magnetic-energy storing elements, only the net magnetic energy stored is of interest since any electric energy due to the parasitic capacitances is counter-productive. Thus, the inductor Q-factor can be defined as [57, 58]

$$Q - \text{factor} = 2\pi \frac{|W_m| - |W_e|}{W_{lost\ in\ a\ cycle}} = 2\omega \frac{|W_m| - |W_e|}{P_{lost}} \tag{2.24}$$

where W_m and W_e represent the magnetic and electric energy, respectively, and P_{lost} indicates the power dissipated from the inductor. The magnetic and electric energy vary as frequency increases. At a particular frequency, they are eventually equal to each other, forcing the Q-factor to become zero and the inductor to self-resonate. This frequency is commonly noted as the *self-resonant frequency (SRF)* of the inductor.

A loop inductor can be characterized only by its input admittance (or impedance). For this reason, the loop inductors in this current work were designed as one-port elements. Grounding one of the ports removes half of the shunt parasitic effects in the lumped element model, but it does not remove them in the real inductor since in reality the parasitics are distributed. Consequently, one-port grounding reduces the accuracy of the inductor model. Despite this fact, the model can still be used

to understand how the parasitics affect the inductor performance.

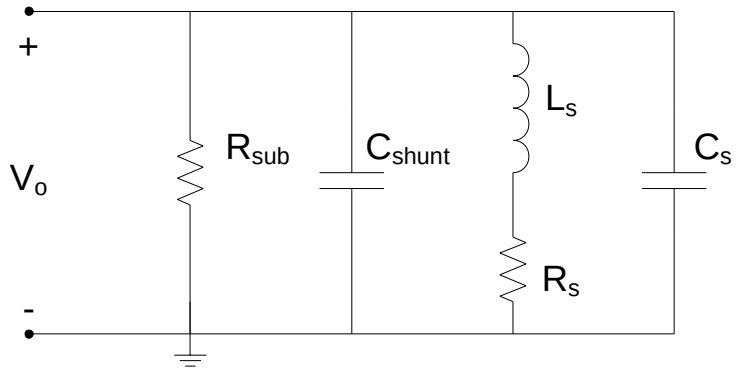

Figure 2.5. One-port model of a loop inductor on a dielectric substrate [57].

Figure 2.5 shows the one-port loop inductor model where the ground potential is assumed to come from the coplanar ground structures. It is obtained by grounding port two in the two-port inductor model shown in Figure 2.3. It is necessary to point out that R_{sub} and C_{shunt} are not really straight paths to ground, but rather consequences of the electromagnetic fields passing through the substrate to reach the ground structures. Using circuit analysis, the Q-factor can be expressed using the inductor's input admittance, Y_{11}, as shown in the following equations [57].

$$Y_{11} = \left(\frac{1}{R_{sub}} + \frac{R_s}{R_s^2 + \omega^2 L_s^2}\right) + j\omega\left(C_{shunt} + C_s - \frac{L_s}{R_s^2 + \omega^2 L_s^2}\right) \tag{2.25}$$

$$Q = -\frac{im(Y_{11})}{re(Y_{11})} = \frac{\omega\left[L_s R_{sub} - R_{sub}(R_s^2 + \omega^2 L_s^2)(C_{shunt} + C_s)\right]}{R_s^2 + \omega^2 L_s^2 + R_s R_{sub}} \tag{2.26}$$

Recall that the Q-factor can also be obtained using the energy stored in and dissipated from the inductor which can be expressed as [57, 59]

$$W_m = \frac{V_0^2 L_s}{2(\omega^2 L_s^2 + R_s^2)} \tag{2.27}$$

$$W_e = \frac{V_0^2(C_s + C_{shunt})}{2} \tag{2.28}$$

$$W_{Lost\ in\ a\ cycle} = \frac{2\pi}{\omega}\frac{V_0^2}{2}\left[\frac{1}{R_{sub}} + \frac{R_s}{R_s^2 + \omega^2 L_s^2}\right] \tag{2.29}$$

Substituting equations (2.27), (2.28), (2.29) into equation (2.24), the inductor Q-factor can alternatively be expressed as [57, 59]

$$Q = \frac{\omega L_s}{R_s} \cdot \frac{R_{sub}}{R_{sub} + R_s \left[\left(\frac{\omega L_s}{R_s} \right)^2 + 1 \right]} \cdot \left[1 - \frac{R_s^2 (C_s + C_{shunt})}{L_s} - \omega^2 L_s (C_s + C_{shunt}) \right]$$
$$= \frac{\omega L_s}{R_s} \cdot (substrate\ loss\ factor) \cdot (self - resonance\ factor) \tag{2.30}$$

where both the $substrate\ loss\ factor$ and the $self-resonance\ factor$ can have any values between zero and one. Upon close inspection, it can be seen that equations (2.30) and (2.26) are equivalent to each other.

The SRF of the inductor can be obtained by equating the self-resonance factor in equation (2.30) to zero, which will result in

$$\omega_{SR}^2 = \frac{1}{L_s (C_s + C_{shunt})} - \frac{R_s^2}{L_s^2} \tag{2.31}$$

The second term in equation (2.31) is usually much smaller than the first term. When this is true, the SRF can then be approximated as

$$\omega_{SR} \approx \frac{1}{\sqrt{L_s (C_s + C_{shunt})}} \tag{2.32}$$

Notice that C_{shunt} in equation (2.32) is half of what really exists in the real inductor due to the grounding of the second inductor port. However, in thick-metal loop inductors, C_s is expected to be more significant than C_{shunt}. Therefore, the accuracy of the equation may not be greatly affected. This being said, equation (2.32) should still be treated as an approximation.

If the Q-factor of a spiral inductor is plotted against frequency, it will typically have a parabolic shape with a maximum, Q_{max}, occurring at a frequency, $f_{Q_{max}}$, as shown in Figure 2.6. This Q-plot characteristic can be explained qualitatively using the one-port inductor model shown in Figure 2.5. At low frequencies, R_{sub} and the capacitive impedance $X_{C_{shunt}}$ and X_{Cs} are bigger than the series impedance of L_s and R_s. Taking the path of least impedance, alternating current flows through the L_s and R_s branch and the Q-factor can be approximated by $\omega L_s / R_s$. As the frequency increases, R_{sub}, $X_{C_{shunt}}$, and X_{Cs} decrease while X_{Ls} and R_s increase. Consequently,

the alternating current starts to flow through R_{sub}, C_{shunt}, and C_s branches, leading to less magnetic energy stored in the inductor. Further, the current flowing through the resistor R_{sub} increases the total dissipated power from the inductor, P_{lost}. The combination of lower magnetic energy stored and higher power dissipated slows down the increase of the Q-factor until it eventually peaks at Q_{max}. As frequency increases further beyond $f_{Q_{max}}$, the trend becomes more severe, further reducing the Q-factor. At the SRF, the total parasitic capacitive impedance equals the inductive impedance, causing the inductor to resonate and the Q-factor to vanish.

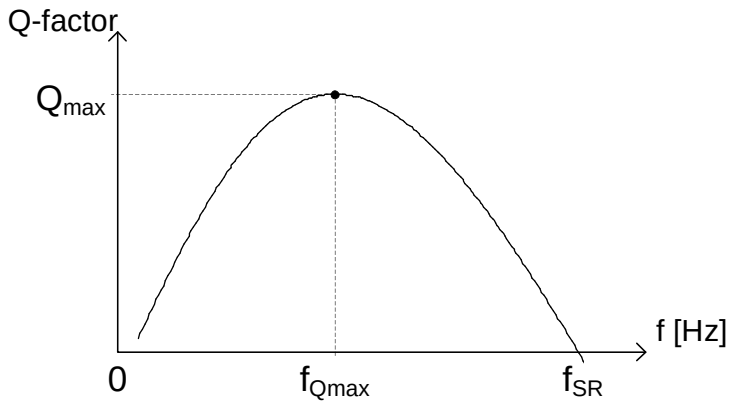

Figure 2.6. Typical Q-factor plot of spiral inductors.

2.2 Low-pass Filters

2.2.1 Low-pass Filter Principle

A low-pass filter (LPF) is a circuit that passes low-frequency signals and attenuates signals with frequencies higher than a *cut-off frequency*, forming pass-band and stop-band regions. There are many ways to realize a low-pass filter. The current study deals with a reactive lumped element-based LPF implemented using passive inductors and capacitors.

A representation of a single-input single-output LPF in frequency domain is shown in Figure 2.7. The output and input are related through a transfer function

$$H(s) = \frac{Y(s)}{X(s)} \tag{2.33}$$

where $X(s)$, $Y(s)$, and $H(s)$ are polynomials in the complex frequency variable $s = \sigma + j\omega$. The transfer function, $H(s)$, is generally a complex parameter which,

Figure 2.7. A representation of a low-pass filter in frequency domain.

along the $j\omega$ axis, can be represented as

$$H(s)|_{s=j\omega} = |H(j\omega)|e^{j\theta(\omega)} \tag{2.34}$$

where $|H(j\omega)|$ and $\theta(\omega)$ are referred to as the *magnitude* and *phase response* respectively, and $\omega = 2\pi f$ is the angular frequency (rad/s).

An ideal LPF completely passes all frequencies below the *cut-off frequency*, ω_p, and attenuates those above it, without a transition region in between. This ideal "brick-wall" type of response requires an infinite number of filter elements, making it practically unrealizable. A real-life LPF can only approximate the ideal response, for instance, Chebyshev, Butterworth approximation, etc. The ideal and practical

LPF responses are illustrated in Figure 2.8. The amount of response deviations of a practical LPF response from that of an ideal one can be expressed in decibels (dB) as

$$\alpha_p = 20\log(A_0/A_1) \tag{2.35}$$

$$\alpha_s = 20\log(A_0/A_2) \tag{2.36}$$

where α_p and α_s is known as pass-band ripple and stop-band attenuation respectively.

2.2.2 Chebyshev Approximations

Low-pass filters may operate in various frequency ranges and impedance levels. It is, therefore desirable to standardize the basic theory and design, and then adapt the filter for the desired applications. This can be achieved using normalized low-pass filters, defined as low-pass filters having unity cut-off frequency, ω_p= 1 rad/s, and unity source resistance, R_{source}= 1 Ω. In the rest of the discussions to follow, a normalized low-pass filter is assumed.

The general method to approximate an ideal LPF magnitude response is to find a function in the form of [60]

$$|H(j\omega)|^2 = \frac{A_0}{1 + F(\omega^2)} \tag{2.37}$$

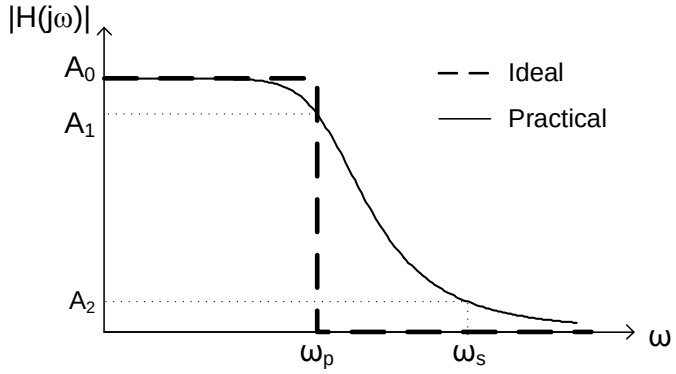

Figure 2.8. Magnitude response of an ideal and practical LPF [60].

such that, $F(\omega^2) \ll 1$ in the $0 < \omega < \omega_p$ range and $F(\omega^2) \gg 1$ in the $\omega > \omega_p$ range. Such a function will make $|H(j\omega)|^2 \approx A_0$ in the pass-band and $|H(j\omega)|^2 \approx 0$ in the stop-band. The Chebyshev approximation achieves this by using *Chebyshev Polynomials*.

The Chebyshev polynomials of order n is defined as

$$C_n(\omega) = \cos(n \arccos\ \omega), \qquad |\omega| \leq 1 \tag{2.38}$$

$$C_n(\omega) = \cosh(n \operatorname{arccosh}\ \omega), \qquad |\omega| > 1 \tag{2.39}$$

$C_n(\omega)$ is a polynomial function in ω. This is more apparent in its recursive form given in (2.40) with some of the polynomials listed in Table 2.1. [60].

$$C_{n+1}(\omega) = 2\,\omega C_n(\omega) - C_{n-1}(\omega) \tag{2.40}$$

Table 2.1. Chebyshev polynomials of different order, n [60].

n	$C_n(\omega)$
0	1
1	ω
2	$2\omega^2 - 1$
3	$4\omega^3 - 3\omega$
4	$8\omega^4 - 8\omega^2 + 1$
5	$16\omega^5 - 20\omega^3 + 5\omega$

From (2.38), one can realize that $C_n(\omega)$ varies between -1 and 1 in the $0 \leq \omega \leq 1$ range. Moreover, one can notice from Table 2.1 that $C_n(\omega)$ is an even function when n is even and odd when n is odd. Further, at high frequencies $C_n(\omega)$ can be approximated by

$$C_n(\omega) \approx 2^{n-1}\omega^n, \qquad \omega \gg 1 \tag{2.41}$$

$C_n(\omega)$ variations in the $0 \leq \omega \leq 1$ range leads to pass-band ripples in the magnitude response of a Chebyshev low-pass filter. To control the ripple amount, a small

number, ϵ, is introduced. The function F(ω^2) can then be expressed as

$$F(\omega^2) = \epsilon^2 C_n^2(\omega) \tag{2.42}$$

Substituting (2.42) into (2.37), the magnitude response of an n^{th}-order normalized Chebyshev low-pass filter is

$$|H(j\omega)| = \frac{A_0}{\sqrt{1+\epsilon^2 C_n^2(\omega)}} \tag{2.43}$$

As passive filters do not generally introduce gain, A_0 will have to be adjusted such that $|H(j\omega)|_{max} = 1$.

Two representative magnitude responses for $n = 3$ and $n = 6$ with $A_0 = 1$ are plotted in Figure 2.9. From the magnitude responses shown, the following can be observed:

1. At $\omega = 0$, $C_n(0) = 0$ for n odd and $C_n(0) = 1$ for n even leading to

$$|H(j0)| = 1, \qquad \text{for } n \text{ odd} \tag{2.44}$$

$$|H(j0)| = \frac{1}{\sqrt{1+\epsilon^2}}, \qquad \text{for } n \text{ even} \tag{2.45}$$

2. At $\omega = 1$, since $C_n(1) = 1$ then

$$|H(j1)| = \frac{1}{\sqrt{1+\epsilon^2}}, \qquad \text{for all } n \tag{2.46}$$

3. The cut-off frequency, ω_p= 1, is the frequency where the last ripple-point occurs before the magnitude response decreases monotonically.

4. There are n half-ripples (minimum to maximum or vice versa) in the pass band

For $\omega \gg 1$, $|H(j\omega)|$ can be approximated as

$$|H(j\omega)| \approx \frac{1}{\epsilon^2 2^{n-1}\omega^{2n}} \tag{2.47}$$

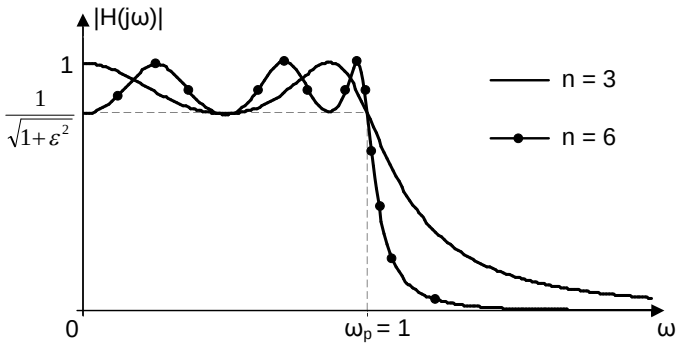

Figure 2.9. Third and sixth-order Chebyshev magnitude responses.

2.2.3 Chebyshev Low-pass Filter Transfer Function

The transfer function of a Chebyshev low-pass filter, can be expressed as

$$H(s) = \frac{A_0}{Y(s)} = \frac{A_0}{(s - s_1)(s - s_2)\ldots(s - s_k)} \tag{2.48}$$

where $s_1, s_2, \ldots, s_k$ are the left-halfplane poles of $H(s)$. Again A_0 will have to be adjusted to ensure the filter does not introduce a gain.

The left-halfplane poles of $H(s)$ can be obtained using the following equations [60]

$$s_k = \sigma_k + j\omega_k = \sin\left[\frac{(2k-1)\pi}{2n}\right]\sinh v + j\cos\left[\frac{(2k-1)\pi}{2n}\right]\cosh v \tag{2.49}$$

$$v = \frac{1}{n}\operatorname{arcsin}(\frac{1}{\epsilon}) \tag{2.50}$$

where $k = 1, 2, \ldots, 2n$ and n is the order of the Chebyshev low-pass filter.

Since sine and cosine function have periods of 2π, there are only $2n$ distinct zeros given by (2.49). As a result, k needs to take only $2n$ consecutive integers. However, to ensure stability of the filter, only n distinct left-halfplane zeros are needed to form the denominator of $H(s)$. So, an n^{th}-order Chebyshev low-pass filter will have an n^{th}-degree transfer function, $H(s)$. Further details on the poles of a Chebyshev filter can be found in [60]. Several denominator polynomials for normalized Chebyshev low-pass filters are given in Appendix A.

2.2.4 Synthesis of a Doubly-Terminated LC Filter

A doubly-terminated LC filter can be represented in Figure 2.10 where the filter is shown as a lossless two-port network. The components to the left of port 1 represent the Thevenin's equivalent of the circuitry connected there (e.g. excitation source), whereas R_2 represents a load which can be an input impedance of another circuitry.

The performance of a doubly-terminated LC filter is commonly measured in terms of power. A maximum amount of power will be transferred to the load when the load and the output impedance (Z_{out}) are conjugate to each other and, simultaneously, when the source and input impedance (Z_{in}) are conjugate to each other.

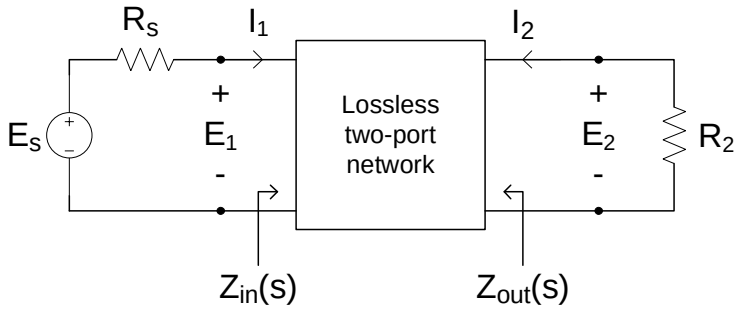

Figure 2.10. A representation of a doubly-terminated lossless filter [60].

When the matching conditions are met and the source/load impedances are represented by resistances, the maximum power available from the source, P_{max}, and the power delivered to the load, P_2, can be expressed as [54]

$$P_{max} = \frac{|E_s|^2}{8R_s} \tag{2.51}$$

$$P_2 = \frac{|E_2|^2}{2R_2} \tag{2.52}$$

P_{max} and P_2 are related through a parameter called transmission coefficient, $t(s)$ which represents the amount of power transferred between the two ports. For $s = j\omega$, the magnitude-squared of $t(s)$ gives the power ratio [60]:

$$|t(j\omega)|^2 = \frac{P_2}{P_{max}} = \frac{4R_s}{R_2}\left|\frac{E_2}{E_s}\right|^2 \tag{2.53}$$

Note that as lossless LC passive filters do not introduce a gain, under the best case scenario, P_2 can only equal P_{max}, making $|t(j\omega)| \leq 1$.

For filter applications, it is desirable to make $|t(j\omega)|$ as close to unity as possible in the pass-band, to allow maximum power from the source to reach the load, and to make $|t(j\omega)|$ as close to zero as possible in the stop-band. When $|t(j\omega)|$ approaches zeros, most of the available power is reflected back to the source. The amount of reflected power is represented by *reflection coefficient*, $\rho(s)$ which is defined in such a way that at $s = j\omega$ [60],

$$|\rho j\omega|^2 = 1 - |t(j\omega)|^2 \tag{2.54}$$

With port 2 terminated in R_2, the input impedance at port 1 becomes the driving-point impedance function of the LC ladder filter. This generally complex impedance can be represented by

$$Z_{in}(j\omega) = R_{in}(\omega) + jX_{in}(\omega) \tag{2.55}$$

Since the two-port filter network is lossless, when $R_2 = Z^*_{out}$, the power delivered to Z_{in} and R_2 is the same ($P_2 = P_{in}$), leading to [54]

$$P_2(j\omega) = \frac{|E_s|^2}{2} \frac{R_{in}(\omega)}{|R_s + Z_{in}(j\omega)|^2} \tag{2.56}$$

Using (2.56) and (2.51), $|t(j\omega)|^2$ and $|\rho(j\omega)|^2$ can be re-written as:

$$|t(j\omega)|^2 = \frac{4R_s R_{in}(\omega)}{|R_s + Zin(j\omega)|^2} \tag{2.57}$$

$$|\rho(j\omega)|^2 = \frac{|R_s - Zin(j\omega)|^2}{|R_s + Zin(j\omega)|^2} \tag{2.58}$$

Each side of (2.58) is simply a multiplication of two complex conjugate functions. Hence, the reflection coefficient can be realized as [60]

$$\rho(s) = \pm \frac{R_s - Z_{in}(s)}{R_s + Z_{in}(s)} \tag{2.59}$$

which in turn can be re-arranged to get the driving-point impedance

$$Z_{in}(s) = R_s \frac{1 \pm \rho(s)}{1 \mp \rho(s)} \tag{2.60}$$

$Z_{in}(s)$ can then be realized into a doubly-terminated LC filter in a ladder configuration using the *Cauer* methods described in [60].

The realization of an LC filter in a ladder configuration can be a long process. Fortunately, normalized element values for various filter types and different orders are available in design tables [61, 62, 63]. One such table is provided in Appendix A for normalized Chebyshev low-pass filters of different orders and ripple amount.

2.2.5 Impedance and Frequency Transformations

A prototype low-pass filter (LPF) has a normalized source resistance of 1 Ω and a cut-off frequency ω_p= 1 rad/s. To adapt this prototype filter to a different impedance level and cut-off frequency, one may perform the impedance and frequency transformations.

The impedance transformations for various elements are as follow

$$R = k_z R_n \qquad L = k_z L_n \qquad C = \frac{1}{k_z} C_n \tag{2.61}$$

$$k_z = \frac{Z_0}{R_n} \tag{2.62}$$

where k_z is the impedance scaling factor; R, L, C are the practical elements; and R_n, L_n, C_n are the normalized elements.

The frequency transformation from a normalized to a practical LPF is given by

$$s = \frac{1}{\Omega_p} S \tag{2.63}$$

where $s = \sigma + j\omega$ is the normalized frequency variable, $S = \Sigma + j\Omega$ is the transformed (or practical) frequency variable, and Ω_p is the practical cut-off frequency.

The transfer function of the practical low-pass filter can be obtained using (2.64) with the transformation illustrated in Figure 2.11.

$$H_{LP}(S) = H_{LP,normalized}\left(\frac{S}{\Omega_p}\right) \tag{2.64}$$

Applying (2.63) together with the impedance transformations gives the element transformation in Table 2.2. Transformation from a normalized low-pass filter to other type of practical filters can be obtained from [60, 64].

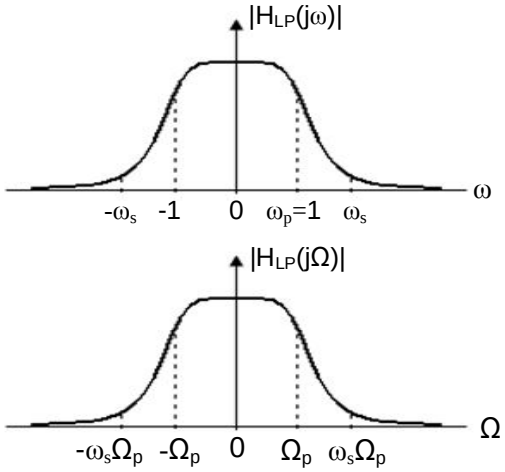

Figure 2.11. Normalized-to-practical low-pass transformation.

Table 2.2. Low-pass element transformations [64].

Normalized LPF Elements	Practical LPF Elements
L_n $z = L_n s$	$Z = k_z \left(\frac{L_n}{\Omega_p} \right) S$ $\left(\frac{k_z}{\Omega_p} \right) L_n$
C_n $y = C_n s$	$Y = \frac{1}{k_z} \left(\frac{C_n}{\Omega_p} \right) S$ $\left(\frac{1}{k_z \Omega_p} \right) C_n$
R_n $z = R_n$	$Z = k_z R_n$ $k_z R_n$

3. SCHEMATIC MODELS OF LOOP INDUCTORS AND LOW-PASS FILTERS

3.1 Loop Inductors

It was explained in Chapter 2 that in addition to the desired inductance values, practical loop inductors also produce unavoidable parasitic capacitances and resistances. Figure 3.1 shows the one-port loop inductor model. As explained in Section 2.1.2, R_{sub} and C_{shunt} are modeled as paths to ground, and represent dielectric loss and parasitic capacitance due to the field passing through the substrate. Using electronic design automation software called Agilent Advance Design System (ADS), each parasitic element value was individually varied to illustrate its effects on Q-factor and self-resonant frequency (SRF) of the inductor.

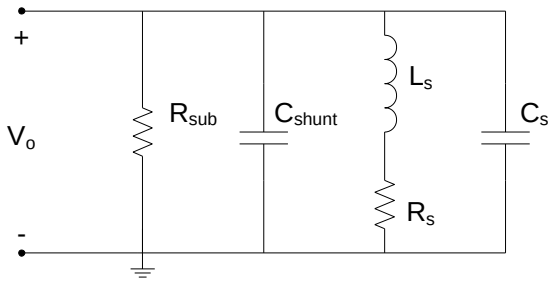

Figure 3.1. One-port model of a loop inductor on a dielectric substrate [57].

The resistance, R_s, represents the ohmic loss in the metal. Its effect on the Q-factor is shown in Figure 3.2 where the Q-factor is plotted against frequency as R_s is varied. A reduction in R_s, for instance through the use of a higher-conductivity metal, increases the Q-factor of the inductor. The SRF, however, remains unaffected.

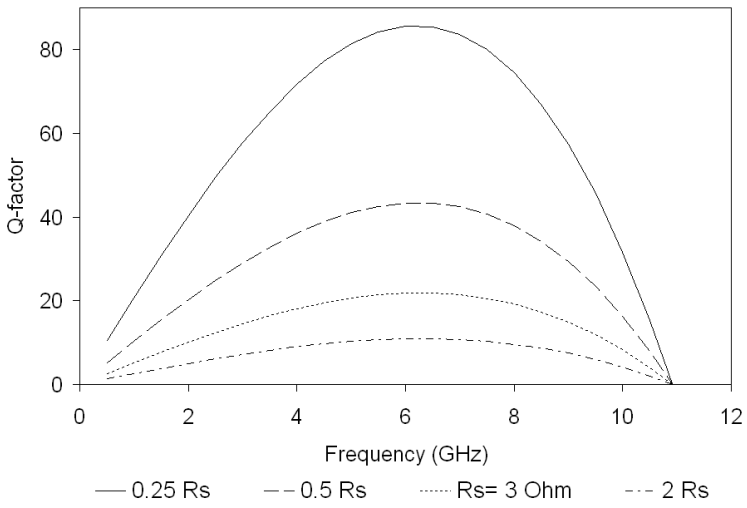

Figure 3.2. Effect of the series resistance, R_s, on Q-factor of an inductor.

The parasitic capacitances and resistances together with the inductance, L_s, form an RLC resonant circuit with a resonant angular frequency of

$$\omega_{SR} \approx \frac{1}{\sqrt{L_s\left(C_s + C_{shunt}\right)}} \tag{3.1}$$

Variations in either C_s, or C_{shunt}, or both will alter the total parasitic capacitance and, thus, the SRF of the inductor. In the case of loop inductors, C_s (parasitic capacitance from the gap closing the inductor loop) is the dominant parasitic capacitance. Figure 3.3 shows a plot of the Q-factor as a function of frequency as C_s is varied. It can be seen that a reduction in C_s increases the SRF of the inductor. In addition, smaller C_s also pushes the high-frequency portion of the Q-factor higher. The low-frequency portion of the Q-factor; however, remains unaffected because it is governed by the parasitic resistance of the metal, R_s.

Substrates also affect the performance of a loop inductor and their impacts are more severe at high frequencies. In the case of dielectric substrates, they degrade the inductor performance by consuming some energy from the electric field, generated by the magnetic fields penetrating the substrate, and dissipating the energy as heat. This dielectric loss phenomenon is the physical mechanism of energy loss through the substrate. When the dielectric loss increases, the amount of energy dissipated

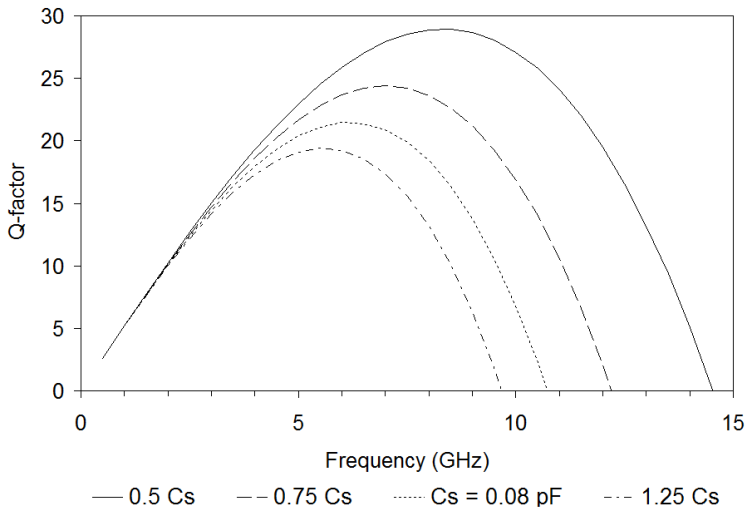

Figure 3.3. Effect of the parasitic capacitance, C_s, on Q-factor and SRF of an inductor.

from the inductor also increases which, in turn, decreases the inductor's Q-factor.

In the one-port inductor model, R_{sub} represents the dielectric loss and its effect on the Q-factor is shown in Figure 3.4. From the equivalent circuit point of view, an increase in the dielectric loss can be thought of as a decrease in R_{sub}. This would increase the "current" through R_{sub} at the expense of the current flowing through L_s. The smaller current through L_s would decrease the resulting magnetic field and magnetic energy stored in the inductor, thus, decreasing the Q-factor. Notice that the qualitative explanation using the current flow is simply an illustration to help understand the substrate loss effect. It is important to realize that in reality, the substrate is not grounded and the current to ground through R_{sub} does not really exist. The actual physical mechanism of substrate affecting the Q-factor is through the dielectric loss phenomenon.

3.2 Lumped-element Low-pass Filters

It was decided that two low-pass filters (LPF) with different 3-dB cut-off frequencies would be designed and fabricated. Both filters would have a 3^{rd}-order, 0.5-dB ripple Chebyshev response in a capacitor-inductor-capacitor "π" equivalent ladder

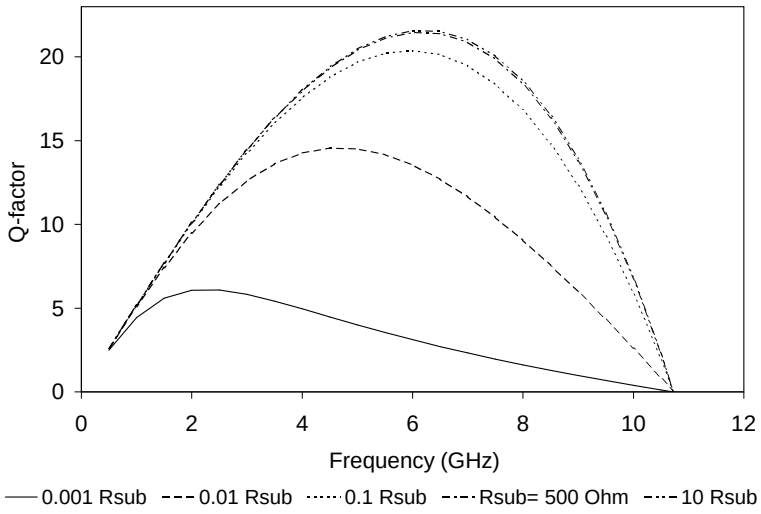

Figure 3.4. Effect of the dielectric loss, R_{sub}, on Q-factor of an inductor.

circuit. The design process started with a 3^{rd}-order low-pass prototype filter with both ports terminated in a resistor. This low-pass prototype filter is shown in Figure 3.5 where g_i (i= 0, 1, 2, 3, 4) represents the normalized component values for a 0.5-dB ripple Chebyshev response. Once the low-pass prototype filter was estab-

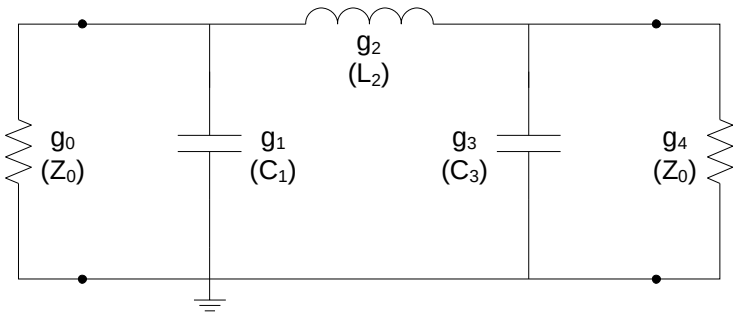

Figure 3.5. Third-order Chebyshev prototype LPF.

lished, frequency and impedance transformations, presented in Section 2.2.5, were then performed to obtain the actual L and C values that would give the desired 3-dB cut-off frequencies (C_1, L_2, and C_3). Note that the impedance and frequency

transformations did not change the "π" ladder circuit of the filter. They simply transformed the element values. The specifications for each Chebyshev low-pass filter are summarized in Table 3.1. The normalized component values were obtained from [61, 62] and are listed together with the de-normalized component values in Table 3.2.

Table 3.1. Design specifications of the Chebyshev low-pass filters.

Low-pass Filter Parameters	Design A	Design B
Order of filter, n	3	3
Pass-band ripple [dB]	0.5	0.5
Impedance of source/load, Z_0 [Ω]	50	50
Last-ripple frequency, (f_{ripple}) [GHz]	10.8	5.1
3-dB cut-off frequency, ($f_{3\text{dB}}$) [GHz]	12.9	6.7

Table 3.2. Element values of the Chebyshev low-pass filters.

Prototype LPF		Actual LPF		
Normalized	Values	De-normalized	Values-A	Values-B
g_0	1	Z_0 [Ω]	50	50
g_1	1.5963	C_1 [pF]	0.50812	0.97715
g_2	1.0967	L_2 [nH]	0.87273	1.67830
g_3	1.5963	C_3 [pF]	0.50812	0.97715
g_4	1	Z_0 [Ω]	50	50

In order to ensure that the de-normalized component values met the desired specifications of both low-pass filters, the LPF responses using these values were simulated using Agilent Advanced Design System (ADS) software. The simulated

frequency responses of both low-pass filters are given in Figure 3.6 and Figure 3.7.

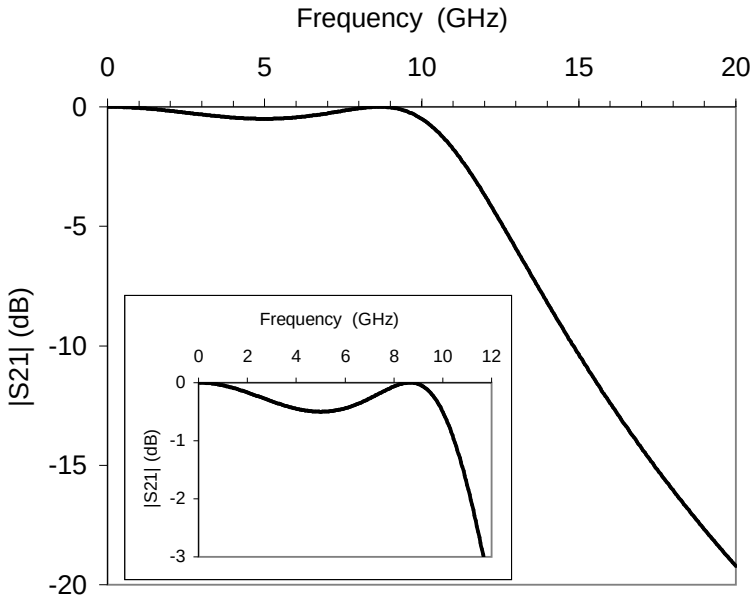

Figure 3.6. Schematic-model simulation result of LPF design A.

A Chebyshev low-pass filter with a given set of specifications (e.g. filter order, passband ripple, and 3-dB cut-off frequency) requires a set of L and C values which correspond to certain transfer function polynomials. Therefore, in general, changing the element values will alter both the pass-band ripple and the cut-off frequency of the filter. Figure 3.8 illustrates the effect of varying the value of capacitor C_1 to the frequency response of LPF design A. It shows that a bigger C_1 value increases the pass-band ripple and decreases the 3-dB cut-off frequency. A bigger C_1 value also leads to a steeper rejection slope in the stop-band. Variations in the value of inductor L_2 lead to slightly different effects on the frequency response which can be observed in Figure 3.9. It shows that a bigger value of inductor L_2 reduces the pass-band ripple and the 3-dB cut-off frequency while keeping the rejection slope in the stop-band relatively constant.

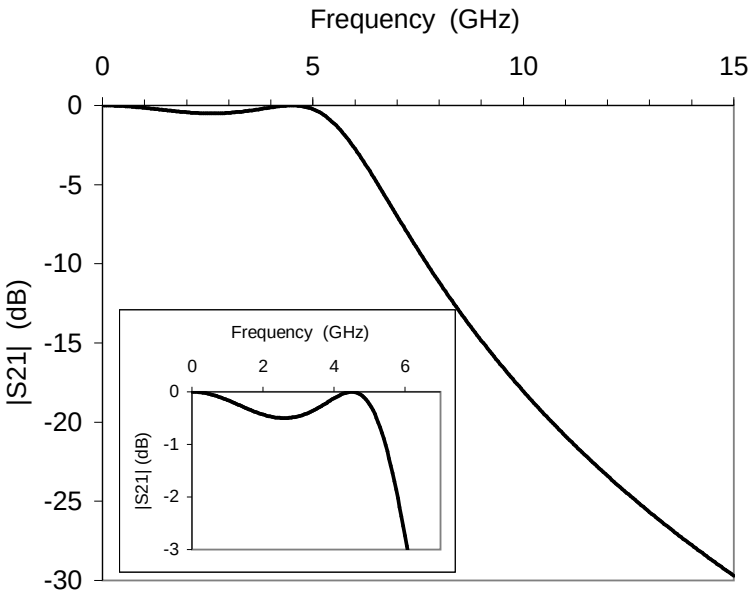

Figure 3.7. Schematic-model simulation result of LPF design B.

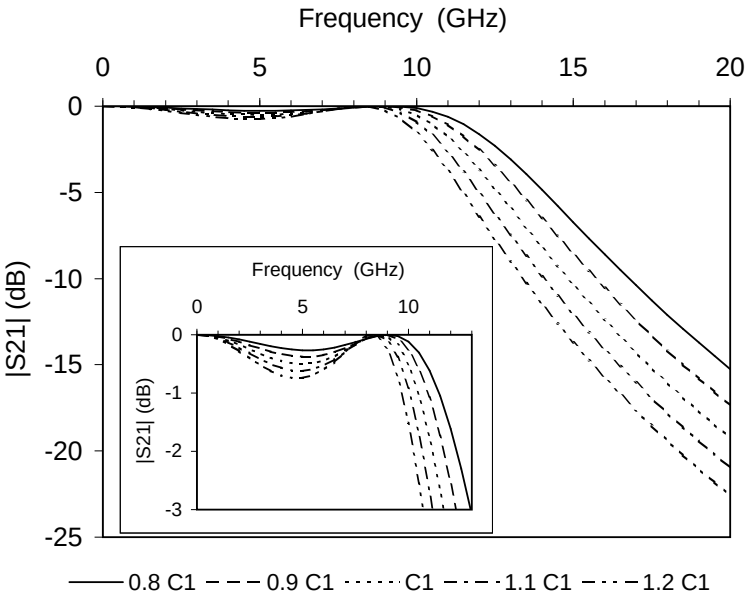

Figure 3.8. Capacitors effects on the frequency response of low-pass filter design A.

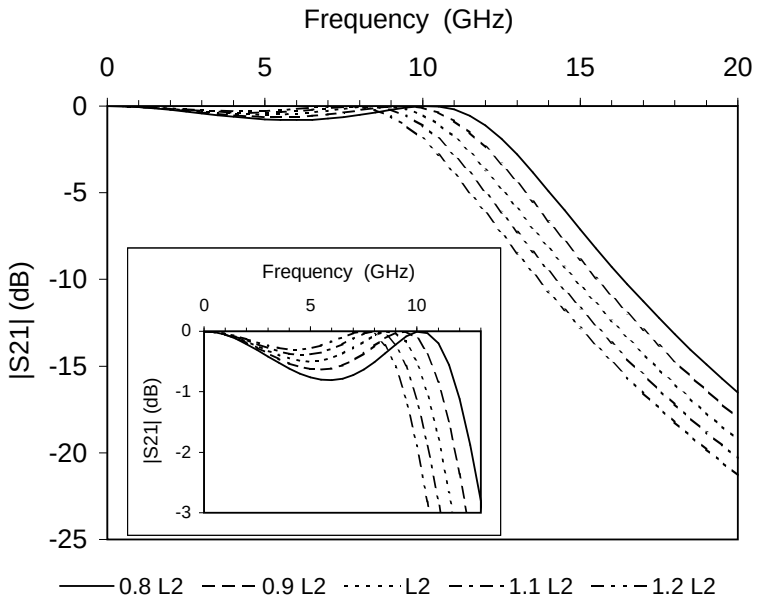

Figure 3.9. Inductor effects on the frequency response of low-pass filter design A.

4. STRUCTURAL MODELS AND DESIGN FABRICATION

4.1 Finite Element Electromagnetic Field Simulations Using Ansoft HFSS

It is necessary to obtain an estimate of key performance indices of the inductors and low-pass filters such as self-resonant frequencies, quality (Q) factors, inductances, return loss, and insertion loss. A method to estimate these performance indices from arbitrary 3D structures, operating at microwave frequencies is therefore required. This can be achieved using Ansoft HFSS$^{\text{TM}}$, a software package for 3D electromagnetic field simulation of high-frequency components.

In general, the steps in working with HFSS are as follows. The first step is to draw the geometric model of the structure, then specify the material properties of each object in the model. The next step is to define the necessary excitation ports that allow power into and out of the model and apply boundary conditions on parts of the model as necessary. The next step is to specify the solution frequency for the analysis and, if desired, the frequency sweep across which output will be generated. Once all these steps are completed, HFSS then generates the field solutions and the associated S-parameters, port characteristics, and the complex propagation constant. The S-parameters can then be converted to the Z- and Y-parameters, which can be used to find other parameters such as resistance/inductance values, self-resonant frequency, etc.

HFSS generates electromagnetic (EM) field solutions using the finite element method. It divides a geometric model into a large number of tetrahedra known as the finite element mesh, where a single tetrahedron is a four-sided pyramid [65]. At each vertex of a tetrahedron, HFSS stores the vector field (such as H-field or E-field) components that are tangential to the three edges of the tetrahedron. In

addition, HFSS can also store the field components that are tangential to a face of the tetrahedron and normal to an edge at the midpoint of the edges. Using these components, HFSS then interpolates the EM fields inside the tetrahedron. This method allows HFSS to represent Maxwells equations as a set of matrix equations and solve the equations using conventional numerical methods [65].

When generating a mesh, by default HFSS only creates a mesh inside an object if the object is specified with a material having a conductivity of less than 10^5 Siemens/meter. Based on this mesh, HFSS then generates field solutions inside the object. Since metals generally have conductivity greater than 10^5 Siemens/meter, HFSS creates only a surface mesh on metal objects and generates field solutions based on the surface mesh using a surface impedance approximation, which is based on skin depth, conductivity, and permeability [65].

Notice that there is a trade-off between the desired level of accuracy and the mesh size. In general, smaller tetrahedron size generates a more accurate solution. However, it leads to a larger number of tetrahedra which may overwhelm the available computer memory and processing power. It is therefore desirable to generate a solution based on a coarse mesh, refine the mesh, generate a new solution, and repeat the cycle until a parameter converges to within a desired limit. HFSS uses such an iterative process and calls it an adaptive analysis [65].

HFSS starts the solution process by generating an initial mesh on the entire model. It then determines the excitation field patterns at each port. To do this, HFSS assumes that each port is connected to a semi-infinitely long waveguide that has the same cross-section and material properties as the port. Therefore, the excitation fields are the fields of the traveling waves propagating along the waveguide to which the port is connected. The resulting 2-D field patterns are then used as boundary conditions to obtain the 3-D field solutions for the entire model [65]. Provided that each port is defined correctly, there will be a perfect matched condition between the port and the characteristic impedance of the waveguide connected to it. Next, HFSS generates the 3-D field solutions by exciting each port individually by a signal of one watt while setting other ports to zero watts. Once a solution is

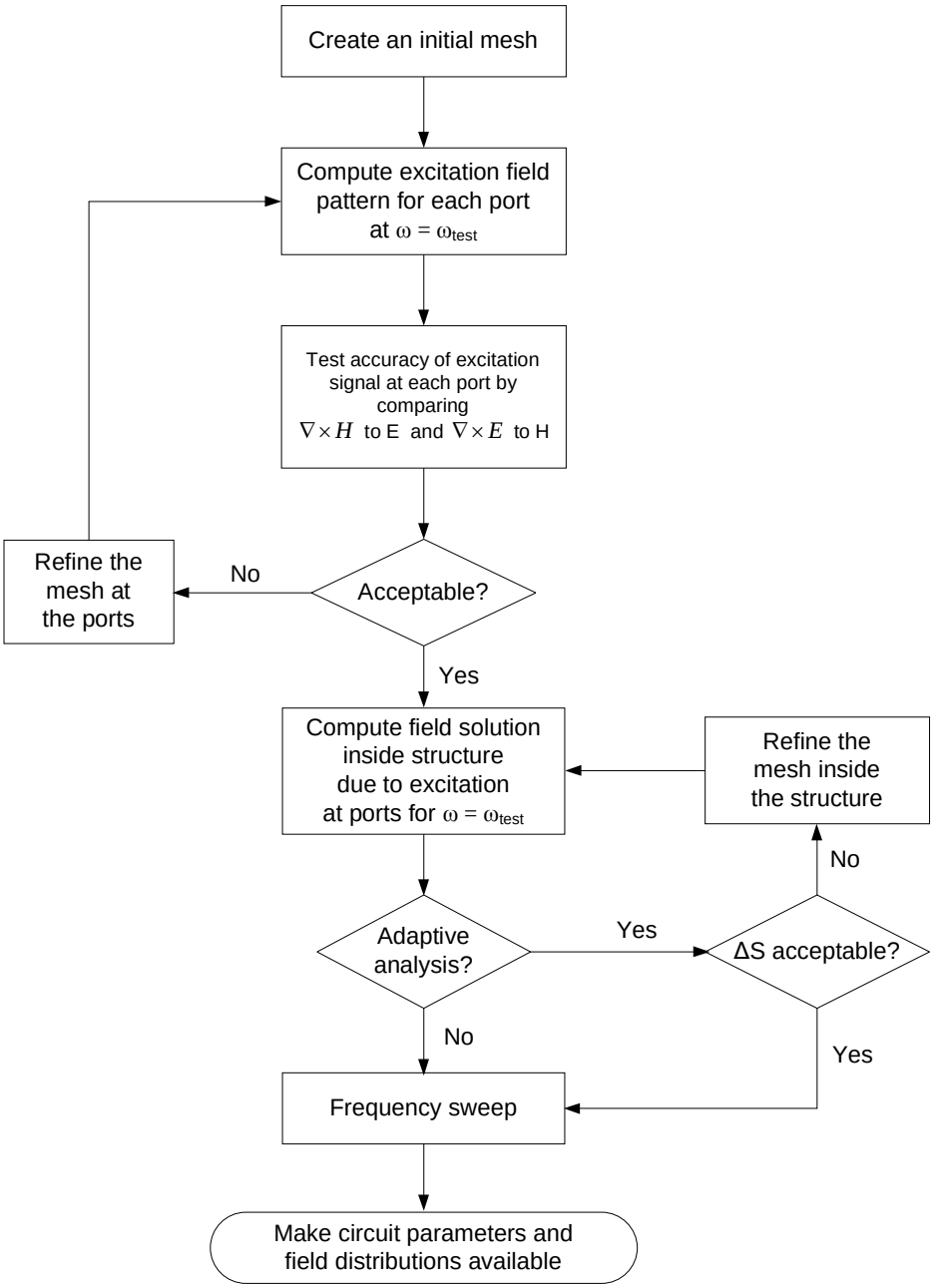

Figure 4.1. Adaptive analysis procedure in Ansoft HFSS.

obtained, another port is excited by a one-watt signal while others are set to zero watts and so forth [65]. After all ports have been excited, HFSS computes the generalized S-parameters from the amount of reflection and transmission that arises. When the adaptive analysis is required, using the generalized S-parameters, HFSS will estimate regions of the model where there is strong error and refine the mesh (tetrahedral) in those regions. Using the refined mesh, HFSS will produce another set of S-parameters, recalculate the error, and the iterative process continues until certain convergence criteria are met. Once the adaptive analysis converges, HFSS will solve the problem at a difference frequency if a frequency sweep is defined [65]. The entire process can be represented by the diagram shown in Figure 4.1.

4.2 Inductor Designs and Structural Models

One-loop and two-loop inductors were designed and their characteristics predicted using Ansoft HFSS. Figure 4.2 shows a representative 3D view of the one-loop and two-loop inductor designs. The one-loop inductor comprises one square turn attached to a ground structure whereas the two-loop inductor consists of two square turns connected in series and a ground structure surrounding the square turns. In both types, the ends of each square turn come very close to each other to form a loop. Consequently, a small gap is produced by these two ends and it is shown as closing gap in Figure 4.2. In both inductor types, the ground structure was included to facilitate testing using GSG (ground-signal-ground) wafer probes. As an effort to minimize extra inductance and parasitic resistance in the two-loop inductors, the ground structure width was made wider than that of the inductance loop. The one-loop inductors also had a ground structure with a different shape. This was to lessen the extra inductance and parasitic resistance while, at the same time, still allowed testing using GSG probes.

The inductors were designed with a consideration of using them together with capacitor elements having features similar to the vertical RF MEMS capacitors [66] in "all-MEMS" reactive lumped-element low-pass filters. This constrained the inductors to single-turn loops and to similar metal height range as the capacitors.

This was done so that both device types could eventually be processed together using a simple, single metal layer, common-height process, and without the additional requirement for an overpass (or underpass), which would be required to connect to the center of multi-turn inductors, resulting in more complicated processing. Both inductor types were designed with a height of 70 μm. Further, since an inductor can be characterized only by its input admittance (or impedance), both inductor types were designed as one-port devices to simplify the testing process.

The one-loop and two-loop inductors were designed in three loop sizes (small, medium, large) for a total of six devices. The top-view of these inductors is presented in Figure 4.3 and 4.4. The dimensions of the one-loop inductor designs are provided in Table 4.1 with a corresponding map shown in Figure 4.5. The dimensions and map for the two-loop counterparts are given in Table 4.2 and Figure 4.6 respectively.

The length of the inductance loop was selected for nominal inductances of 0.5 nH to 5 nH. This range was chosen to anticipate low-pass filter designs in the 1-10 GHz range. It can be observed from Table 4.1 and 4.2 that the metal width of the inductance loop for the medium and large inductors, both one-loop and two-loop, was chosen to be $50\sqrt{2}$ μm to ensure structural stability. The small inductors; however, had narrower metal widths to maintain as wide a separation as possible between the inductance loop segments, facing each other. In addition, this would also better exemplify the capability of the deep X-ray lithography (DXRL) process

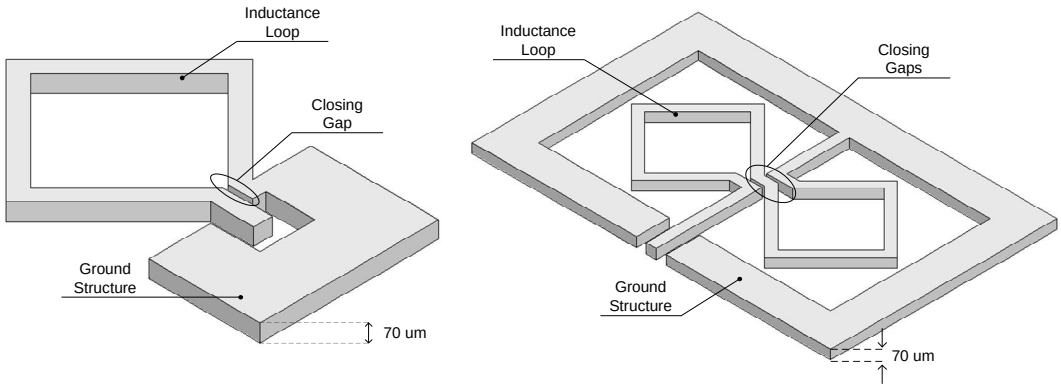

Figure 4.2. Representative 3D view of one-loop and two-loop inductors.

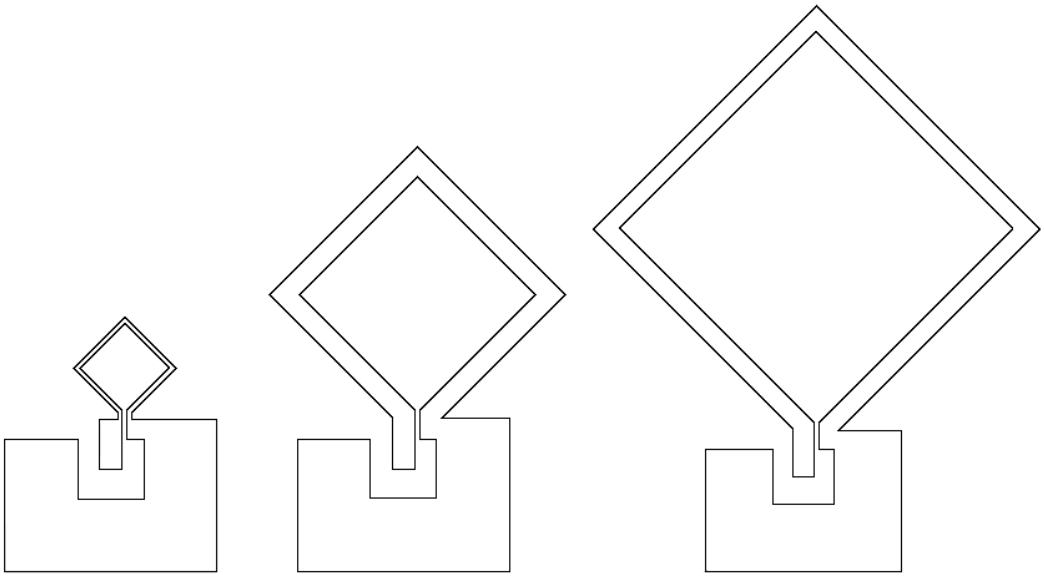

Figure 4.3. Top view of one-loop inductors.

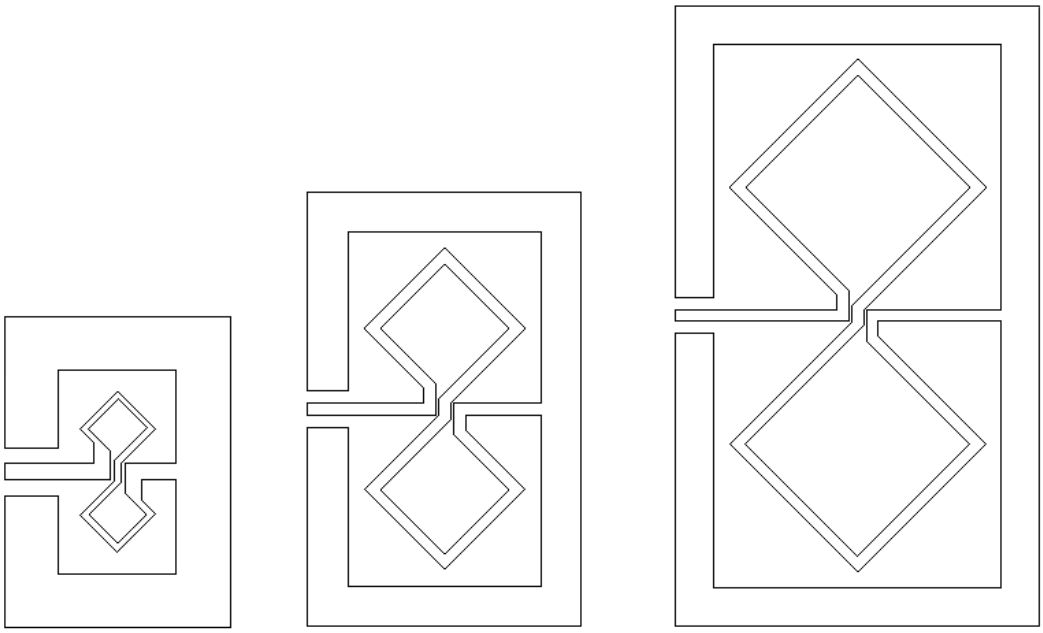

Figure 4.4. Top view of two-loop inductors.

Table 4.1. One-loop inductor dimensions.

Dimensions	1-loop Inductors		
	small	medium	large
Loop length, L_{loop} [μm]	$175\sqrt{2}$	$500\sqrt{2}$	$825\sqrt{2}$
Loop-trace width, W_t [μm]	$10\sqrt{2}$	$50\sqrt{2}$	$50\sqrt{2}$
Device length, L [μm]	870	1440	2090
Closing gap width, W_g [μm]	20		
L_3 [μm]	70		
L_2 [μm]	200		
L_1 [μm]	250		
W_1 [μm]	250		

to produce tall and small structures. The gap closing the square turns was chosen to be 20 μm wide. Ideally this gap should be as small as possible to support increased inductive flux linkage; however, a narrower gap would amplify the parasitic coupling-capacitance and reduce the self-resonant frequency (SRF). Using the Greenhouse method [52] presented in Chapter 2, the small, medium, and large inductors, were expected to give nominal inductance values of 0.3- 0.6 nH, 1- 2 nH, and 2.5- 5 nH

Table 4.2. Two-loop inductor dimensions.

Dimensions	2-loop Inductors		
	small	medium	large
Loop length, L_{loop} [μm]	$175\sqrt{2}$	$500\sqrt{2}$	$825\sqrt{2}$
Loop-trace width, W_t [μm]	$20\sqrt{2}$	$50\sqrt{2}$	$50\sqrt{2}$
Device length, L [μm]	1445	2705	4005
Device width, W [μm]	1050	1705	2350
Closing gap width, W_g [μm]	20		
Ground structure widthW_{gnd} [μm]	250		

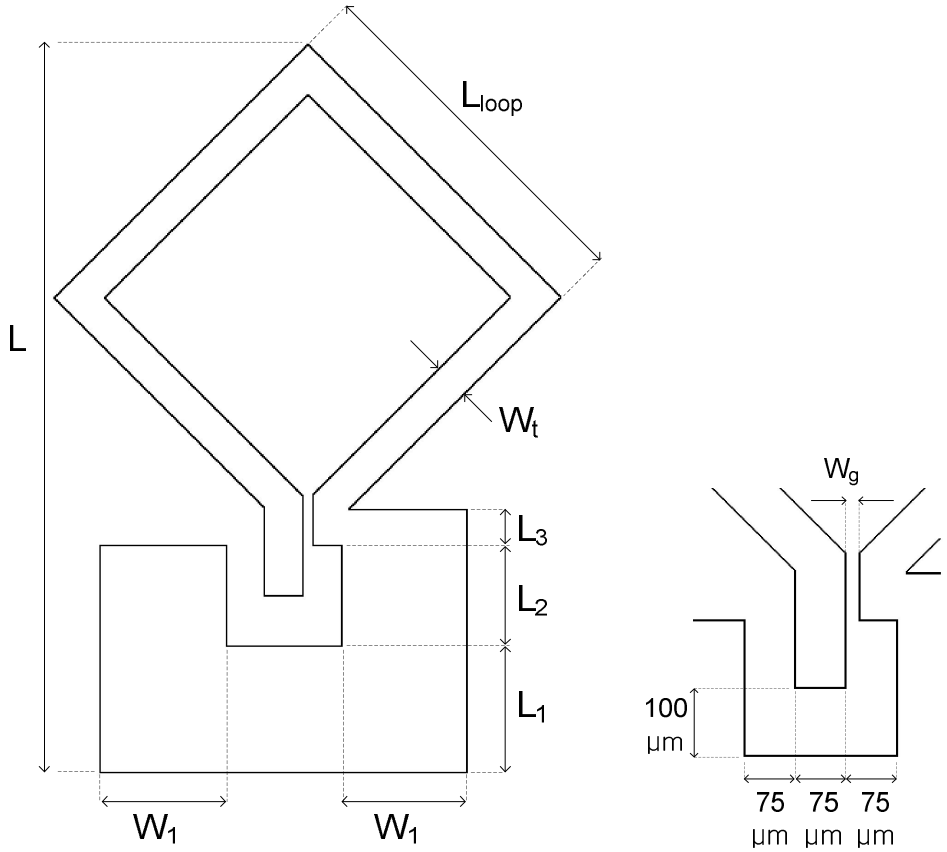

(a) Overview. (b) Middle section.

Figure 4.5. Map of dimensions of the one-loop inductor.

respectively.

The ground structure of the two-loop inductors could introduce additional parasitic inductance and resistance. In addition, there could also be some parasitic capacitances between the ground structure and the square loops. In an effort to reduce these parasitics, the ground structure was chosen to be 250-μm wide at a distance of 100 μm from the square loops.

HFSS simulation models for the one-loop and two-loop inductors are presented in Figure 4.7 and Figure 4.8 respectively, showing both virtual and actual objects. Existing only in the simulation models, the virtual objects in the one-loop inductor model consist of an air box and excitation port, while for the two-loop they consist

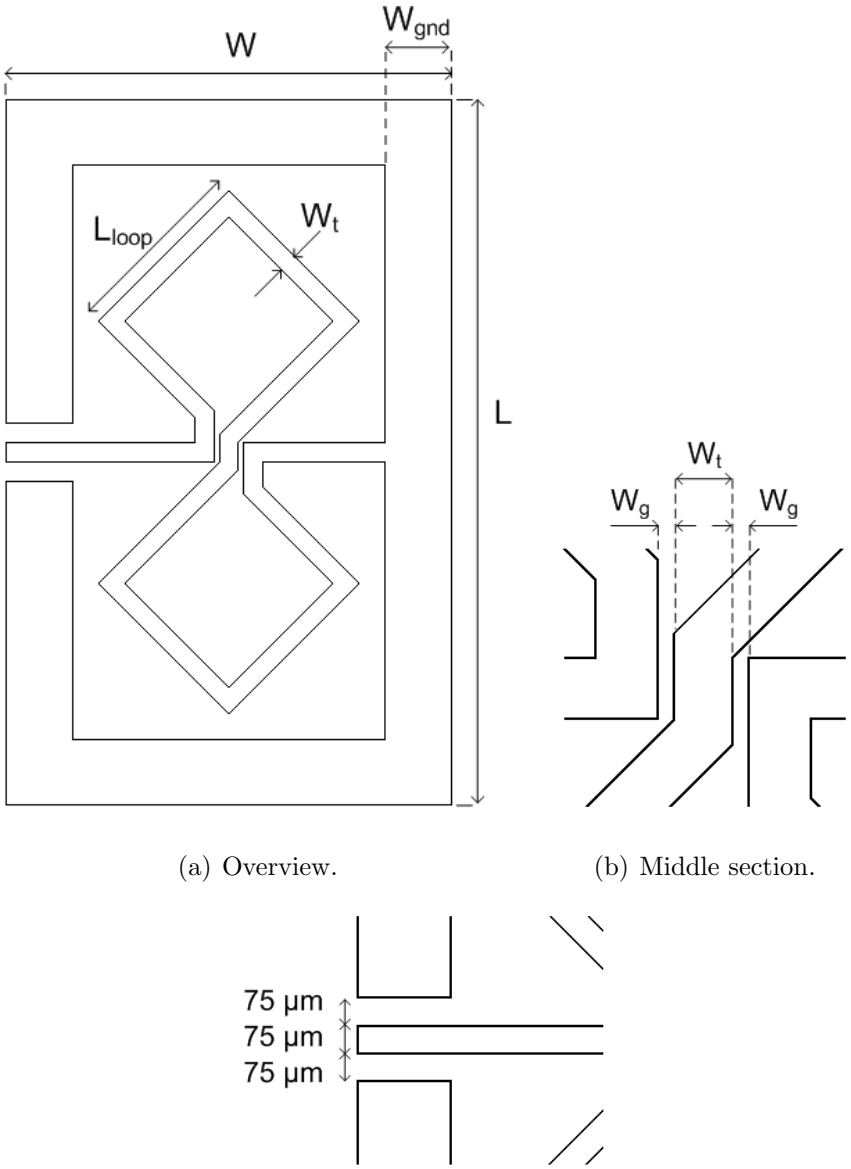

(a) Overview.

(b) Middle section.

(c) Port configuration.

Figure 4.6. Map of dimensions of the two-loop inductor.

of an air box, an excitation port, and a PEC (perfect electric conductor) bridge. The actual objects represent objects that will be present in the device after fabrication which include the inductance loop(s), ground structure, and the substrate.

In HFSS, regions not occupied by any objects in a model are considered as background objects. By default HFSS defines the background objects as perfect

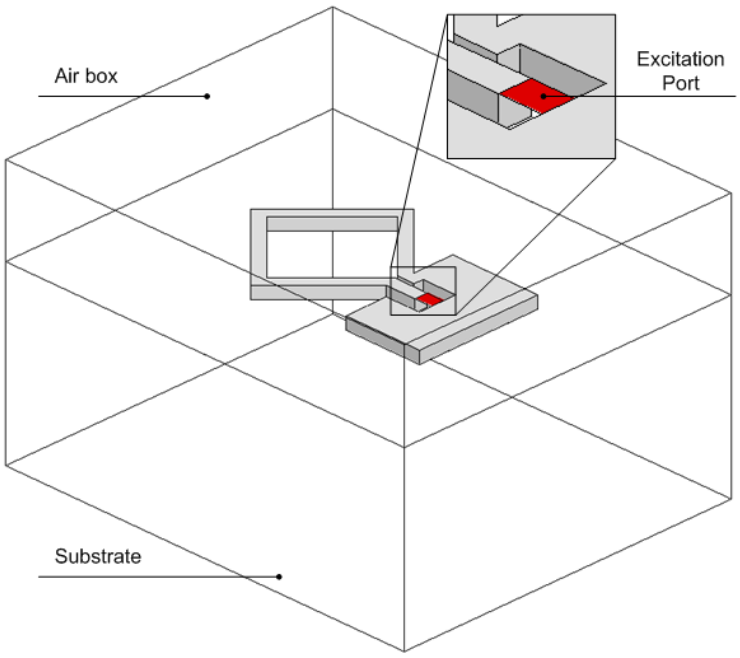

Figure 4.7. Representative HFSS simulation model for one-loop inductors.

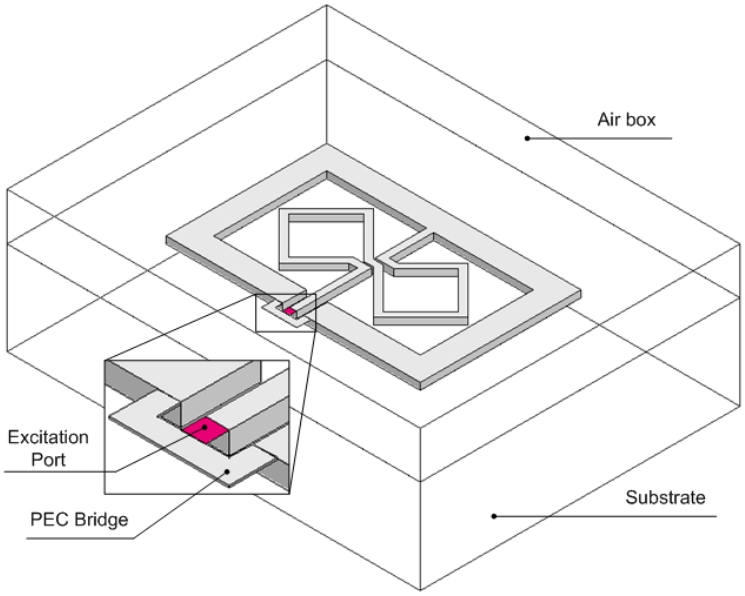

Figure 4.8. Representative HFSS simulation model for two-loop inductors.

conductors and generates no electromagnetic fields inside them [65]. Since the one-loop and two-loop inductors generate fields in their surrounding, they need to be separated from the background objects by placing them inside an air box (a box defined with air as the material). Consequently, the air box becomes part of the HFSS model. Since the air box touches the background object, its surfaces become perfect conductor walls. Therefore, the air box needs to be properly sized such that its walls do not influence the fields inside the box and change the intended behaviour of the inductor structures. Reference [67] suggests that an air box should initially be set a multiple of times bigger than the field-containing volumes in a model. The size is then adjusted as necessary by visualizing the solved fields inside the box. If there is a strong interaction between the perfect conductor walls and the fields, the air box is enlarged.

In order to allow power into and out of the model, a 2-D surface inside both inductor models was defined as an excitation port. A Lumped excitation port was chosen since it simulates measurements gathered by GSG (ground-signal-ground) wafer probes well. Detailed discussions on lumped ports can be found in [68] and some of the important guidelines on port sizing are presented here for convenience. The excitation port has to touch both the inductance loop and the ground structure. The port width should be no larger than the width of the loop trace, W_t, and the port length should be roughly equal to its width. In case of the two-loop inductors, the two ends of the ground structures need to be connected together. In Figure 4.8, this connection is provided by the PEC bridge.

The two inductor types (one-loop and two-loop) were modeled in both nickel and gold on an alumina substrate, and also in nickel on a quartz-glass substrate in HFSS. This was done to observe the effects of metal and substrate materials on the inductor performance. In order to get accurate electromagnetic simulation results it was important that the electrical properties of the materials were defined as realistically as possible. They include the nickel relative permeability and conductivity, gold conductivity, as well as the relative permittivity and loss tangent of alumina and quartz-glass. Unfortunately, it was not known with a high certainty whether the

electrical properties used in the simulations really represented those of the actual materials used in the fabrication, since they can vary with process, especially with electroplating.

In the case of electroplated nickel, a survey of values found in the literature [69] shows that little consensus exists on its magnetic relative permeability and DC bulk conductivity. Reference [69] argues that the initial permeability of nickel approaches unity from a certain dc value as frequency increases. Further, the most prominent variations in nickel initial permeability occurs in the 0.1- 10 GHz range. This decreasing trend of permeability agrees with a collection of measured data published in [70] which is shown in Figure 4.9. Although, the measured data shows large discrepancies, it shows a similar trend, which is a low-frequency value that drops off to less than 2 at about 10 GHz.

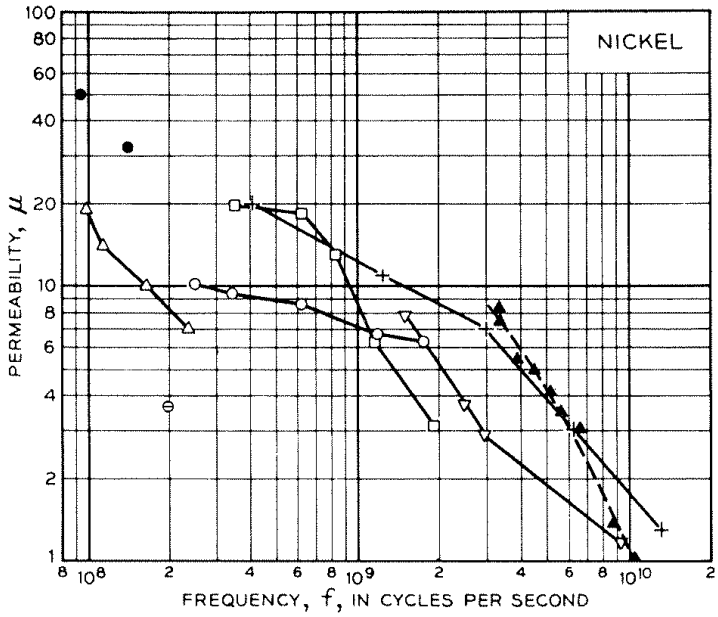

Figure 4.9. Measured frequency characteristics of initial permeability for nickel [70]. (+[71], Δ[72], □[73], •[74]), ⊖[75], ∘[76], ▽[77], ▲[78]).

Relative permeability values used for the simulations in this study are given in Table 4.4. These values were measured data obtained by Hodsman et al. [78] and were chosen because they were roughly in the 1- 10 GHz range. In terms of nickel conductivity, a value of 1.266×10^7 S/m [79] was used. This is a measured conductivity value of electrodeposited nickel from a sulfamate bath, which is similar to electroplating process used in this study. This is slightly lower than the value for bulk nickel from the HFSS library (1.45×10^7 S/m) or typically found in the literature (1.46×10^7 S/m) [80]. For gold, default electrical property values of 4.100×10^7 S/m for conductivity and 0.99996 for relative permeability were used. This conductivity value agrees well with bulk conductivity values typically found in the literature (4.26×10^7 S/m) [80] and with conductivity value for electroplated gold [81].

Default electrical-property values from the HFSS library for both 96% alumina and quartz glass were used in simulations in the current study. Table 4.3 and 4.4 present the electrical properties of the materials used in simulations.

Table 4.3. Electrical properties of materials used in HFSS simulations.

Material	Relative Permittivity ϵ_r	Relative Permeability μ_r	Conductivity σ [S/m]	Dielectric Loss Tangent tan δ
Quartz glass	3.78	1	0	0
Alumina 96%	9.40	1	0	0.006
Nickel	1	see Table 4.4	1.266×10^7	0
Gold	1	0.99996	4.1×10^7	0

Frequency sweeps were performed during the simulations to reveal the frequency characteristics of each inductor. At every frequency point, a scattering parameter, S_{11}, was generated. The input S-parameter, S_{11}, was then transformed to its equivalent input admittance, Y_{11}, which was then used to calculate several inductor

Table 4.4. Measured initial permeability of nickel [78].

Frequency [GHz]	μ_r
DC	17.0
3.356	8.30
3.374	7.50
3.956	5.60
4.545	5.00
5.062	4.10
5.564	3.40
6.522	3.00
8.772	1.50
9.615	1.03
10.084	1.00

performance indices as follow:

$$R = Re\left(\frac{1}{Y_{11}}\right) \tag{4.1}$$

$$L = \frac{X_L}{2\pi f} = \frac{Im\left(\frac{1}{Y_{11}}\right)}{2\pi f} \tag{4.2}$$

$$Q = \frac{X_L}{R} = \frac{Im\left(\frac{1}{Y_{11}}\right)}{Re\left(\frac{1}{Y_{11}}\right)} \tag{4.3}$$

where R is the equivalent resistance (Ω), L is the equivalent inductance in Henry (H), and f is the frequency of interest (Hz). Notice that (4.1) and (4.2) are the equivalent resistance and inductance respectively of the inductor. This means the resistance comprises both the metal and substrate losses, whereas the inductance includes the series inductance and parasitic capacitances of the inductor.

4.3 Fabrication of One-loop and Two-loop Inductors

The inductors were fabricated using deep X-ray lithography (DXRL) processes at the Institute for Microstructure Technology (IMT), Karlsruhe Institute of Technology in Germany. Beamline Litho-2 at the 2.5-GeV electron storage ring ANKA, at the institute, was used to carry out the X-ray exposures.

The first step in the fabrication of the inductors was to design and layout a mask. A picture of the entire mask is given in Figure 4.10. The mask size is (2×6) cm^2 and was shared with another user. The small one-loop and two-loop inductors were included twice to ensure redundancy since they were more structurally demanding than the other inductor designs. Consequently, a total of eight inductors were included on the mask layout.

All corners in the layout drawings of the inductors were rounded to a 5 μm radius. This was done to avoid the PMMA resist from cracking during fabrication and to inhibit point of stress being formed in the electroplated nickel [12, 66, 82]. The rounding of corners was the only distinction between the layout drawings and the top view of the inductor models created in HFSS software.

The one-loop and two-loop inductors were fabricated on both 0.5-mm thick quartz glass and 1-mm thick alumina substrates. A 3-μm titanium layer was sputter-deposited on the substrates and then oxidized for 1.5 minutes. This Ti/TiOx layer acts as an adhesion layer and a seed layer for metal electroplating. A 100-μm thick polymethyl-methacrylate (PMMA) photoresist foil was glued onto the titanium seed layer [11]. The sample was then exposed to X-rays through a 2.7-μm thick titanium mask membrane supporting 25-μm thick gold absorbers. The exposure conditions were adjusted to provide a photoresist bottom dose deposition of 3.5 kJ/cm^3. Following exposure, development was performed in GG developer at room temperature to remove the exposed photoresist. The titanium seed layer was used as a plating base to electroplate nickel or gold to a height of 70 μm in the tall patterned PMMA template. Room temperature electroplating processes were used to reduce thermal distortions which tend to warp tall and very thin PMMA structures [12].

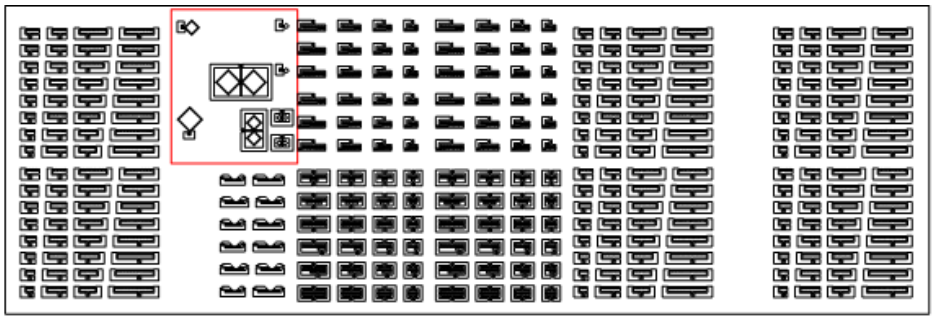

(a) Overview.

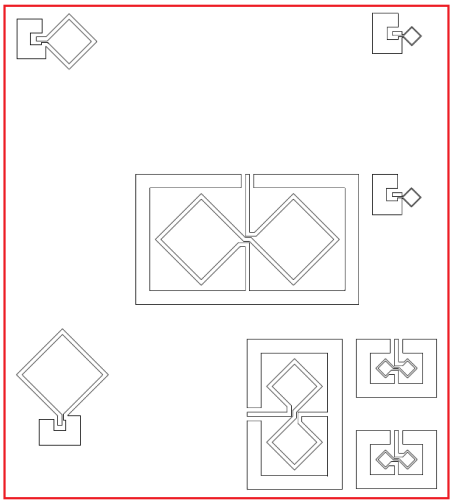

(b) Magnified view of inductors layout.

Figure 4.10. Mask layout of loop inductors.

The structure was then exposed to X-ray flood irradiation, allowing the remaining PMMA to be removed with another step of development. Finally, the structure was wet-etched with 5% HF acid for two to three minutes to remove the seed layer, electrically isolating the structures [12]. Several representative scanning electron micrograph images of the inductors are shown in Figure 4.11-4.14.

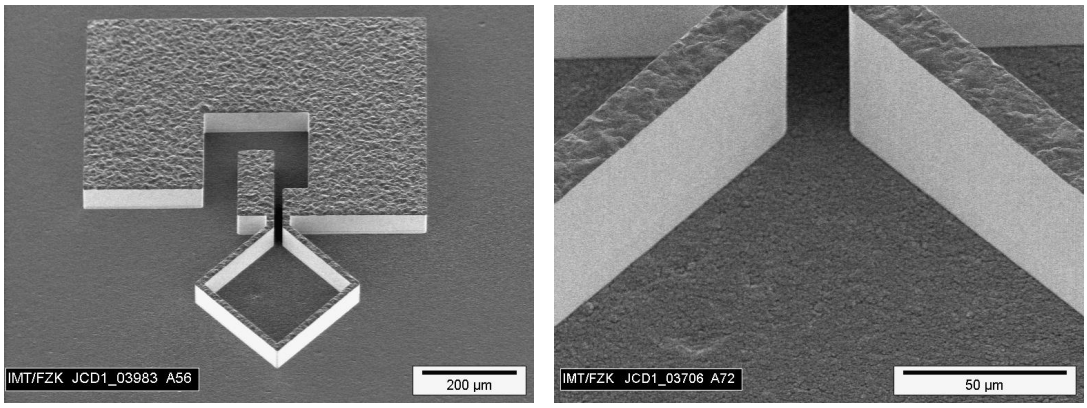

(a) Inclined overview. (b) Magnified view of the gap.

Figure 4.11. Small one-loop inductor fabricated using DXRL (70 μm nickel on alumina) showing structural quality of the tall loop structure (courtesy of IMT).

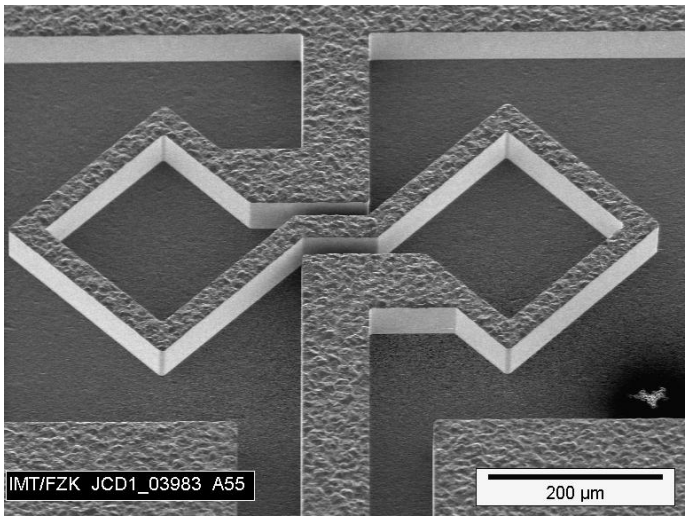

Figure 4.12. Inclined-overview of the small two-loop inductor (70 μm nickel on alumina) (courtesy of IMT).

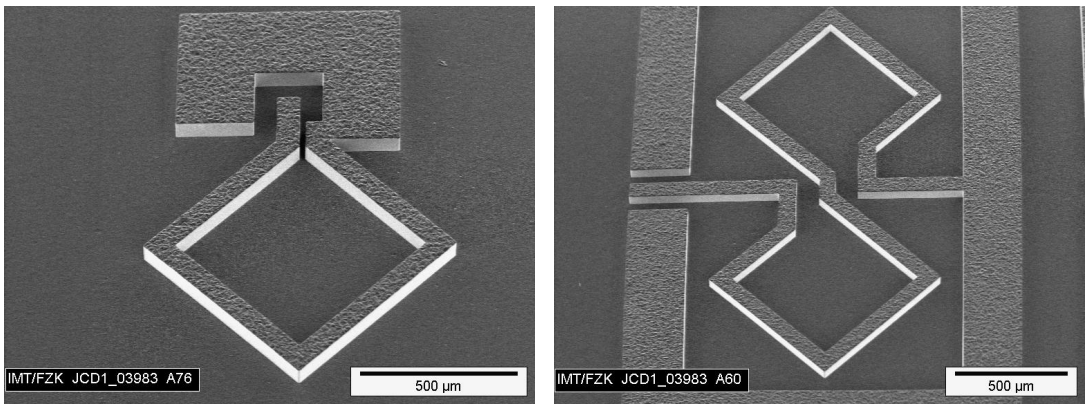

(a) One-loop. (b) Two-loop.

Figure 4.13. Inclined-overview of the medium-size inductors fabricated using DXRL (70 μm nickel on alumina) (courtesy of IMT).

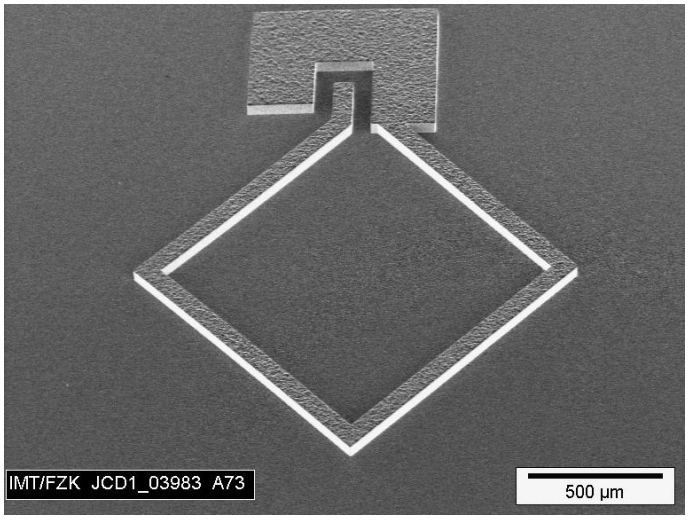

Figure 4.14. Inclined-overview of the large one-loop inductor (70 μm nickel on alumina) (courtesy of IMT).

4.4 Low-pass Filter Design and Structural Models

Two low-pass filters were designed and their frequency responses predicted using Ansoft HFSS. Figure 4.15 shows a representative 3D view of the filter design which consists of an inductance loop and two ground structures. Both low-pass filters were

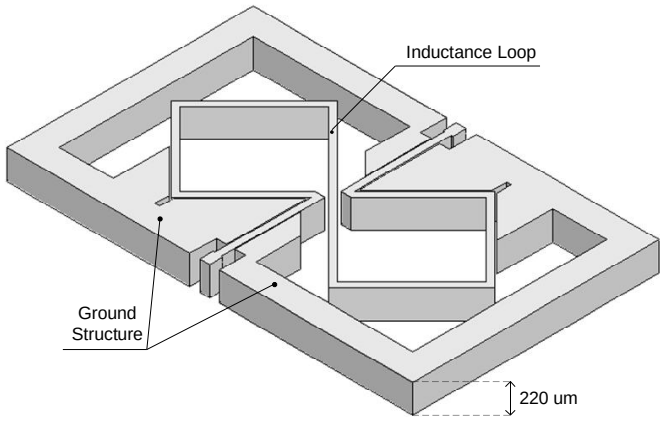

Figure 4.15. Three dimensional view of a low-pass filter.

220 μm tall and featured 8.5-μm wide air gaps obtained by bringing the ground structures very close to the inductance loop. The ground and the inductance loop structures consequently formed two shunt parallel-plate capacitors along the air gaps. This capacitor design uses the capability of deep X-ray lithography (DXRL) to produce tall structures with small lateral dimensions. The filters also had ground structures configured to facilitate testing using GSG wafer probes.

Figure 4.16 shows the top view of the low-pass filters generated in the current study. Both low-pass filters realized a third-order, 0.5-dB ripple Chebyshev response in a capacitor-inductor-capacitor "π" equivalent ladder circuit. Low-pass filter A was designed for a last-ripple frequency of f_{ripple}= 5.1 GHz with a 3-dB frequency of $f_{3\text{dB}}$= 6.7 GHz. Low-pass filter B was designed for a last-ripple frequency of f_{ripple}= 10.8 GHz with a 3-dB frequency of $f_{3\text{dB}}$= 12.9 GHz.

The necessary inductance and capacitance values for the above specifications

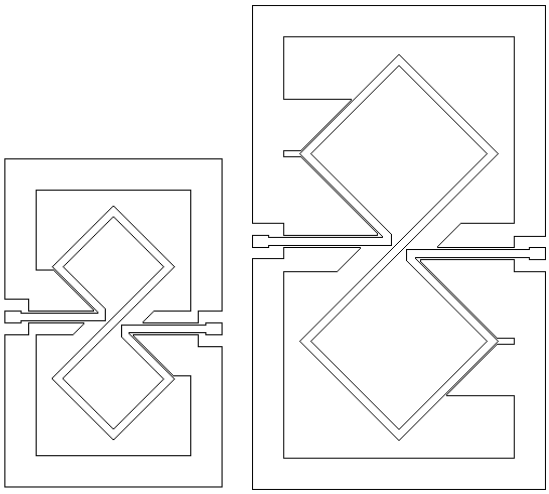

(a) Design A. (b) Design B.

Figure 4.16. Top view of low-pass filters.

were obtained by adjusting the structure dimensions. The dimensions of each low-pass filter structure are given in Table 4.5 with a map of the dimensions shown in Figure 4.17 where the air gap (also the capacitance length) extends from point A to F and from point A' to F'.

Table 4.5. Low-pass filter dimensions.

Dimensions	Design A	Design B
Width, W [μm]	1378	1880
Length, L [μm]	2084	3100
Ground-ring width, W_g [μm]	200	200
Trace width, W_t [μm]	50	50
Inductance-loop length, L_{loop} [μm]	550	900
Air-gap width, W_{gap} [μm]	8.5	8.5
Capacitance length, L_{cap} [μm] *design A*= $\overline{ABCD} = \overline{A'B'C'D'}$ *design B*= $\overline{ABCDEF} = \overline{A'B'C'D'E'F'}$	1120	2250

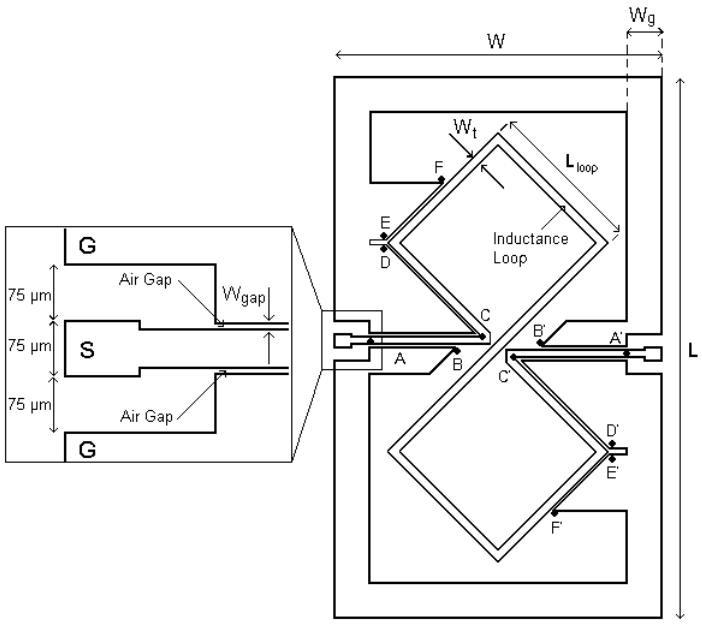

Figure 4.17. Representative top view of the low-pass filters.

The inductive structure in each low-pass filter design was adapted from the two-loop inductor design. The metal width of the inductance loop was 50 μm . Although a wider metal trace would increase structure stability, it will also increase the overall size of the filters. Further, for a given height, conductors with smaller widths give slightly more inductance because they generate more external magnetic flux [49]. With the trace width and the height fixed at 50 μm and 220 μm respectively, the length of the inductance loop (L_{loop}) for a given inductance value was calculated using the method described in Chapter 2. The length of the inductance loop (L_{loop}) for each filter design is provided in Table 4.5. In each design, the capacitive-coupling gaps in the middle of the filter structure were about 21 μm wide. This was to support increased inductive flux linkage while keeping parasitic capacitance low.

The two shunt capacitors are air-dielectric parallel plate capacitors whose capacitance values are approximated by

$$C = \frac{\epsilon_0(length \times height)}{gap\_width} \tag{4.4}$$

where ϵ_0 is the permittivity of free space, *length* and *height* are the length and

height of the parallel plates respectively, and *gap_width* is the separation between the plates (i.e. air gap width). A narrower gap generally produces a bigger capacitance; however, it will make the structures more challenging to fabricate. This is due to increased chances of overpass structures across the gap, creating short-circuit paths. Based on the successfully fabricated gap in [12, 18], the gap width in this design was chosen to be 8.5 μm. Equation (4.4) was then solved for the capacitance length, L_{cap} for a given capacitance. This capacitance length and other dimensions of the LPF design were used as a starting point for HFSS simulations and were adjusted as necessary to account for parasitics present in the structure.

The ground structures provide return paths for the RF signal. Unfortunately, they introduce finite amount of parasitic self-inductances and capacitances. In an effort to minimize these parasitics, the width of the ground structures was made 200 μm while the distance between the ground structures and inductance-loop structure was made approximately 100 μm .

Figure 4.18 shows an HFSS simulation model for low-pass filter design B which, similar to the loop-inductor models, consists of real and virtual objects. The low-pass filter simulation model shown was setup following the same guidelines as those for the two-loop inductor models. These details can be found in Chapter 4.2. Since the low-pass filters were all two-port networks, their simulation models contained two excitation ports and two PEC (perfect electric conductor) bridges. These were the only differences between the low-pass filter and two-loop inductor models.

The meshing size in the simulations varied with the overall size of the models and the desired accuracy. For the low-pass filter design B, a meshing size of approximately 13,000 tetrahedral elements was generated. This meshing size corresponded to a maximum change of S-parameter between iterations of approximately 0.009 in the HFSS adaptive analysis process.

The low-pass filters were modeled in nickel on both alumina and quartz glass substrates to observe substrate effects on a filters performance. The materials used in the low-pass filter simulations had the same electrical-property values as those in the inductor simulations. These electrical property values can be found in

Table 4.3 and 4.4.

The performance of a low-pass filter was evaluated by performing a frequency sweep and plotting the magnitude of the S-parameters in decibels (dB). Of particular interest are S_{11} and S_{21} which represent the input-port voltage reflection coefficient and forward voltage gain respectively. These two parameters can be calculated as follow [54]:

$$|S_{11}|_{dB} = 20\ \log(|S_{11}|_{linear}) \tag{4.5}$$

$$|S_{21}|_{dB} = 20\ \log(|S_{21}|_{linear}) \tag{4.6}$$

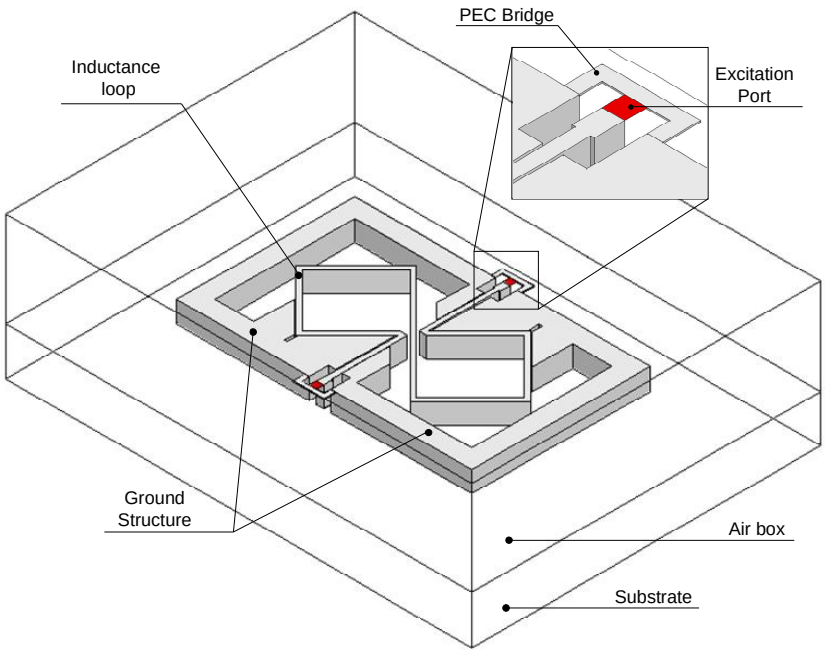

Figure 4.18. HFSS simulation model of low-pass filter design B.

4.5 Fabrication of Low-pass Filters

The overall structure of the low-pass filter designs are generally quite similar to the two-loop inductors. However, the narrow air gap, coupled with the desired structure height, does increase the complexity of the fabrication. In order to increase

the probability of producing deformation-free structures, a few minor modifications were made to layout of the filters. A representative final layout drawing of the filters is shown in Figure 4.19.

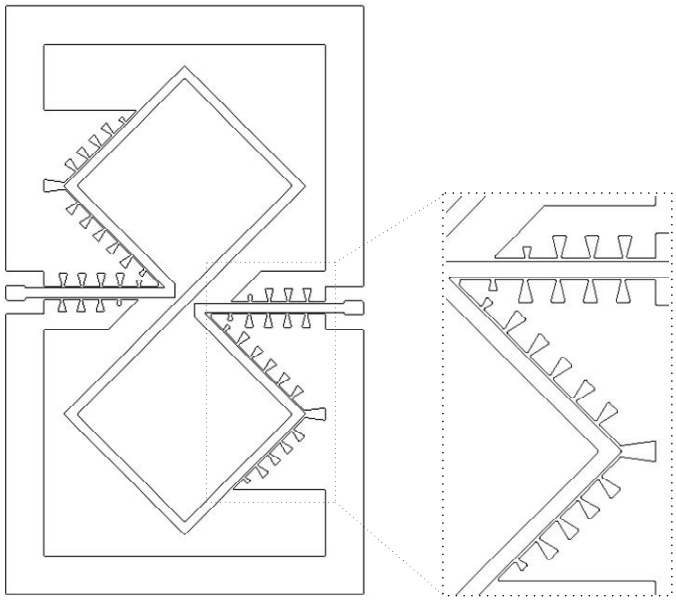

Figure 4.19. Layout drawing of low-pass filter design B.

The first modification was the rounding of all corners in the layouts to a 5 μm radius. This was done for the same reasons as in the loop inductor case. The second modification to the layout was the triangular voids in the ground structures along the air gaps. These triangular voids serve two purposes [12, 66], providing additional support to the tall and narrow PMMA resist structure so it is not deformed or fractured during resist development and metal electroplating and allowing Hydrofluoric (HF) acid to get into the narrow air gap during wet-etching of the seed layer. In general, more voids provide more structural support to the PMMA resist structure; however, they also reduce the effective capacitance length, thus the capacitance value. These two factors consequently govern the size and spacing of the triangular voids. Depending on the location of a triangular void and the available space, the void size could be one of three shown in Table 4.6 and was placed 90- 100 μm apart

from adjacent ones. A representative figure of the triangular void is shown in Figure 4.20.

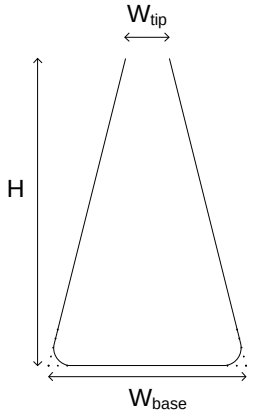

Figure 4.20. Representative figure of the triangular voids used in the layout.

Table 4.6. Dimensions of triangular voids.

	Void 1	Void 2	Void 3
W_{tip} [μm]	33.3	10.0	10.0
W_{base} [μm]	63.3	45.0	27.5
H [μm]	108	70.0	35.0

The low-pass filters were fabricated in a similar manner to the loop inductors on both 0.5-mm thick quartz glass and 1-mm thick alumina. In this case, a thicker 340-μm thick polymethyl-methacrylate (PMMA) photoresist was glued onto the seed layer. The resulting voids in the resist were then electroplated with nickel to a height of 220 μm. The LPFs are produced only in nickel, not only because they are more structurally demanding than the inductors, but also because IMT has a well-developed nickel electroplating process and considerable experience

in producing well-structured devices in nickel. From an RF perspective, higher electrical-conductivity, such as gold or copper, are expected to have lower metal loss. High-temperature electroplating processes at 52 °C were initially performed; however, visual inspections using a scanning electron microscope (SEM) showed structural deformations in the tall and narrow PMMA structures. These deformations could be attributed to thermal distortions and increased PMMA water uptake and swelling in the electrolyte [12]. Figure 4.21 presents an SEM image of low-pass filter design A and illustrates one of the most severe deformations. The room-temperature electroplating processes, later opted, successfully reduced the amount of deformations, resulting in significant improvements to the structural quality of the low-pass filters. Representative SEM images of these higher-quality filters are shown in Figure 4.22- 4.25. The brighter regions in the figures represent smooth sidewall surfaces, a typical characteristic of DXRL-fabricated structures.

Although the deformations were reduced, unfortunately slight variations in the structure height and air gap still existed. From measurements, the structure height varied between 203- 285 μm, while the air gap width ranged from 6- 6.5 μm. In the original design, the height and the air gap width were 220 μm and 8.5 μm respectively.

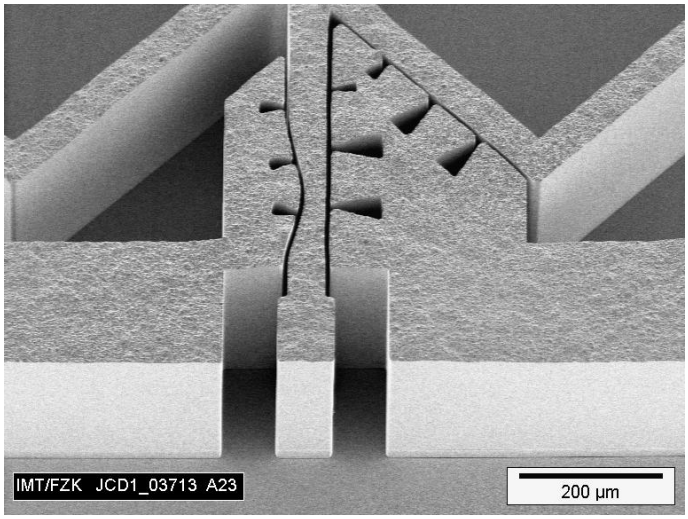

Figure 4.21. Filter structure fabricated using high-temperature electroplating process showing a structural deformation (courtesy of IMT).

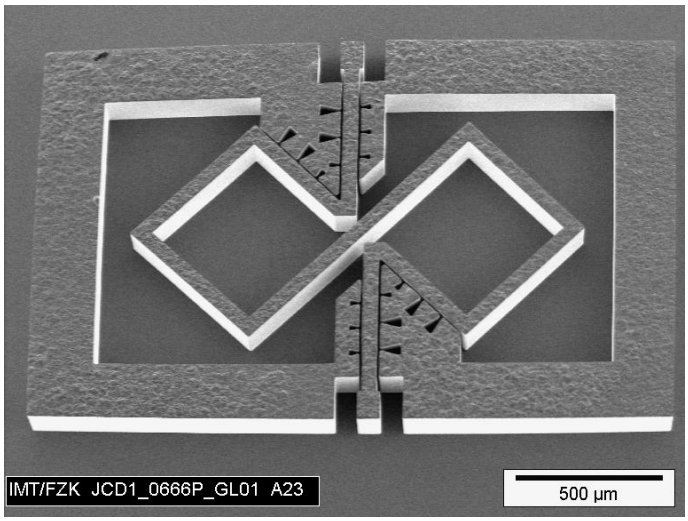

Figure 4.22. Overview of LPF design A (nominal 212 μm nickel on quartz glass) with room temperature electroplating showing little structural deformations (courtesy of IMT).

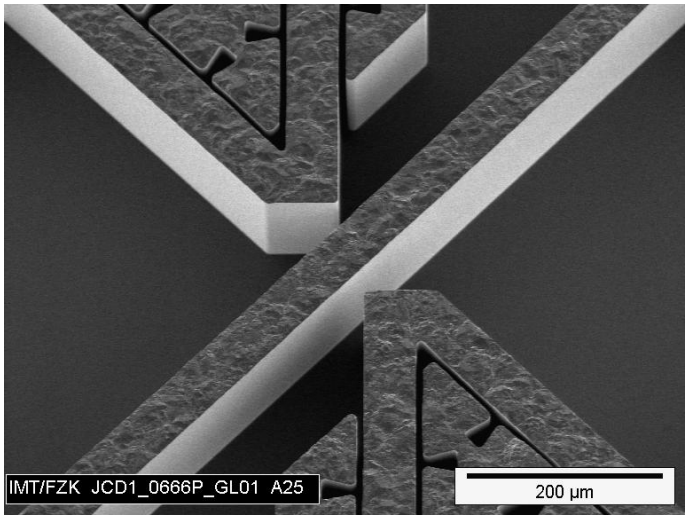

Figure 4.23. Magnified view of middle section of LPF design A highlighting high aspect-ratio capacitive-coupling air gaps (aspect ratio 33:1 in 212 μm nickel) (courtesy of IMT).

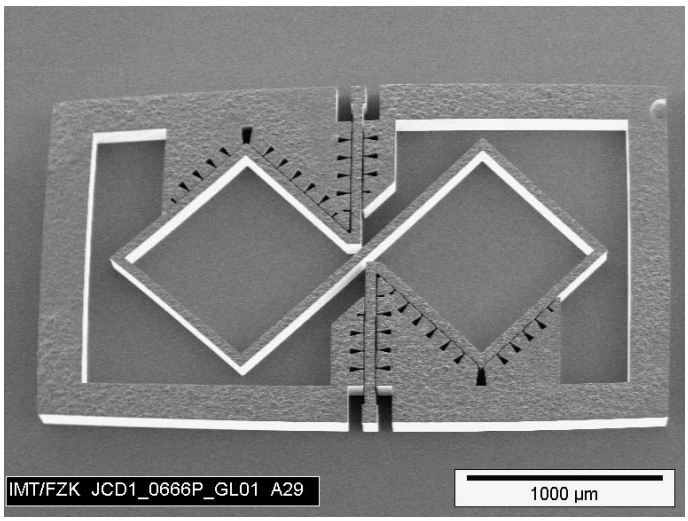

Figure 4.24. Overview of LPF design B (nominal 203 μm nickel on quartz glass) with room temperature electroplating showing little deformations (courtesy of IMT).

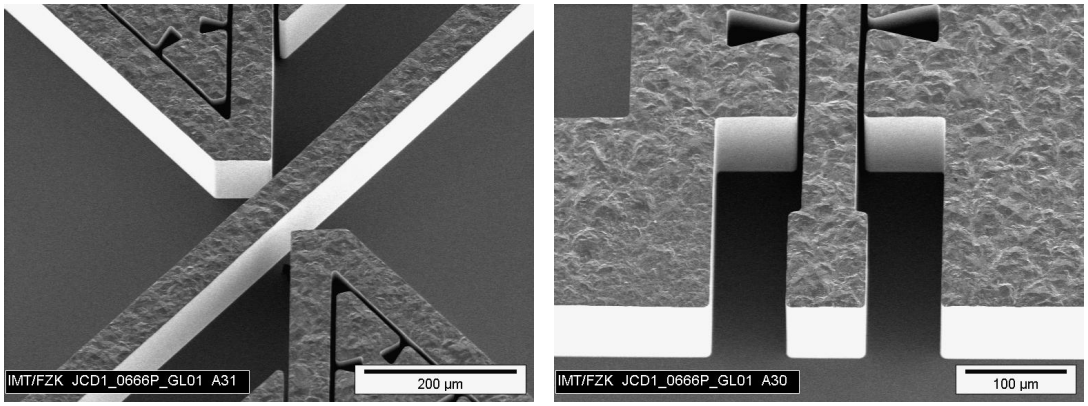

(a) Middle section. (b) Capacitive coupling air gaps.

Figure 4.25. Magnified views of LPF design B (gap aspect ratio 32:1 in 203 μm nickel) (courtesy of IMT).

5. RESULTS AND DISCUSSION

5.1 Test Environment Overview

The fabricated inductors and filters were tested using an Agilent 8722ES vector network analyzer (VNA). It has an operating frequency range of 50 MHz to 40 GHz and supports full two-port S-parameter measurements. Connections between the VNA and the inductors/filters were established using coaxial cables, terminated with wafer probes.

The wafer probes were ACP40-W-GSG-150 from Cascade Microtech Inc. Each probe tip consists of three legs, made of tungsten, in a ground-signal-ground (GSG) configuration with a pitch (centre-to-centre distance between adjacent probe legs) of 150 μm and a maximum operating frequency of 40 GHz. The probes were placed on micropositioners to allow fine positioning of the probes onto the inductor/filter under test. Figure 5.1 shows a picture of a probe on a micro-positioner and the tip of the probe.

In order to eliminate error introduced by the coaxial cables and the wafer probes, calibration of the test setup was performed. Short-open-load (SOL) and short-open-load-thru (SOLT) calibration procedures [83, 84] were used for the inductor and filter measurements respectively. Both procedures were carried out using a Cascade Microtech 101-190 impedance standard substrate (ISS) which provided the short, load, and thru standards. The open standard was applied with the probes in the air.

In the case of inductors, after the SOL calibration procedures were performed, the probe was set down onto the inductor using the positioner. Visual control of the probe was performed through a stereo microscope manufactured by Vision

Engineering. Once a good contact between the inductor-under-test and the probe was obtained, the measured one-port S-parameter from the VNA was acquired. Measurements of the low-pass filters were carried out with the same steps using two wafer probes. Figure 5.2 shows a snapshot of the test setup for the inductors while Figure 5.3 shows a picture of a probe touching an inductor and a filter.

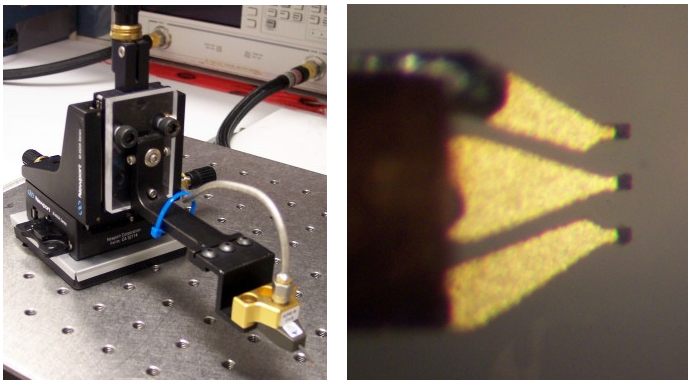

(a) On a micro-positioner. (b) GSG tip configuration.

Figure 5.1. Wafer probe.

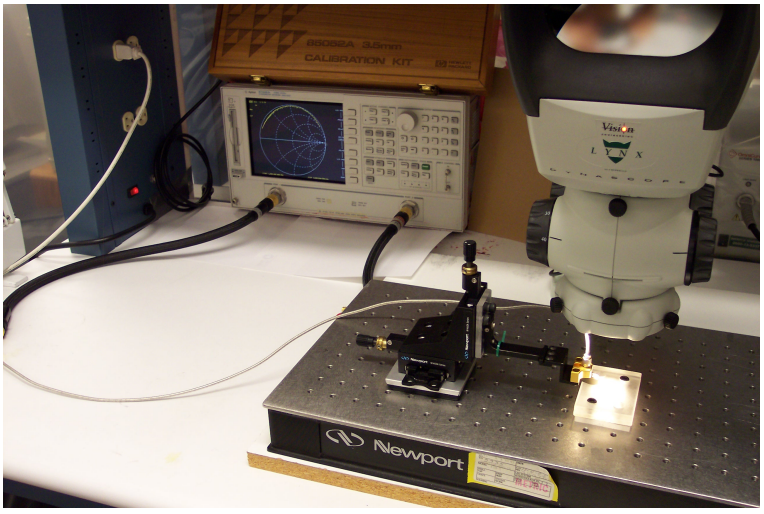

Figure 5.2. Test setup for a one-port S-parameter measurement of an inductor.

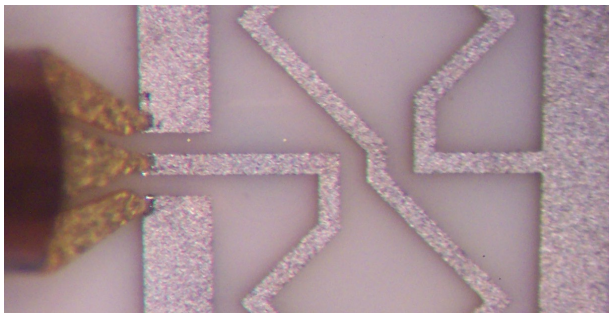

(a) Inductor-under-test.

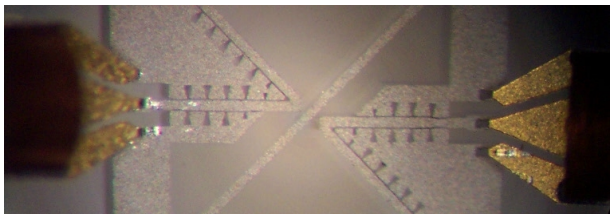

(b) Low-pass filter-under-test.

Figure 5.3. Wafer probes making a contact with a device-under test.

5.2 Loop Inductor Simulation and Measurement Results

Three inductor samples were produced which included nickel and gold inductors on an alumina substrate and nickel inductors on a quartz glass substrate. Inductor performance parameters presented in this thesis were calculated using the formulas given at the end of Chapter 4.2 with a frequency span for each inductor chosen to capture a typical 25-100 Ω inductive reactance range, while ensuring the span did not exceed the maximum frequency rating of the test setup of 26.5 GHz. For clarity, representative results for only the nickel inductors on an alumina substrate are presented in the main thesis, and comparisons between the different samples are done using only the medium-sized 1-loop and 2-loop inductors. Complete results for other inductors can be found in Appendix B.

The measurement and simulation results for the small, medium, and large 1-loop nickel inductors on an alumina substrate are presented in Figure 5.4- 5.6 respectively.

The inductive reactances shown in the figures are the total reactances, and include parasitic capacitive reactances in each inductor. Both the measured and simulated inductive reactances of each inductor demonstrate an increasing trend with frequency and agree to each other reasonably well. This agreement is especially true at lower frequencies such as in the large inductor and in the lower frequency region of the medium inductor. As the frequency increases, the measured and simulated reactances begin to differ which can be observed in the small inductor case and in the higher frequency region of the medium inductor. This discrepancy may be attributed to parasitic capacitances which have more effects at higher frequencies. Since inductive reactance and inductance are proportional to each other, the inductance of each 1-loop inductor also shares the same trend as the inductive reactance when plotted against frequency.

The resistances presented in Figures 5.4- 5.6 are the real component of the inductors input impedances and represent the combination of metal and substrate losses. The resistances have a trend that increases with frequency which can be attributed to the skin effect that worsens as the frequency increases. In addition, the trend also represents dielectric loss through the substrate that becomes more severe at higher frequencies, increasing the total energy dissipated from the inductor. At lower frequencies, the measured and simulated resistances of the medium and large 1-loop inductors agree to each other well. However, the measured resistances increased faster than the simulated values for both inductors. The measured resistance of the medium 1-loop inductor differs by 64% from the simulated value at its operating frequency, f_0 (frequency at which the inductive reactance is equal to 50 Ohm). For the large 1-loop inductor, this difference between the measured and simulated resistances is about 38%. In the case of the small 1-loop inductor, the measured resistance is slightly higher than the simulated value in the lower frequency region. As the frequency increases, the measured resistances increase at a slower rate than the simulated values, an opposite trend to that in the medium or large inductor. The measured resistance of the small 1-loop inductor differs by 18% from the measured value at its operating frequency.

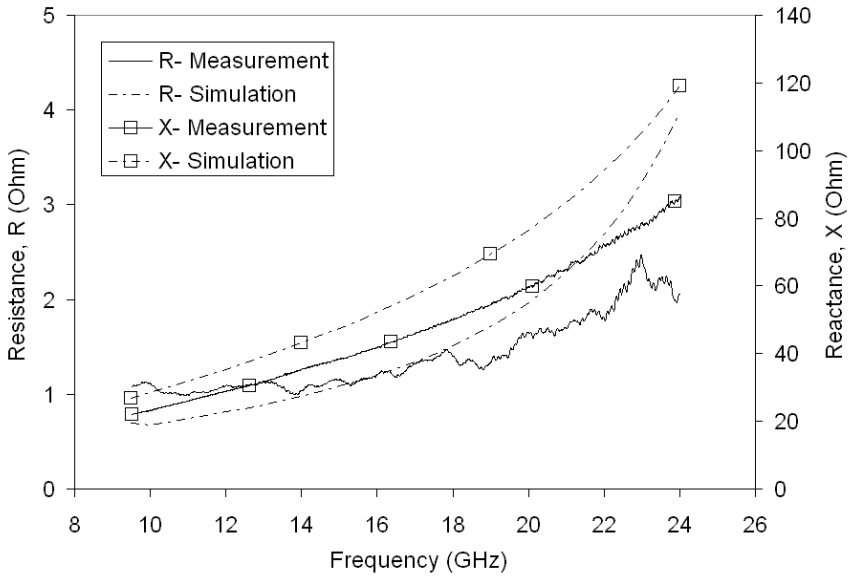

(a) Resistance and inductive reactance.

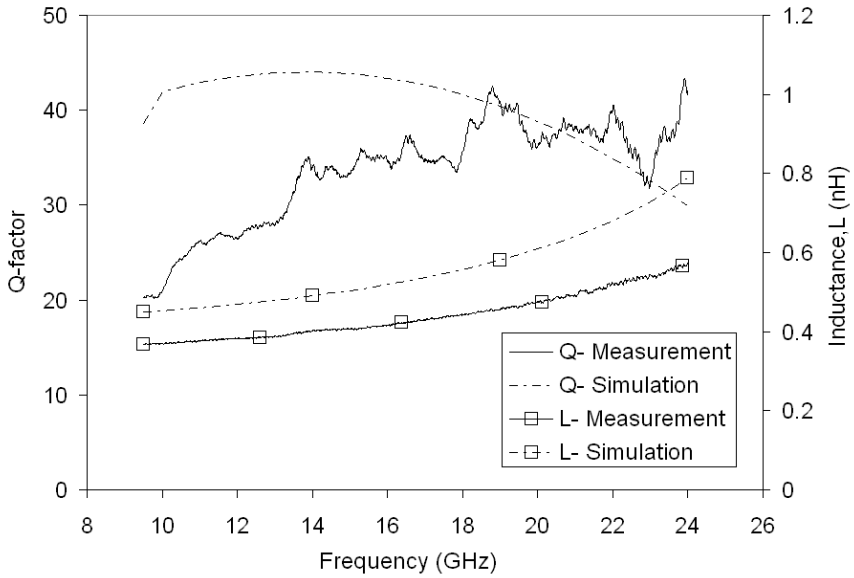

(b) Q-factor and inductance.

Figure 5.4. Inductor parameters of small 1-loop inductor (nickel on alumina).

The Q-factors of all the 1-loop inductors show a peak, which is in agreement with the background theory in Section 2.1.3. Since the Q-factors were obtained by taking the ratio between the inductive reactance, X_L and resistance, R, any

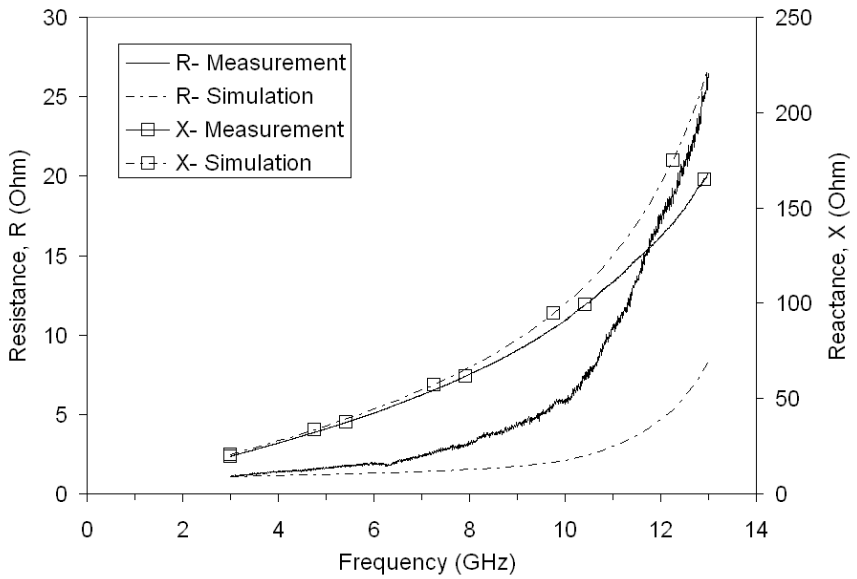

(a) Resistance and inductive reactance.

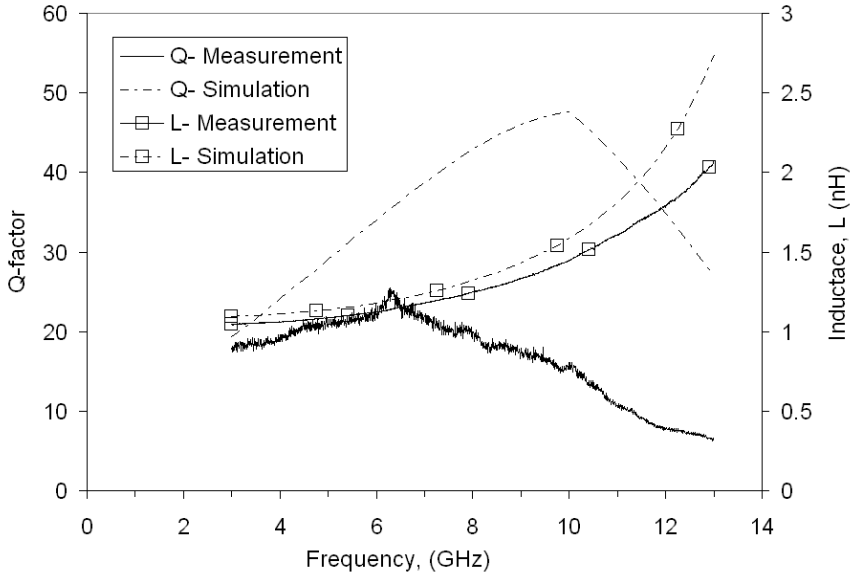

(b) Q-factor and inductance.

Figure 5.5. Inductor parameters of medium 1-loop inductor (nickel on alumina).

differences between the measured and simulated X_L and R would make measured and simulated Q-factors to be different. This is noticeable in the small and medium 1-loop inductors shown in Figures 5.4 and 5.5 respectively. For the large 1-loop

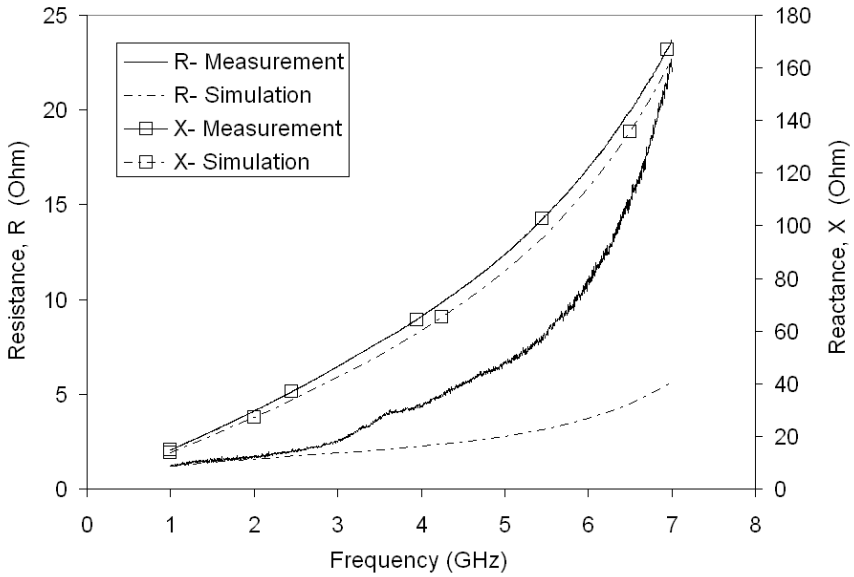

(a) Resistance and inductive reactance.

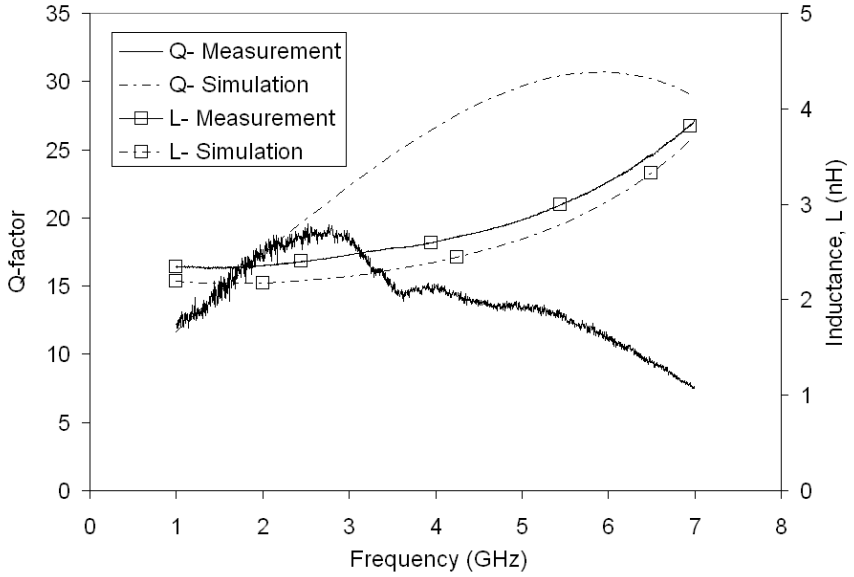

(b) Q-factor and inductance.

Figure 5.6. Inductor parameters of large 1-loop inductor (nickel on alumina).

inductor, the measured Q-factor agrees well with the simulated value in the lower frequency span but is somewhat different than predicted from simulation at higher frequencies.

The differences in the resistances, thus Q-factors, could possibly be related to a few factors. The 1-loop inductors are meant to operate at high frequencies. Unfortunately, measurements at high frequencies are susceptible to parasitic effects, leading to measurement errors. In addition, the resistance of each 1-loop inductor is small which amplifies the effects of the measurement errors. Another possible cause was the indirect measurements of the resistance values. The network analyzer measured voltage reflection coefficients which were then transformed to impedances. At high frequencies, a slight change in the reflection coefficient can translate to a considerable amount in the associated resistance. Another contributing factor could be the inaccurate values of material properties in the simulation. The electrical conductivity and relative permeability of nickel used in this study were based on measured data from [79, 78]. However, as explained in Chapter 4, they may not exactly be the actual values. In addition, electrical properties of alumina would also affect the simulation results due to the electromagnetic fields penetrating the substrate. The current study used the electrical properties of alumina from the material library of HFSS software.

Using the medium 1-loop as an example, the effects of material properties on the inductor response are observed through simulations and are shown in Figure 5.7. The modified simulations used a relative permeability of $\mu_r = 10$ for nickel and a loss tangent of $tan\,\delta = 0.06$ (10 times bigger than the value in the HFSS library) for alumina. Figure 5.7 shows that the material properties have a marginal influence on the reactance. However, they considerably affect the resistance, leading to a better agreement between the measurement and simulation values. While the material properties may be an exaggeration and still not represent the actual values, Figure 5.7 does demonstrate the impact they could have on the simulation results. More comprehensive characterization of the electrical properties may lead to a better agreement between measurement and simulation results.

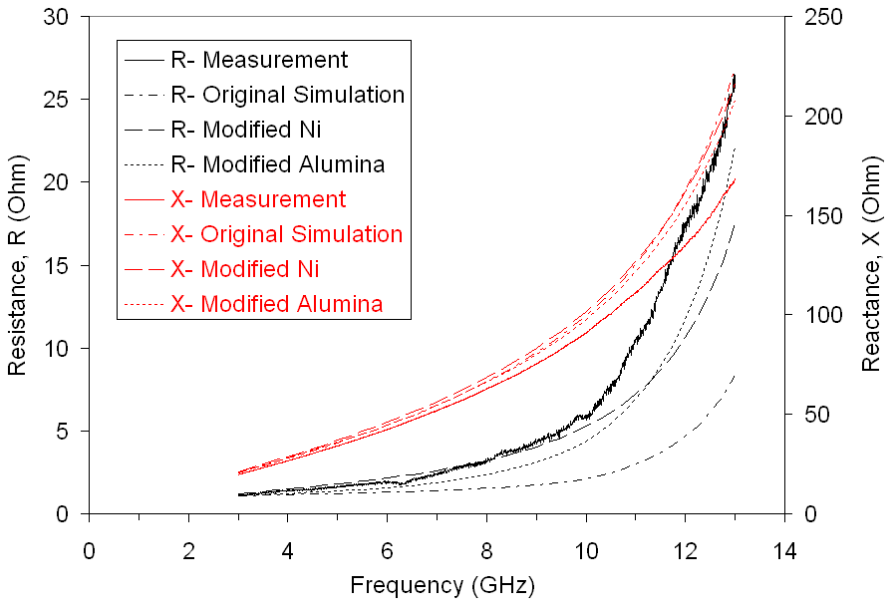

Figure 5.7. Effects of material properties on the simulation results of medium 1-loop nickel inductor on an alumina substrate.

The self-resonant frequency (SRF) measurements were performed separately from the ones done for Figures 5.4- 5.6. These measurements were performed at sufficiently high frequencies to allow the reactance (imaginary component of the impedance) to transition from a positive to negative value. The self-resonant frequency was the frequency at which the reactance became zero. Table 5.1 presents the SRF and other performance parameters of the 1-loop nickel inductors on an alumina substrate.

The measurement and simulation results for the small, medium, and large 2-loop nickel inductors on an alumina substrate are presented in Figures 5.8- 5.10 respectively. The measured and simulated reactance values agreed very well at low frequencies. This is apparent from the large 2-loop inductor and the low frequency portion of the medium 2-loop inductor. At high frequencies, the measured and simulated values begin to differ. As the frequency increases, the reactances of the measured small and medium 2-loop inductors increase slower than predicted from

Table 5.1. Performance parameters of the 1-loop nickel inductors on an alumina substrate (Meas.= measurement values, Sim.= simulation values).

Type		Operating Frequency (f_0, GHz) @ $X_L = 50\,\Omega$	Inductance L (nH) @ f_0	Resistance $R\,(\Omega)$ @ f_0	Q-factor @ f_0	Self-resonant Frequency SRF (GHz)
Small	Meas.	18	0.44	1.3	39	> 26.5
	Sim.	16	0.51	1.1	44	> 26.5
Medium	Meas.	6.8	1.2	2.3	22	17
	Sim.	6.6	1.2	1.4	37	16
Large	Meas.	3.2	2.5	2.9	17	11
	Sim.	3.5	2.3	2.1	24	10

simulations. This difference may be caused by parasitic capacitive reactance that has more effect with increasing frequencies. The inductance values of the inductors also have the same trend as the reactance values.

The measured resistance, thus Q-factor, of the small 2-loop inductor is somewhat different from that predicted from simulation. As shown in Figure 5.8, initially the measured resistance increases faster than the simulated value; however, this trend reverses as the frequency increases. At its operating frequency, the measured resistance of the small 2-loop inductor is different from the simulated value by approximately 63%. In the case of the medium 2-loop inductor, there is a better agreement between the measured and simulated resistances as well as Q-factors, especially at low frequencies where both values almost overlap. The measured resistance only differs by 3% from the measured value at its operating frequency. In the case of the large 2-loop inductor, Figure 5.10 shows that the resistance values demonstrate an even better agreement between measurement and simulation results. Operating in a lower frequency range than the other 2-loop inductors, the large inductor has simulated and measured resistances that differ by 2% at its operating frequency. A good

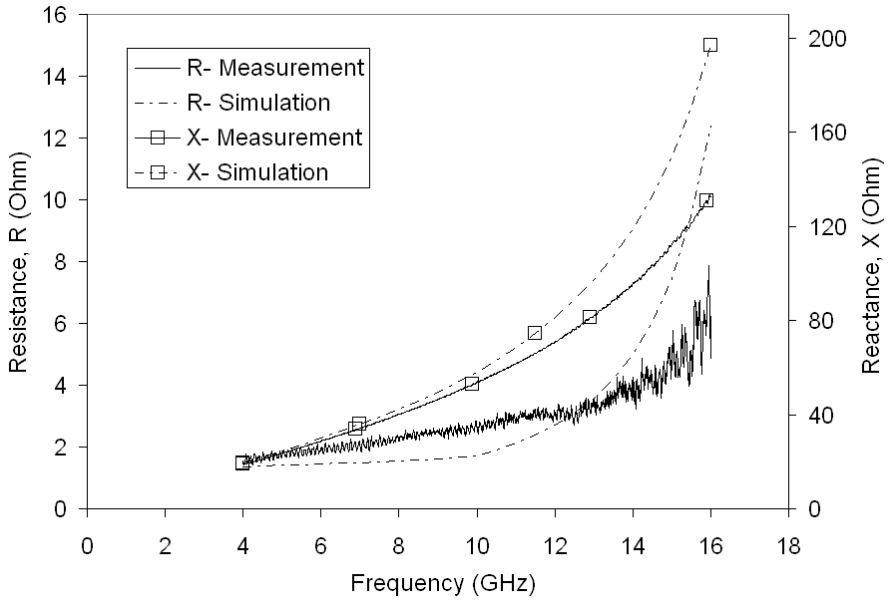

(a) Resistance and inductive reactance.

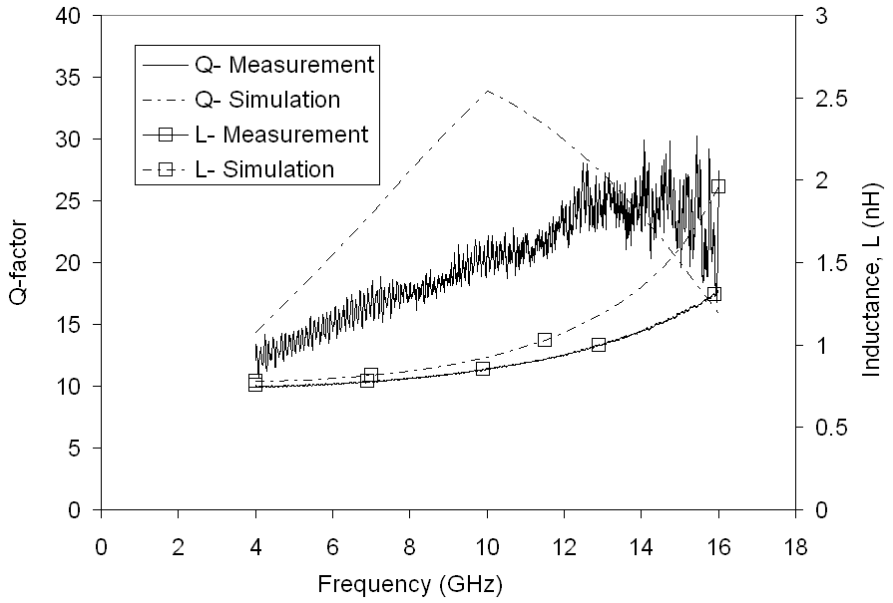

(b) Q-factor and inductance.

Figure 5.8. Inductor parameters of small 2-loop inductor (nickel on alumina).

agreement between the measurement and simulation results can also be observed in the Q-factor.

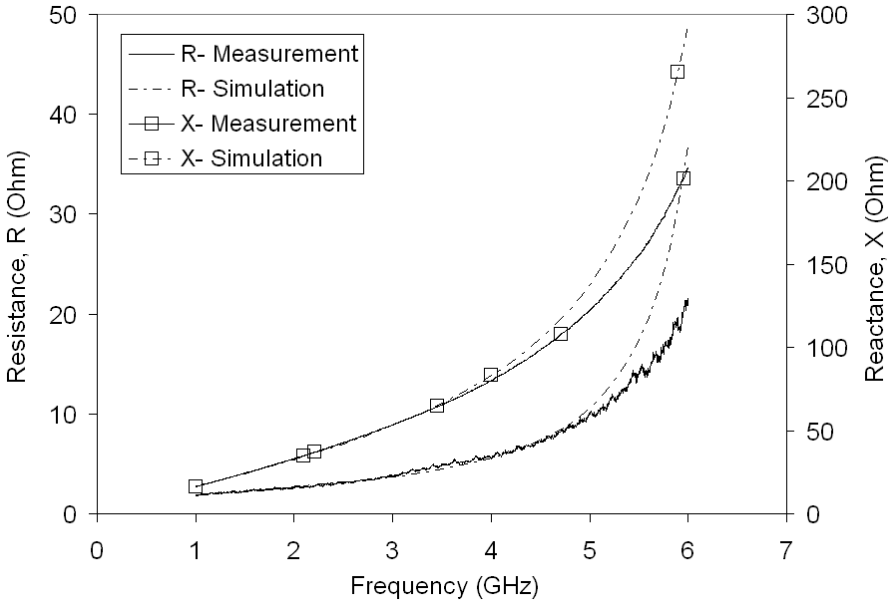

(a) Resistance and inductive reactance.

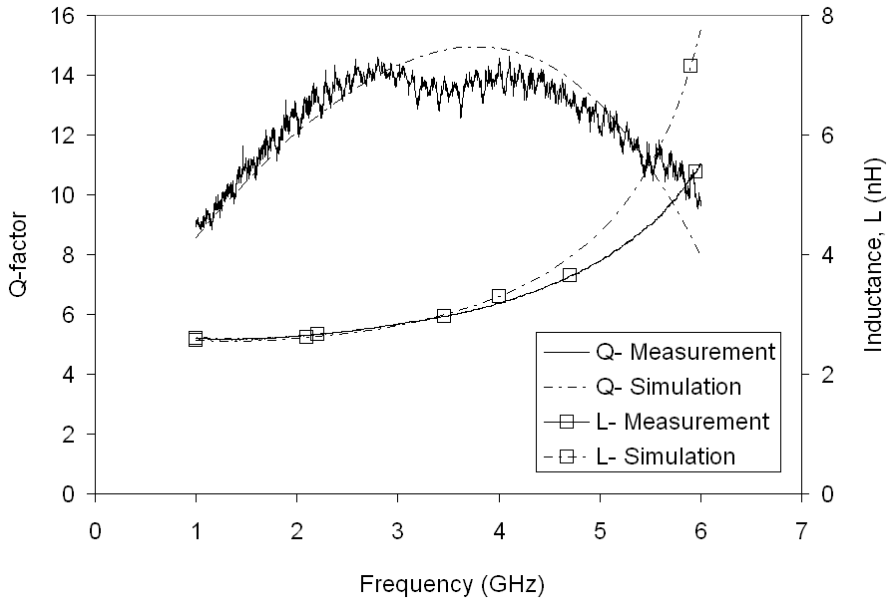

(b) Q-factor and inductance.

Figure 5.9. Inductor parameters of medium 2-loop inductor (nickel on alumina).

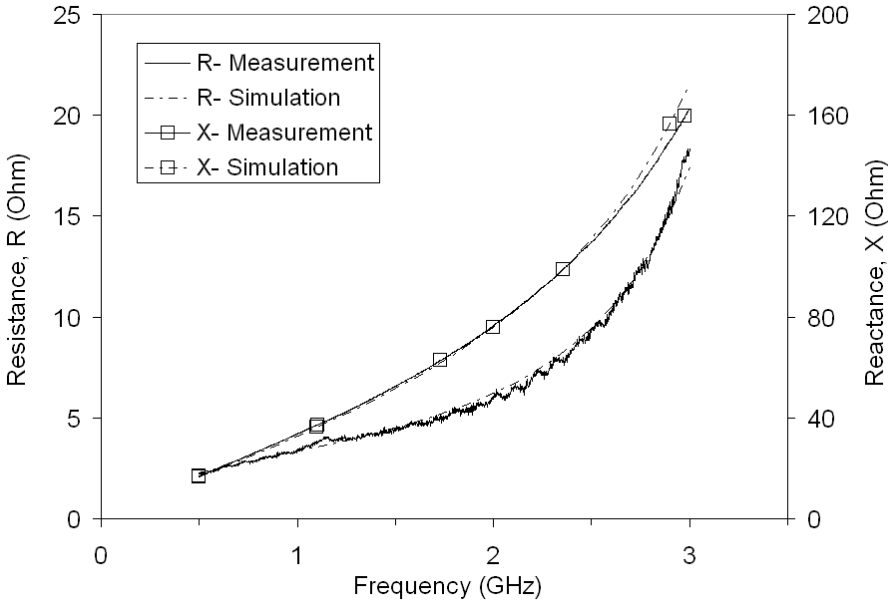

(a) Resistance and inductive reactance.

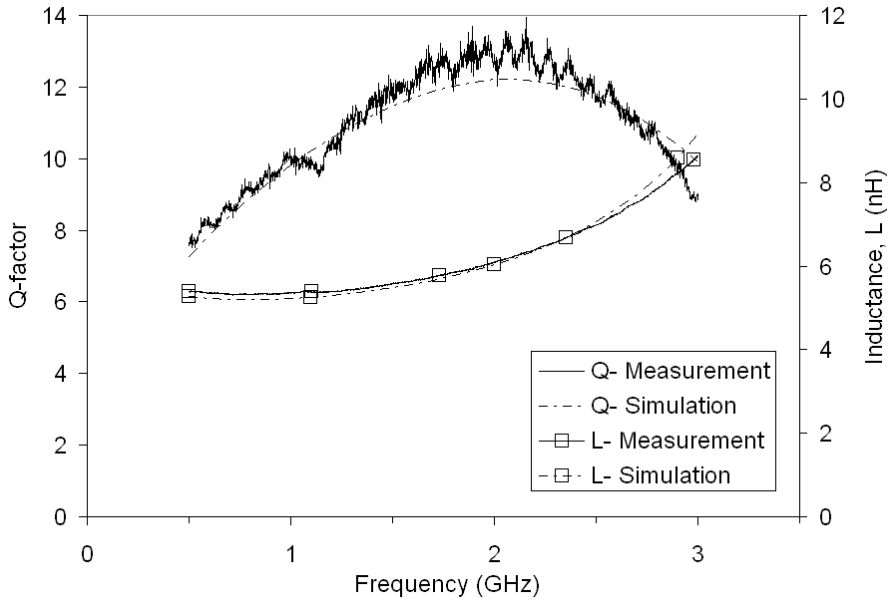

(b) Q-factor and inductance.

Figure 5.10. Inductor parameters of large 2-loop inductor (nickel on alumina).

The self-resonant frequency measurements for the 2-loop inductors were done following the same procedures as for the 1-loop inductors. The SRF and other performance parameters of the 2-loop nickel inductors on an alumina substrate are presented in Table 5.2.

Table 5.2. Performance parameters of the 2-loop nickel inductors on an alumina substrate (Meas.= measurement values, Sim.= simulation values).

Type		Operating Frequency (f_0, GHz) @ $X_L = 50\,\Omega$	Inductance L (nH) @ f_0	Resistance $R\,(\Omega)$ @ f_0	Q-factor @ f_0	Self-resonant Frequency SRF (GHz)
Small	Meas.	9.5	0.84	2.6	20	22
	Sim.	9.1	0.88	1.6	31	19
Medium	Meas.	2.8	2.8	3.6	14	7.7
	Sim.	2.9	2.8	3.5	14	7.0
Large	Meas.	1.4	5.5	4.3	12	4.4
	Sim.	1.5	5.5	4.4	11	4.1

The measurement results for the medium 1-loop and 2-loop inductors with different metals and substrate materials are presented in Figures 5.11 and 5.12 respectively. At low to medium frequencies, the metal type has a significant effect on the parasitic resistance and quality factors of the inductors. Due to a higher conductivity, both the 1-loop and 2-loop gold inductors demonstrate lower parasitic resistance, thus higher Q-factors than the nickel counterparts. The metal type, however, almost has no effects on the inductive reactances or the self-resonant frequencies of the inductors. The similarity between the self-resonant frequencies of the gold and nickel inductors can also be observed in Table 5.3.

At high frequencies, the inductor on a quartz glass substrate has a lower parasitic resistance than those on alumina substrates. This could be attributed to a lower

dielectric loss tangent of the quartz glass compared to alumina. The inductor on a glass substrate also demonstrates a higher self-resonant frequency which suggests that it has lower parasitic capacitances than those on alumina substrates. The lower parasitic capacitance, in the inductor on a quartz glass substrate, consequently, pushes its Q-factor slightly higher (flatter Q-factor plot) at high frequencies due to a higher magnetic energy stored in the inductor.

Table 5.3. Measured performance parameters of the medium inductors with different metals and substrate materials.

Type	Operating Frequency (f_0, GHz) @ $X_L = 50\,\Omega$	Inductance L (nH) @ f_0	Resistance $R\,(\Omega)$ @ f_0	Q-factor @ f_0	Self-resonant Frequency SRF (GHz)
Ni/ Alumina (1-loop)	6.8	1.2	2.3	22	17
Au/ Alumina (1-loop)	6.7	1.2	0.91	55	18
Ni/ Quartz (1-loop)	7.4	1.1	2.2	23	26
Ni/ Alumina (2-loop)	2.8	2.8	3.6	14	7.7
Au/ Alumina (2-loop)	2.9	2.7	1.6	32	7.9
Ni/ Quartz (2-loop)	3.0	2.6	3.4	15	11

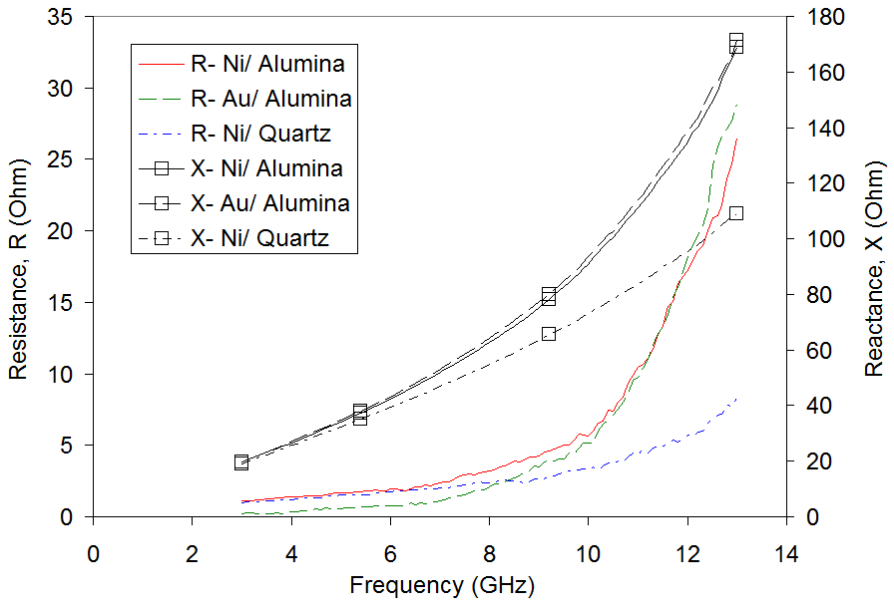

(a) Resistance and inductive reactance.

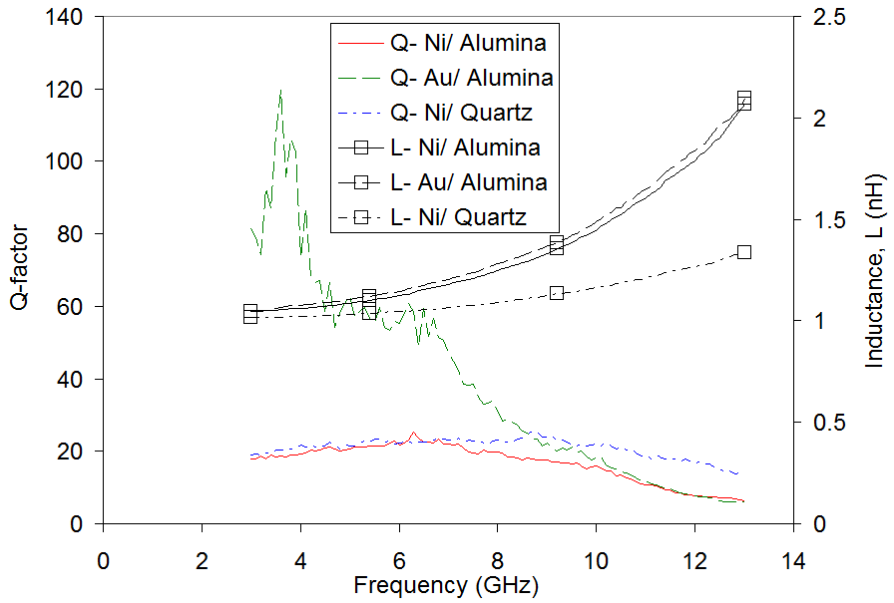

(b) Q-factor and inductance.

Figure 5.11. Measured inductor parameters of the medium 1-loop inductors from different samples.

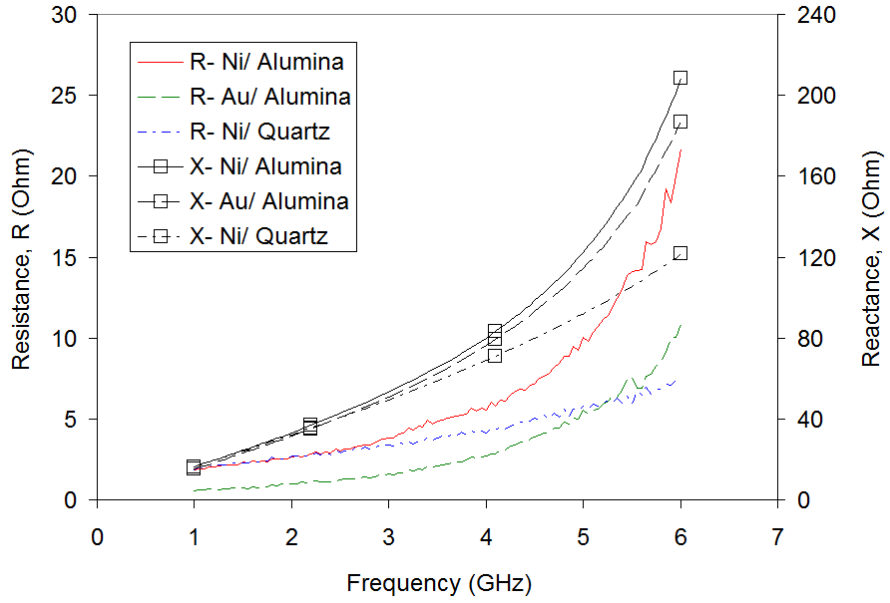

(a) Resistance and inductive reactance.

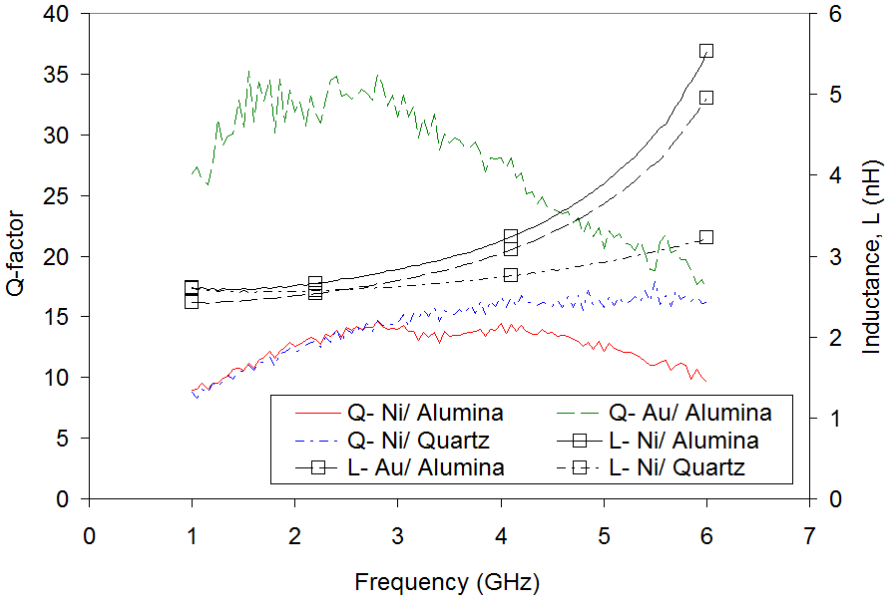

(b) Q-factor and inductance.

Figure 5.12. Measured inductor parameters of the medium 2-loop inductors from different samples.

5.3 Low-pass Filter Simulation and Measurement Results

The low-pass filter (LPF) designs presented in Chapter 4 were fabricated in nickel on both a quartz glass substrate (sample GL01) and an alumina substrate (sample 3814).

Figure 5.13 presents S_{11} plots of low-pass filter A on a quartz glass substrate (sample GL01) from both the measurement and HFSS simulation. Since the low-pass filter is a two-port network, the S_{11} plots indicate the matching of the filters at their ports in a 50-Ω characteristic impedance system. Figure 5.13 shows measured and simulated S_{11} magnitude of better than 10 dB at approximately 5 GHz. In terms of power delivered to the filter, this means more than 90% of power was transferred into the filter. At higher frequencies, the low-pass filter rejects most of the input signal, leading to small measured and simulated S_{11} magnitudes.

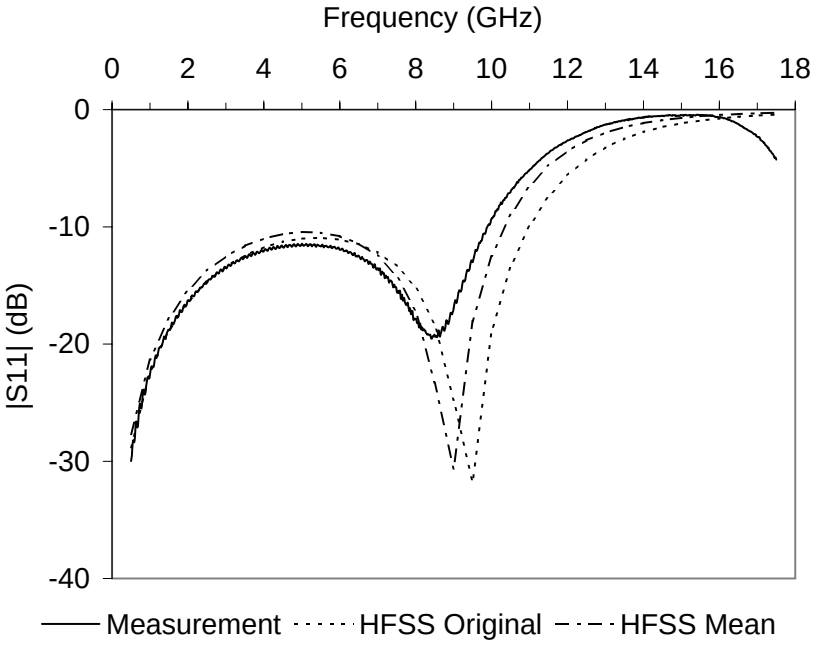

Figure 5.13. S_{11} response of low-pass filter A on a quartz glass substrate (sample GL01).

The S_{21} frequency response of low-pass filter A on sample GL01 from both the measurement and HFSS simulation is shown in Figure 5.14. The simulated S_{21} response shows three half-ripples in the pass-band, indicating a third order low-pass filter [63], with a ripple magnitude of 0.54 dB. Further, it also shows that the last ripple (f_{ripple}) occurs at about 11 GHz and the 3-dB frequency ($f_{3\text{dB}}$) at approximately 13 GHz. The frequency response decreases further as frequency increases into the stop-band of the filter. In comparison, the measured S_{21} plot also shows a third-order low-pass filter response with a pass-band ripple of 0.6 dB, a last-ripple frequency (f_{ripple}) of about 10 GHz, and a 3-dB frequency of approximately 12 GHz. Early in the stop-band, the measured and simulated S_{21} demonstrate approximately the same attenuation; however, at higher frequencies the measured S_{21} shows a steeper rejection slope than predicted during simulation. The measured S_{21} reaches a bottom point at approximately 16 GHz and bounces back toward zero, a behaviour not

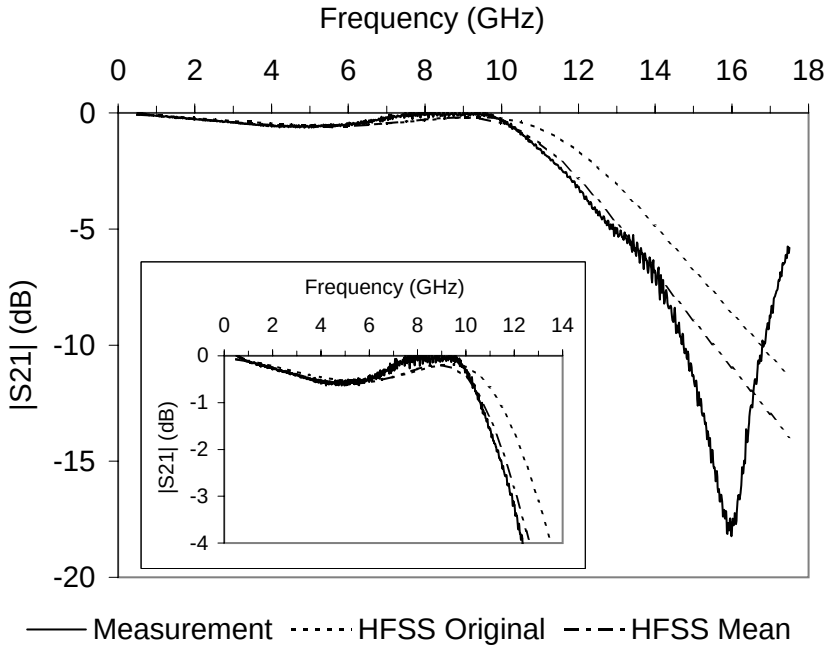

Figure 5.14. S_{21} response of low-pass filter A on a quartz glass substrate (sample GL01).

seen in the simulation result in the frequency span shown but expected to occur at a higher frequency. These differences in stop-band attenuation characteristics between the measurement and simulation can likely be attributed to secondary higher order effects, making the "π" equivalent circuit model of the low-pass filter less ideal. The differences can also be attributed to distributed RF effects due to the filter physical size that becomes more comparable to the signal wavelength at higher frequencies, contributing to the re-entrant behaviour.

The discrepancies in the S_{11} response, ripple amount, f_{ripple}, and $f_{3\text{dB}}$ between the measurement and simulation results can be attributed to the differences in the height of the filter structure and the air gap width between the final structure and the simulation model. This is because the structure height and gap width determine the capacitance in the filter structure. Inspection of the low-pass filter A structures revealed an average metal height of 212 μm and an average air gap width of 6.5 μm (aspect ratio of 33:1). These dimensions were 220 μm and 8.5 μm respectively in the simulation model. These measured mean values were fed back into HFSS software and the simulation was repeated. The HFSS simulation results using the mean values are also shown in both Figures 5.13 and 5.14. It can be seen that there is a better agreement in both S_{11} and S_{21} responses between the measurement and the simulation using the mean values. Further agreement could possibly be obtained with more comprehensive metal height and gap width measurements.

S_{11} plots of low-pass filter B on a quartz glass substrate (sample GL01) from both the measurement and HFSS simulation are shown in Figure 5.15. This figure shows measured and simulated S_{11} magnitudes of better than 11 dB at about 2.5 GHz. This is equivalent to 92% of excitation power being transmitted into the filter. In the higher frequency region, both the measured and simulated S_{11} almost vanish, indicating that very little input excitation signal gets transmitted into the filter in the stop band.

Figure 5.16 presents the S_{21} frequency responses of low-pass filter B on sample GL01 from both the measurement and HFSS simulation. The simulated S_{21} response shows three half-ripples in the pass-band, indicating a third-order low-pass response

with a ripple of 0.48 dB. It also shows a last-ripple frequency (f_{ripple}) of about 5.1 GHz, and a 3-dB frequency (f_{3dB}) of approximately 6.7 GHz. In comparison, the measured S_{21} plot shows a third-order low-pass response with a pass-band ripple of 0.6 dB, a last-ripple frequency (f_{ripple}) of about 4.7 GHz, and a 3-dB frequency of approximately 6.1 GHz. At higher frequencies the measured S_{21} shows a steeper rejection slope than the simulation, reaches a bottom point at approximately 11 GHz, and bounces back toward zero. The same S_{21} behaviour is not seen in the simulation in the frequency span shown but is expected to occur at a higher frequency. The differences in the stop-band attenuation characteristics can likely be attributed to secondary higher order and distributed RF effects, as was the case for low-pass filter A from the same sample.

Structural inspection of low-pass filter B revealed an average metal height of 203 μm and an average air gap width of 6.4 μm (aspect ratio of 32.1). These dimensions were 220 μm and 8.5 μm respectively in the simulation model. These

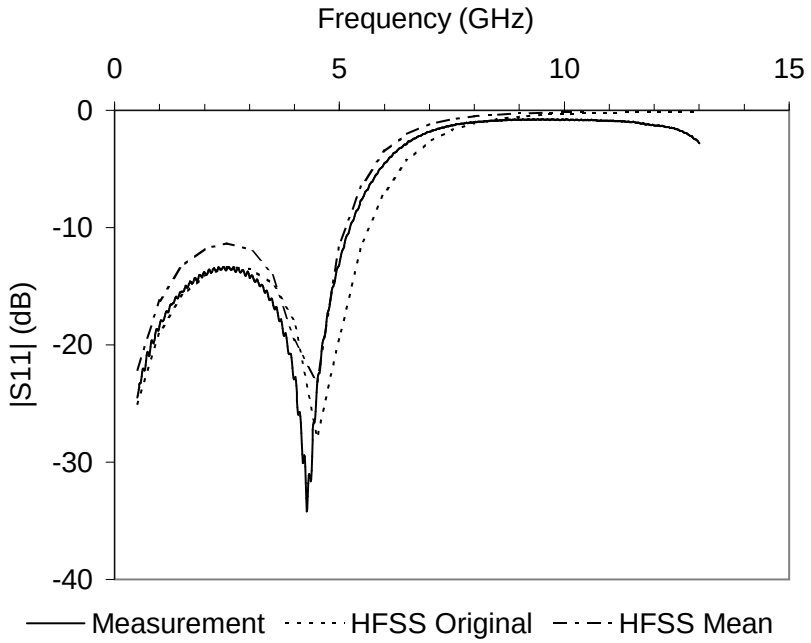

Figure 5.15. S_{11} response of low-pass filter B on a quartz glass substrate (sample GL01).

measured mean values were fed back into HFSS software and the simulation was repeated. The simulation results using the mean metal height and air gap width are also shown in both Figure 5.15 and 5.16. It can be seen that the S_{11} and S_{21} responses from the simulation using the mean values match the measurement responses better. This shows that differences in the S_{11} response, the ripple amount, f_{ripple}, and $f_{3\text{dB}}$ between measurement and simulation can be attributed to differences in the metal height and air gap width between the final structure and the simulation model.

Figure 5.17 presents S_{11} plots of low-pass filter A on an alumina substrate (sample 3814) from both the measurement and HFSS simulation. It shows measured and simulated S_{11} magnitude of better than 5 dB at about 5 GHz, indicating that more than 68% of power was transferred into the filter. In the higher frequency region, the simulated S_{11} magnitude vanishes while the measured S_{11} grows to about 10 dB before decreasing toward zero. This measured S_{11} behaviour concurs with the

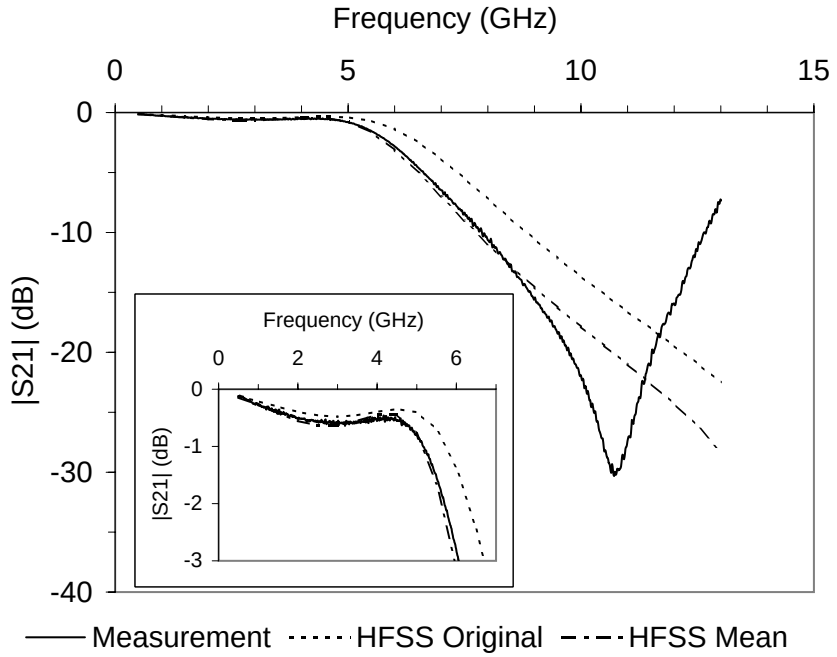

Figure 5.16. S_{21} response of low-pass filter B on a quartz glass substrate (sample GL01).

measured S_{21} response.

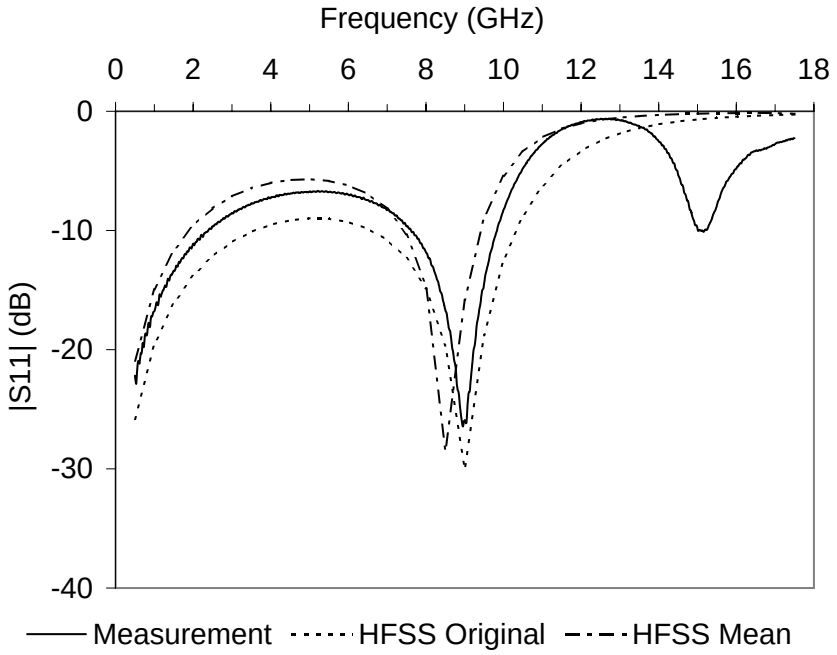

Figure 5.17. S_{11} response of low-pass filter A on an alumina substrate (sample 3814).

The S_{21} frequency responses of low-pass filter A from the same sample from both the measurement and HFSS simulation are shown in Figure 5.18. The simulated S_{21} response shows a third order low-pass response with a ripple magnitude of 0.8 dB, f_{ripple} of approximately 10.4 GHz and an $f_{3\text{dB}}$ of about 12 GHz. In comparison, the measured S_{21} response shows a third-order low-pass response with a pass-band ripple of 1.4 dB, an f_{ripple} of about 10 GHz, and an $f_{3\text{dB}}$ of approximately 11 GHz. In the stop-band, the measurement shows steeper rejection slope than the simulation and bottoms out at about 13 GHz. At higher frequencies, the measured S_{21} increases toward zero then decreases for a second time.

Metal height and air-gap width measurements of the filter structure revealed an average metal height of 285 μm and an average air gap width of 6 μm (aspect ratio of 48:1). Figure 5.17 and 5.18 show the simulation results using the mean metal

height and air gap width. The measurement for S_{11} is located somewhat in between the original simulation and the simulation using the mean values. The simulated S_{21} using the mean values looks somewhat similar to the measured one. Better metal height and air gap width measurements could give better agreements between measured and simulated S-parameters results.

S_{11} plots of low-pass filter B on an alumina substrate (sample 03814) from both the measurement and HFSS simulation are shown in Figure 5.19. This figure shows measured and simulated S_{11} magnitudes of better than 6 dB at approximately 2.5 GHz, indicating that 75% of excitation power is transmitted into the filter. In the higher frequency region, the magnitude of the simulated S_{11} almost vanishes while that of the measured S_{11} increases, indicating more excitation power is transferred into the filter.

The measured and simulated S_{21} frequency responses of low-pass filter B from the same sample are shown in Figure 5.20. The simulation result shows a third order

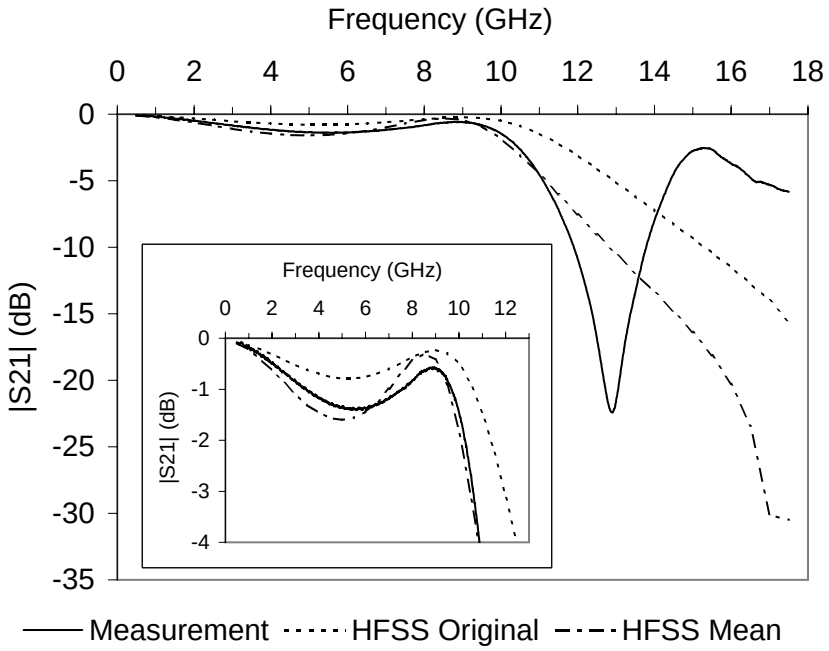

Figure 5.18. S_{21} response of low-pass filter A on an alumina substrate (sample 3814).

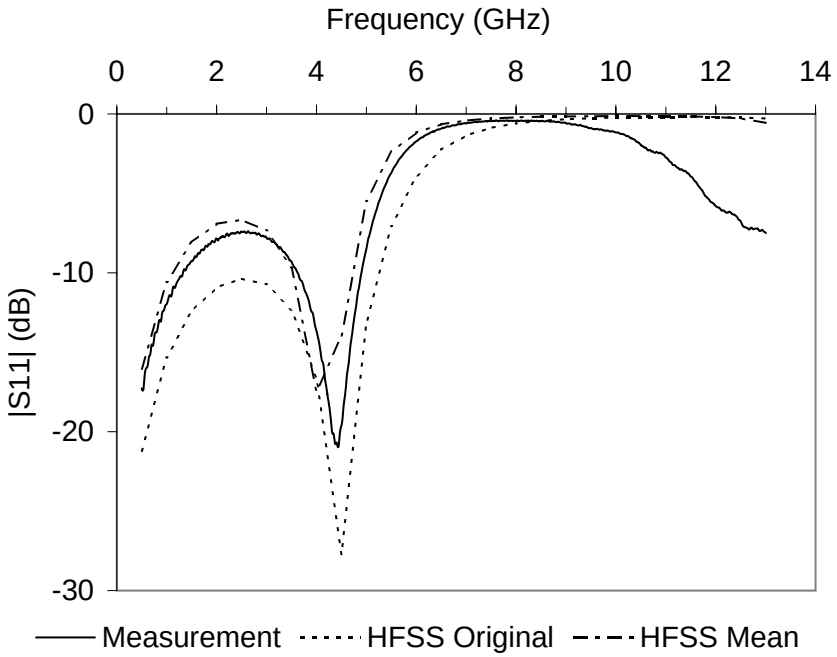

Figure 5.19. S_{11} response of low-pass filter B on an alumina substrate (sample 3814).

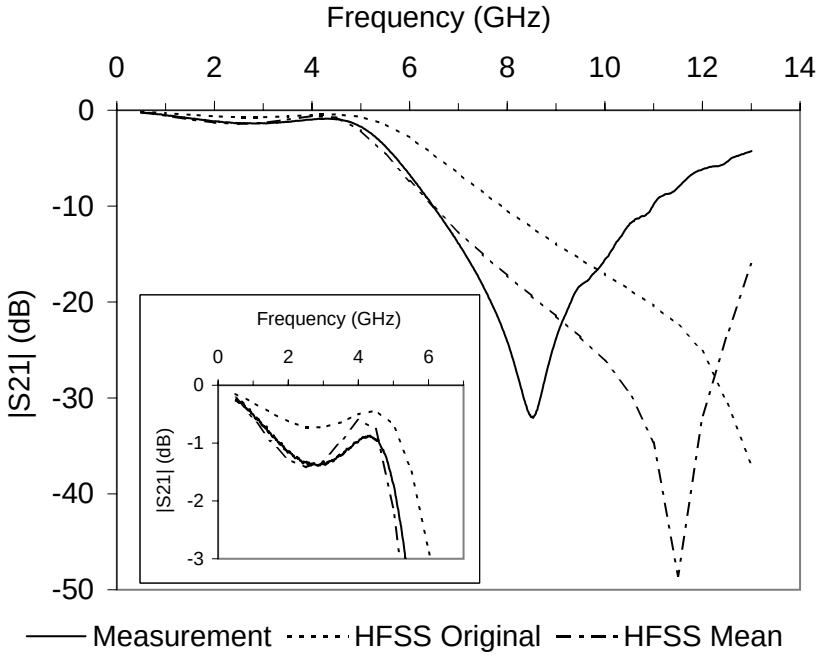

Figure 5.20. S_{21} response of low-pass filter B on an alumina substrate (sample 3814).

low-pass response with a ripple magnitude of 0.7 dB, an f_{ripple} of approximately 5 GHz and an $f_{3\text{dB}}$ of about 6.1 GHz. In the stop-band, the rejection slope becomes steeper at higher frequencies. In comparison, the measurement result shows a third-order low-pass response with a pass-band ripple of 1.4 dB, an f_{ripple} of about 4.7 GHz, and an $f_{3\text{dB}}$ of approximately 5.2 GHz. Similar to the previous filters, at higher frequencies the measurement shows higher attenuation than the simulation, bottoms out at about 8 GHz, and bounces back toward zero.

Metal height and air-gap width measurements of the filter structure revealed an average metal height of 270 μm and an average air gap width of 6 μm (aspect ratio of 45:1). HFSS simulation using the mean metal height and air gap width was performed and the results are shown in both Figures 5.19 and 5.20. Using the mean values, the simulated S_{21} exhibits a bottom point then increases back toward zero. Moreover, there is also better agreement between the simulation and the measurement in terms of the pass-band ripple, f_{ripple}, $f_{3\text{dB}}$, and the magnitude of S_{11}.

The use of quartz glass and alumina substrates, which have different values of relative permittivity (dielectric constant, ϵ_r) and dielectric loss tangent ($tan\,\delta$), allowed for observations of the substrate effects on the performances of the filters. These were done by comparing the measured S-parameters of filters from different samples. Figures 5.21 and 5.22 present the S-parameters of low-pass filter A and B respectively from both the quartz glass and alumina substrate.

In Figure 5.21, both the measured S_{21} responses of low-pass filter A on the alumina and quartz glass substrate show attenuation that increases rather abruptly in the higher frequency portion of the stop-band. Following the abrupt increase in the attenuation, the S_{21} responses eventually bottom out and increase back toward zero as frequency increases further. However, the bottom point on the S_{21} response for the filter on alumina occurs sooner than the one on quartz glass. These trends in the measured S_{21} responses can be attributed to an "electrically distributed" nature of the filter circuits where the phase of a voltage or current changes over the physical size of the circuit [54]. As the frequency increases, the corresponding wavelength (λ)

becomes smaller. Consequently, the physical size of the filters becomes on the order of the wavelength which, in turn, causes them to appear less "electrically lumped" and to start behaving like a distributed circuit, leading to a pass-band re-entrance. In simulations, this pass-band repetition occurred at frequencies higher than those in the figure. The difference in the frequency at which the bottom point on the S_{21} response occurs can be associated with the substrate material. The wavelength (λ) in a material is inversely proportional to the square root of the material's relative permeability (μ_r) and relative permittivity (ϵ_r).

For non-magnetic dielectric materials ($\mu_r = 1$), such as alumina and quartz glass, the proportions can be expressed as

$$\lambda_{dielectric} \propto \frac{1}{\sqrt{\epsilon_r}} \tag{5.1}$$

Therefore, for a given frequency, the wavelength in alumina will be smaller than that in quartz glass by a factor of $\sqrt{\epsilon_{r,quartz}/\epsilon_{r,alumina}}$ and so the physical size of the filter on alumina will be more comparable to its wavelength compared to that on quartz. Consequently the filter on alumina will behave like a distributed circuit more than the quartz glass counterpart.

As an illustration, on a quartz glass substrate, the width of LPF A (refer to Table 4.5) is approximately 10% of the wavelength at 12 GHz. On an alumina substrate, this width is about 17% of the wavelength at the same frequency. Assuming the low-pass filter circuits start to appear distributed when their physical size is 10% of the signal wavelength [85, 86], then the low-pass filter on alumina needs a smaller frequency to start behaving like a distributed transmission line.

Figure 5.21 also shows that low-pass filter A on the alumina substrate has a bigger pass-band ripple and a steeper rejection slope than that on the quartz glass substrate. These suggest that the inductive/capacitive impedances change when the same filter is fabricated on an alumina substrate. While the change in impedance can be caused by differences in the filter structures dimensions, they can also be attributed to the substrate material. This argument is supported by the simulated S_{21} responses of the two filters. The simulation models for the filter on alumina and

quartz glass substrate were identical except for the substrate type, yet variations in the pass-band ripple and rejection slope exist.

Changes in the inductive/capacitive impedances can also be explained using the distributed effects argument. Since the filter on alumina substrate appears more distributed than that on quartz glass substrate, the voltages and currents (thus impedances) in the filter circuit can vary in both magnitude and phase angle [54]. Because the wavelength in alumina is smaller than in quartz glass, there are more fractions of a wavelength in the filter. This leads to more variations in phase angle, thus impedance, across the dimensions of the filter on alumina substrate.

The measured S_{21} responses of low-pass filter B on an alumina and quartz glass substrate also share very similar trends with those of low-pass filter A in the higher frequency portion of the stop-band. However, as Figure 5.22 shows, filter B on both substrates reach their bottom point even sooner than filter A. This is likely because low-pass filter B has bigger dimensions than filter A. Consequently, low-pass filter B only needs a lower frequency than filter A to make its physical size equal to 10% of the wavelength, thus, starting to behave like a distributed transmission line. In the lower frequency portion of the stop-band and in the pass-band, the S_{21} responses in Figure 5.22 show that low-pass filter B on alumina substrate has a bigger ripple and a steeper rejection ratio than that on quartz glass. These trends are shared by low-pass filter A.

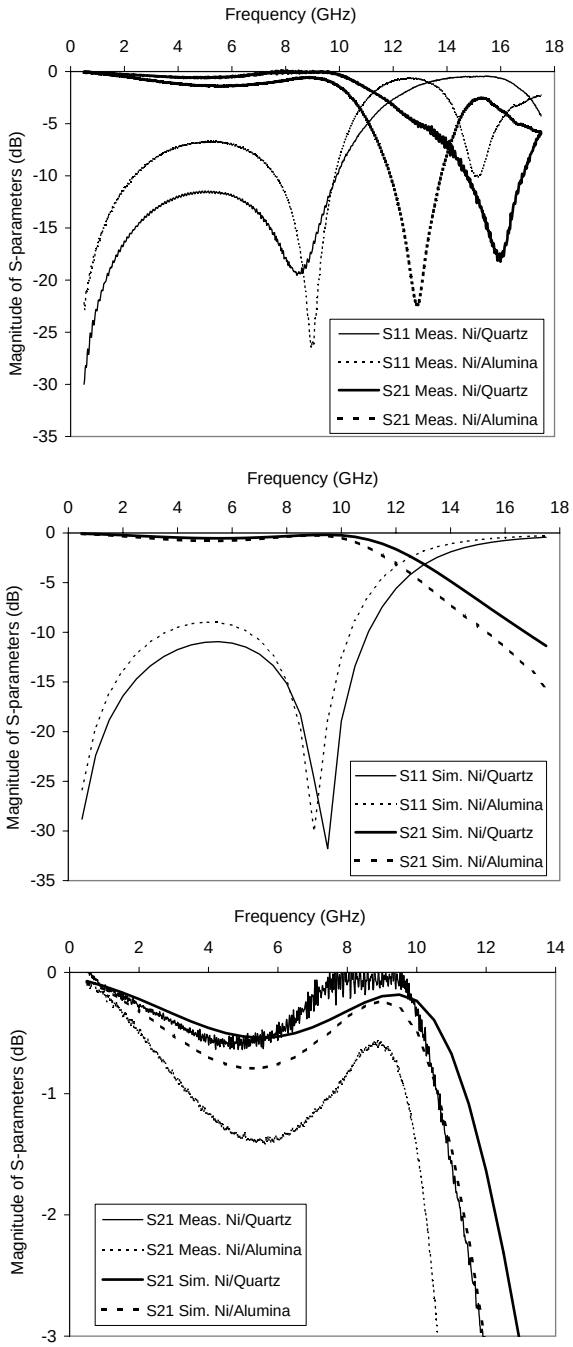

Figure 5.21. S-parameters of low-pass filter A on quartz glass and alumina (*top*: measurement, *middle*: simulation, *bottom*: magnified view of S_{21}).

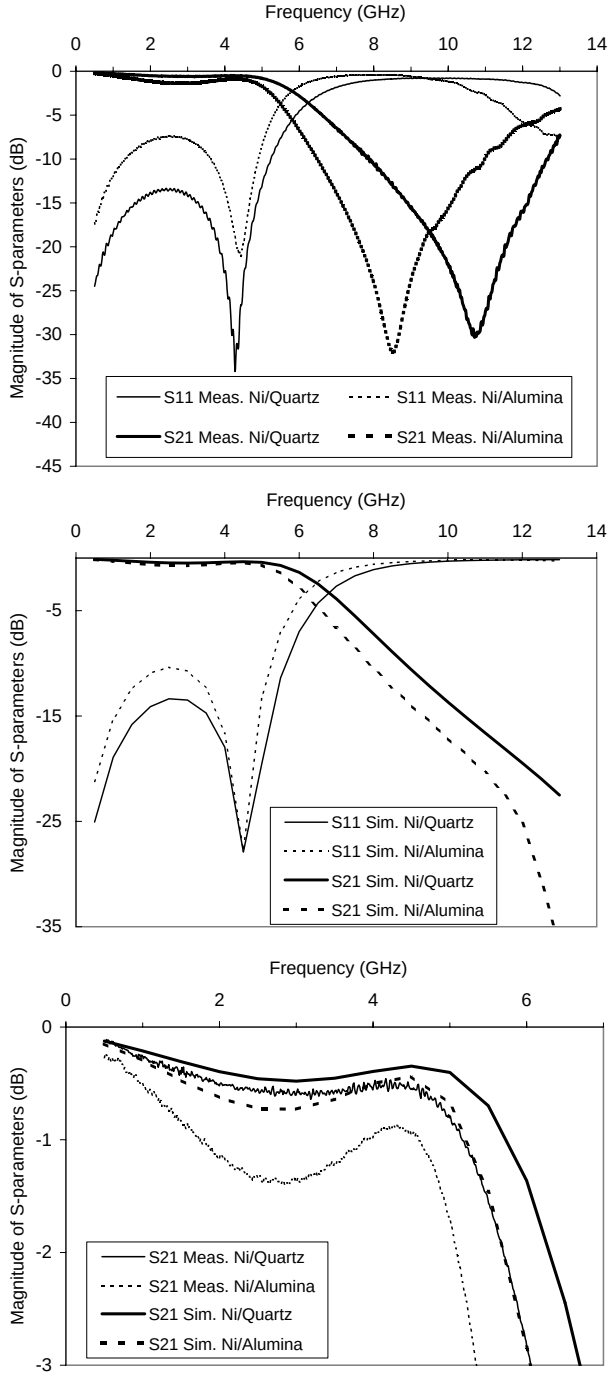

Figure 5.22. S-parameters of low-pass filter B on quartz glass and alumina (*top*: measurement, *middle*: simulation, *bottom*: magnified view of S_{21}).

5.4 Comparison to Representative Simulated Planar Distributed Low-pass Filters

In order to allow comparisons to distributed low-pass filters (LPFs), two planar distributed LPFs were designed and simulated using the ADS software. Both designs were based on common shunt- or series-connected $\frac{\lambda}{8}$ microstrip transmission-line segments, where λ is the signal wavelength. Further, each filter had a third-order Chebyshev response with comparable pass-band ripple and last-ripple frequency (f_{ripple}) to the measurement results of the lumped-element LPFs on a quartz glass substrate (sample GL01).

The distributed filters are shown in Figures 5.23 and 5.24 with their dimensions listed in Table 5.4. For comparison purposes, the lumped-element LPFs are also included in the figures. Both distributed filters are 18-μm thick in nickel on a quartz glass substrate. The material properties were the same as those in the lumped-element filter simulations using HFSS.

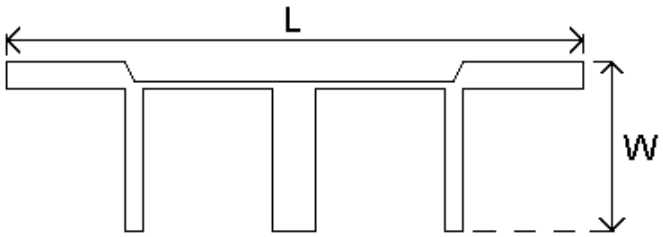

(a) Planar distributed.

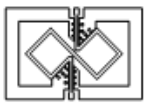

(b) Lumped-element.

Figure 5.23. Third-order low-pass filter design A.

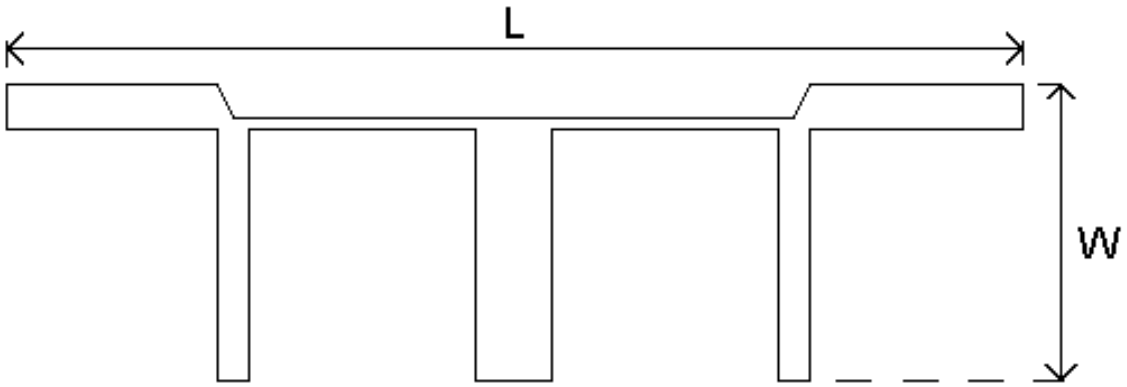

(a) Planar distributed.

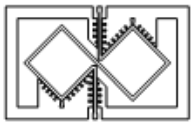

(b) Lumped-element.

Figure 5.24. Third-order low-pass filter design B.

Table 5.4. Dimensions and specifications of the distributed low-pass filters.

Planar Distributed Low-pass Filter	Design A	Design B
Ripple ammount [dB]	0.6	0.6
Last-ripple frequency, f_{ripple} [GHz]	10.3	4.7
Width, W [mm]	3.1	5.9
Length, L [mm]	8.6	19.4

Figure 5.25 shows S-parameters of the distributed-LPF design A obtained from simulations. The S_{21} response shows a 3^{rd}-order Chebyshev response with a bottom point occurring at about 22 GHz. This expected pass-band re-entrance is typical characteristic of a distributed low-pass filter.

Figure 5.26 shows the S-parameters of the simulated distributed-LPF A and the measured lumped-element LPF A from sample GL01. The lumped-element filter demonstrates a similar S_{11} response to its distributed counterparts. In terms of S_{21} response, this figure demonstrates that the lumped-element filter gives the expected 3^{rd}-order Chebyshev LPF response with comparable pass-band ripple, f_{ripple}, and $f_{3\text{dB}}$ to the distributed filter.

Figure 5.27 presents the S-parameters of the simulated distributed-LPF B and the measured lumped-element LPF B from sample GL01. Similar to the filter design A, the distributed filter also shows a 3^{rd}-order Chebyshev response with the typical pass-band re-entrance. This figure also demonstrates that the lumped-element LPF has comparable performance to the distributed filter.

Table 5.5 summarizes the dimensions of the planar distributed and lumped-element low-pass filters. The lumped-element filter dimensions are also shown in Chapter 4.4. Since the dimensions of the lumped-element filters do not depend on the signal wavelength, they can be made smaller. The lumped-element implementation leads to an area reduction of 89% and 95% for low-pass filter design A and design B respectively.

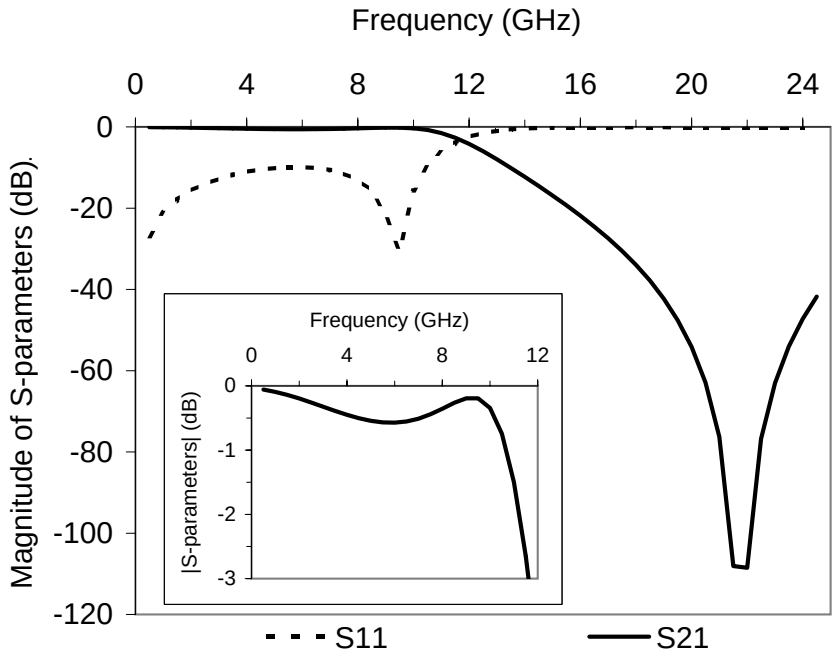

Figure 5.25. Magnitude of S-parameters of distributed low-pass filter design A.

Table 5.5. Size comparisons of distributed and lumped-element low-pass filters.

	Design A		Design B	
	Lumped-element	Distributed	Lumped-element	Distributed
Width, W [mm]	1.38	3.1	1.88	5.90
Length, L [mm]	2.08	8.6	3.10	19.4
Area Occupied [mm^2]	2.90	26.7	5.80	114.5

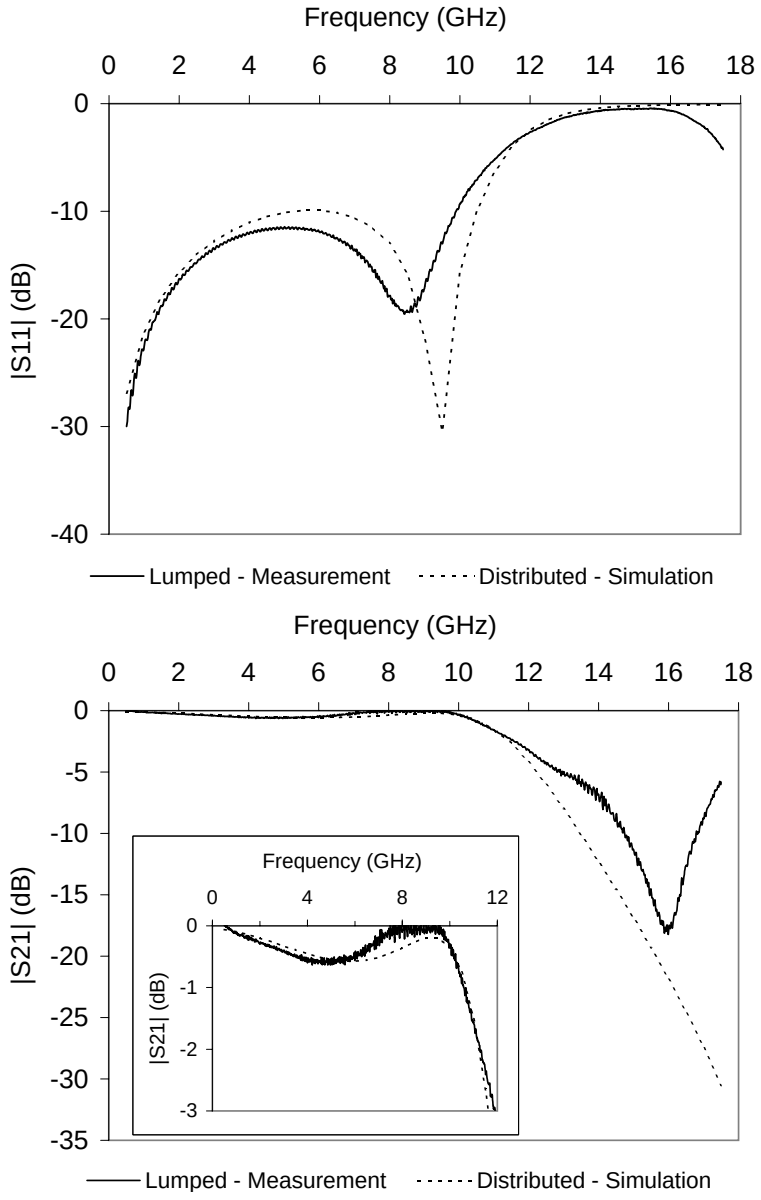

Figure 5.26. Magnitude of S-parameters of simulated distributed-LPF A and measured lumped-element LPF A from sample GL01.

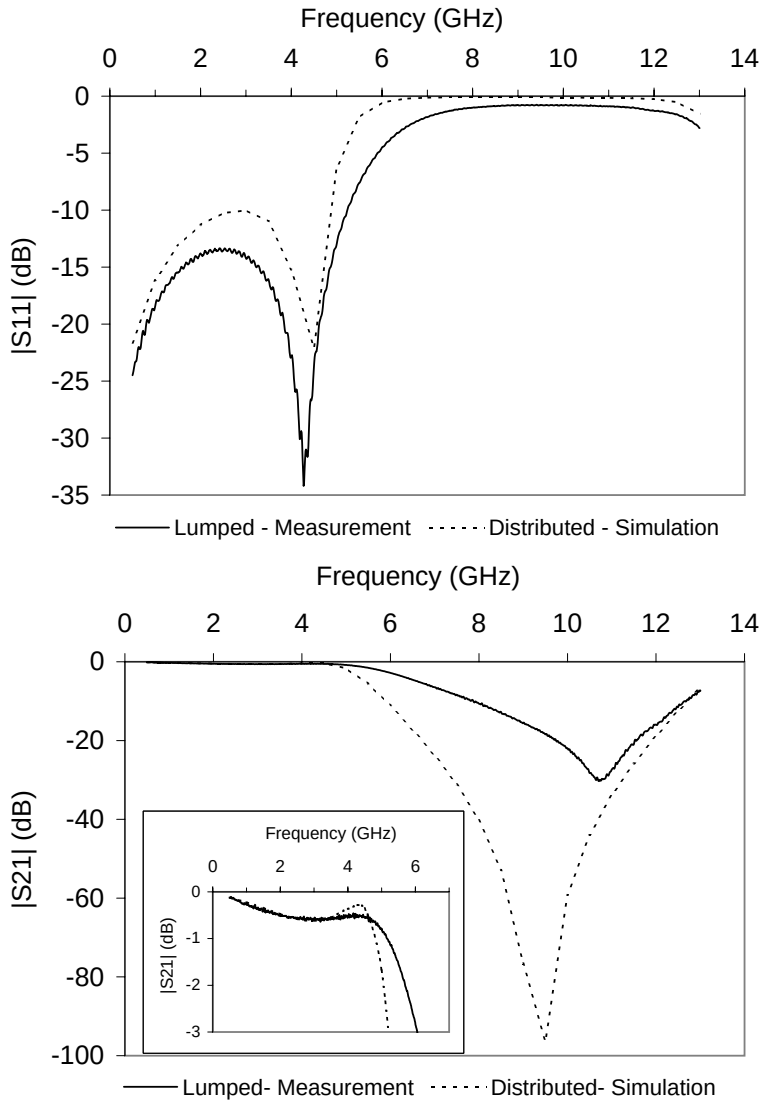

Figure 5.27. Magnitude of S-parameters of simulated distributed-LPF B and measured lumped-element LPF B from sample GL01.

6. CONCLUSIONS

6.1 Summary and Conlusions of Inductor Work

One of the research objectives was to develop inductors that were structurally compatible with capacitors similar to the pre-existing vertical RF MEMS capacitors in [18]. This was in a consideration that the two types of devices would be used as building blocks for lumped-element RF circuits such as filters. The compatibility issue constrained the inductor design to single-turn loops. The single-turn design allows simultaneous fabrication of both devices types and removes the requirement for an overpass which would be required in multi-turn inductors. Consequently, square 1-loop and 2-loop inductor designs, each having three sizes, were generated. Each 1-loop inductor consisted of a single-turn loop while the 2-loop inductor consisted of two single-turn loops in series.

The 1-loop and 2-loop inductors were fabricated in 70 μm nickel and gold on an alumina substrate and also nickel on a quartz glass substrate. At a 50-Ω inductive reactance point, the fabricated 1-loop inductors gave inductances of 0.4-3 nH with quality (Q) factor of 17- 55 and self-resonant frequencies exceeding 11 GHz. Also at the 50-Ω point, the fabricated 2-loop inductors provided inductances in the 0.8- 5.5 nH range with Q-factors of 11- 42 and self-resonant frequencies of 4- 22 GHz.

In general, the measured and simulated inductive reactances agreed reasonably well for all of the 1-loop and 2-loop inductors. In terms of the resistance values, rather significant discrepancies were observed between the measurement and simulation results of the 1-loop inductors. A possible cause was the high-frequency measurements that were more susceptible to parasitic effects, introducing measure-

ment errors. This was made worse by the small resistance values of the inductors that needed to be measured. Another possible cause was the indirect measurements of resistance values. The network analyzer measured voltage reflection coefficients which were then transformed to impedances. A slight change in the reflection coefficient could translate to a considerable amount in the resistance. The discrepancies could also be related to non-accurate definitions of material electrical properties during simulations such as metal permeability and conductivity, relative permittivity (i.e. dielectric constant), and loss tangent. For instance, simulations showed that a factor of 10 in the dielectric constant of alumina led to better agreements between simulation and measurement results of the medium 1-loop inductor on an alumina substrate. In the 2-loop inductor case, the measured and simulated resistances agreed reasonably well. Further, these agreements were better than in the 1-loop inductor case. The better agreements could be related to the lower frequency ranges in which the 2-loop inductors operated compared to those of the 1-loop inductors.

Benefiting from a higher electrical conductivity, the gold inductors demonstrated the lowest parasitic resistances, thus highest Q-factors. At high frequencies, due to a lower dielectric loss tangent, the inductors on a quartz glass substrate outperformed those on an alumina substrate. The inductors on a quartz glass also demonstrated the highest self-resonant frequency (SRF) due to lower parasitic capacitances. The quartz glass substrate also made the inductors appeared more "electrically lumped", allowing better RF performance at higher frequencies.

In conclusions, 1-loop and 2-loop inductors fabricated using deep X-ray lithography (DXRL), have been demonstrated. The structurally compatible design allowed them to be fabricated together with vertical RF MEMS capacitor elements. Through HFSS simulations, variations in the material electrical properties have been shown to affect the inductor performances. Accurate definitions of material properties in the simulations are therefore essential. A metal with high electrical conductivity and a substrate with low dielectric constant and loss tangent have been shown to enhance the performance of an inductor.

6.2 Summary and Conclusions of Low-pass Filter Work

Two lumped-element low-pass filters (LPF) were designed in 220-μm thick nickel on both quartz glass and alumina substrates and featured 8.5 μm capacitance air gaps. Both designs realized a third-order, 0.5-dB ripple Chebyshev response in a "π" equivalent ladder circuit with 3-dB frequencies (f_{3dB}) of 6.7 GHz and 12.9 GHz respectively.

The fabricated nickel-on-quartz filters had a 0.6-dB ripple with 3-dB frequencies (f_{3dB}) of 6.1 GHz and 11.9 GHz respectively. The filter $|S_{21}|$ responses hit a bottom point and rebounded, creating a "dip" which occurred at 11 GHz for the lower-f_{3dB} filter and 16 GHz for the higher-f_{3dB} filter. Upon closer inspections, the filter with a lower f_{3dB} had an average air gap of 6.4 μm and metal height of 203 μm (aspect ratio of 32:1). The filter with a higher f_{3dB} showed an average air gap and metal height of 6.5 μm and 212 μm respectively (aspect ratio of 33:1). When the filters were fabricated on an alumina substrate, they exhibited a 1.4-dB ripple with 3-dB frequencies (f_{3dB}) of 5.4 GHz and 10.6 GHz respectively. The "dip" in the $|S_{21}|$ response occurred at 8 GHz and 13 GHz for the lower-f_{3dB} and higher-f_{3dB} filter respectively. Structural examinations showed that the lower-f_{3dB} filter had an average air gap and metal height of 6 μm and 270 μm respectively (aspect ratio of 45:1). The higher-f_{3dB} filter displayed an average air gap and metal height of 6 μm and 285 μm respectively (aspect ratio of 48:1). Using these average values of air gap and metal height, the measured filter responses were better predicted during HFSS simulations.

In conclusions, lumped-element low-pass filters, fabricated using deep X-ray lithography (DXRL), have been demonstrated. These filters were approximately (1.4 x 2.1) mm^2 and (1.9 x 3.1) mm^2. The lumped-element implementations led to an area reduction of up to 95% on a quartz glass substrate versus a distributed-element approach. These lumped-element LPFs have successfully incorporated the vertical RF MEMS capacitor concept and structurally compatible loop inductor, showing that the two types of elements can be used as building blocks for lumped-

element filters.

Through HFSS simulations, variations in the air gap and metal height have been shown to affect the filter responses. Despite the lumped-element design, the fabricated filters exhibited a distributed-circuit characteristic at high frequencies. However, based on the measurement results, the occurrence of this characteristic shifted to a higher frequency when a substrate with a low relative permittivity, in this case quartz glass, was used.

6.3 Future Work

The following recommendations may be considered for continuation of the current study:

1. Electrical properties of the alumina, quartz glass, and electroplated nickel and gold, used in this study may be more comprehensively determined. The metal conductivity and relative permeability, relative permittivity, and loss tangent are particularly of interest. These properties determine how a simulation model will respond to a given set of inputs and more accurate material properties are important to obtain more representative simulation results.

2. The 2-loop inductor design in this study had an additional ground structure configured to facilitate testing. This ground structure may be de-embedded to improve even further the accuracy of the measurement results for the 2-loop inductors. One possible way to perform this can be found in [30, 32, 87].

3. The source (or sources) of the difference between simulated and measured resistance values in the 1-loop inductors should be more comprehensively determined. The fact that the difference was more significant in the 1-loop inductors suggested that there may be some loss mechanisms that were not properly considered in the simulations. This may serve as a starting point for further investigations.

4. The issue of air gap and metal height variations in the filter structures need

to be addressed. Filter performance was shown to be quite sensitive to these structural variations. A possible way to address the metal height variation is to use mechanical polishing.

5. The low-pass filters may be fabricated using high electrical conductivity metals such as gold and copper which will lower losses and improve the filter performance. However, this will require further development of suitable electroplating process to ensure good structural quality. The filters may also be built on a lower relative permittivity (i.e. dielectric constant) substrate. This will make the filters appear more electrically lumped, allowing them to operate at higher frequencies.

6. The lumped-element low-pass filter design concept may be extended into band-pass filter designs. Distributed band-pass filters typically require coupled resonators with $\frac{\lambda}{4}$-related impedance inverters, leading to a larger size than low-pass filters. With a comparable performance, a lumped-element band-pass filter design is expected to give an even more appreciable size reduction versus a distributed design.

REFERENCES

[1] J. L. Hilbert, "RF-MEMS for wireless communications," *IEEE Communications Magazine*, vol. 46, no. 8, pp. 68–74, 2008.

[2] J. Bouchaud, B. Knoblich, and H. Wicht, "Will RF MEMS live up their promise?," in *Proceedings of the 36th European Microwave Conference, EuMC 2006*, (Manchester, United Kingdom), pp. 1076–9.

[3] L. Lu, P. Bhattacharya, L. P. B. Katehi, and G. E. Ponchak, "X-band and K-band lumped wilkinson power dividers with a micromachined technology," in *2000 IEEE MTT-S International Microwave Symposium Digest*, vol. 1, pp. 287–90, 11-16 June 2000.

[4] F. Ellinger, R. Vogt, and W. Bachtold, "Compact reflective-type phase-shifter MMIC for C-band using a lumped-element coupler," *IEEE Transactions on Microwave Theory and Techniques*, vol. 49, no. 5, pp. 913–7, 2001.

[5] J.-M. Kim, S. Lee, J.-H. Park, J.-M. Kim, C.-W. Baek, Y. Kwon, and Y.-K. Kim, "MEMS-based compact dual-band bandpass filters with applications to wireless local area network," *Journal of Micromechanics and Microengineering*, vol. 16, no. 7, pp. 1135–42, 2006.

[6] E. Gono-Santosa, D. M. Klymyshyn, M. Börner, D. Haluzan, S. Achenbach, and J. Mohr, "High-aspect-ratio rf low-pass filter fabricated using deep x-ray lithography," in *8th International Workshop on High Aspect Ratio Micro-Structure Technology ,HARMST 2009*, (Saskatoon, Canada), pp. 199–200.

[7] S. Lucyszyn, "Review of radio frequency microelectromechanical systems technology," *IEE Proceedings-Science, Measurement and Technology*, vol. 151, no. 2, pp. 93–103, March 2004.

[8] M. J. Madou, *Fundamentals of Microfabrication: The Science of Miniaturization*. Boca Raton: CRC Press, 2nd ed., 2002.

[9] E. Becker, W. Ehrfeld, D. Munchmeyer, H. Betz, A. Heuberger, S. Pongratz, W. Glashauser, H. Michel, and R. von Siemens, "Production of separation-nozzle systems for uranium enrichment by a combination of X-ray lithography and galvanoplastics," *Naturwissenschaften*, vol. 69, no. 11, pp. 520– 3, 1982.

[10] E. Becker, W. Ehrfeld, P. Hagmann, A. Maner, and D. Munchmeyer, "Fabrication of microstructures with high aspect ratios and great structural heights by synchrotron radiation lithography, galvanoforming, and plastic moulding (liga process)," *Microelectronic Engineering*, vol. 4, no. 1, pp. 35– 56, 1986.

[11] W. Menz, J. Mohr, and O. Paul, *Microsystem Technology*. Weinheim: Wiley-VCH, 2001.

[12] S. Achenbach, D. Klymyshyn, D. Haluzan, T. Mappes, G. Wells, and J. Mohr, "Fabrication of RF MEMS variable capacitors by deep X-ray lithography and electroplating," *Microsystem Technologies*, vol. 13, no. 3- 4, pp. 343 – 7, 2007.

[13] F. Pantenburg, S. Achenbach, and J. Mohr, "Influence of developer temperature and resist material on the structure quality in deep x-ray lithography," *Journal of Vacuum Science and Technology B*, vol. 16, no. 6, pp. 3547– 51, 1998.

[14] F. Pantenburg, S. Achenbach, and J. Mohr, "Characterisation of defects in very high deep-etch x-ray lithography microstructures," *Microsystem Technologies*, vol. 4, no. 2, pp. 89– 93, 1998.

[15] S. Achenbach, *Optimization of the process conditions for the fabrication of microstructures by ultra deep X-ray lithography (UDXRL)*. PhD thesis, Forschungsentrum Karlsruhe, Karlsruhe, Germany, 2000.

[16] Z. Ma, D. Klymyshyn, S. Achenbach, and J. Mohr, "Microwave cavity resonators using hard x-ray lithography," *Microwave and Optical Technology Letters*, vol. 47, no. 4, pp. 353– 7, 2005.

[17] F. Pantenburg and J. Mohr, "Influence of secondary effects on the structure quality in deep x-ray lithography," *Nuclear Instruments and Methods in Physics Research, Section B*, vol. 97, no. 1- 4, pp. 551– 6, 1995.

[18] D. M. Klymyshyn, D. T. Haluzan, M. Börner, S. Achenbach, J. Mohr, and T. Mappes, "High aspect ratio vertical cantilever RF-MEMS variable capacitor," *IEEE Microwave and Wireless Components Letters*, vol. 17, no. 2, pp. 127–9, 2007.

[19] D. M. Klymyshyn, H. C. Jayatilaka, M. Borner, and J. Mohr, "High aspect-ratio coplanar waveguide wideband bandpass filter with compact unit cells," *IEEE Transactions on Microwave Theory and Techniques*, vol. 57, no. 11, pp. 2753–60, 2009.

[20] S. Achenbach, D. Klymyshyn, T. Mappes, A. Kachayev, V. Subramanian, G. Wells, and J. Mohr, "Submicron-scale surface acoustic wave resonators fabricated by high aspect ratio x-ray lithography and aluminum lift-off," *Microsystem Technologies*, vol. 14, no. 9- 11, pp. 1715– 19, 2008.

[21] A. Kachayev, D. Klymyshyn, S. Achenbach, and V. Saile, "High vertical aspect ratio liga microwave 3-db coupler," in *Proceedings International Conference on MEMS, NANO and Smart Systems (ICMENS 2003)*, (Banff, Canada), pp. 38–43, 2003.

[22] A. Reyes, S. El-Ghazaly, S. Dorn, M. Dydyk, D. Schroder, and H. Patterson, "Coplanar waveguides and microwave inductors on silicon substrates," *IEEE Transactions on Microwave Theory and Techniques*, vol. 43, no. 9, pp. 2016–22, 1995.

[23] H. Ronkainen, H. Kattelus, E. Tarvainen, T. Ruhisaari, M. Andersson, and P. Kuivalainen, "IC compatible planar inductors on silicon," *IEE Proceedings-Circuits, Devices and Systems*, vol. 144, no. 1, pp. 29–35, 1997.

[24] H. Jiang, Y. Wang, J. L. A. Yeh, and N. C. Tien, "On-chip spiral inductors suspended over deep copper-lined cavities," in *2000 IEEE MTT-S International Microwave Symposium Digest*, vol. 48, pp. 2415–23.

[25] G. W. Dahlmann, E. M. Yeatman, P. Young, I. D. Robertson, and S. Lucyszyn, "Fabrication, RF characteristics and mechanical stability of self-assembled 3D microwave inductors," in *Proceedings of 11th International Conference on Solid State Sensors and Actuators Transducers '01/Eurosensors XV*, vol. A97-98, (Munich, Germany), pp. 215–20.

[26] Y. S. Choi and J. B. Yoon, "Experimental analysis of the effect of metal thickness on the quality factor in integrated spiral inductors for rf ics," *IEEE Electron Device Letters*, vol. 25, no. 2, pp. 76–9, 2004.

[27] M. Rais-Zadeh and F. Ayazi, "Characterization of high-Q spiral inductors on thick insulator-on-silicon," *Journal of Micromechanics and Microengineering*, vol. 15, no. 11, pp. 2105–12, 2005.

[28] J. Sun and J. Miao, "High performance mems inductors fabricated on localised and planar thick SiO2 layer," *Electronics Letters*, vol. 41, no. 7, pp. 446–7, 2005.

[29] J. Lopez-Villegas, J. Samitier, C. Cane, P. Losantos, and J. Bausells, "Improvement of the quality factor of RF integrated inductors by layout optimization," *IEEE Transactions on Microwave Theory and Techniques*, vol. 48, no. 1, pp. 76–83, 2000.

[30] L. Li and D. Uttamchandani, "Monolithic RF MEMS inductor using silicon MEMS foundry process," *Micro & Nano Letters*, vol. 1, no. 1, pp. 5–8, 2006.

[31] W. Wu, F. Huang, Y. Li, S. Zhang, X. Han, Z. Li, Y. Hao, and Y. Wang, "RF inductors with suspended and copper coated thick crystalline silicon spirals for monolithic MEMS LC circuits," *IEEE Microwave and Wireless Components Letters*, vol. 15, no. 12, pp. 853–5, 2005.

[32] D. S. Park, Y. Jeong, J.-B. Lee, and S. Jung, "Chip-level integration of RF MEMS on-chip inductors using UV-LIGA technique," *Microsystem Technologies*, vol. 14, no. 9-11, pp. 1429–38, 2008.

[33] V. M. Lubecke, B. Barber, E. Chan, D. Lopez, M. E. Gross, and P. Gammel, "Self-assembling MEMS variable and fixed RF inductors," *IEEE Transactions on Microwave Theory and Techniques*, vol. 49, no. 11, pp. 2093–8, 2001.

[34] J. Zou, C. Liu, D. R. Trainor, J. Chen, J. E. Schutt-Aine, and P. L. Chapman, "Development of three-dimensional inductors using plastic deformation magnetic assembly (PDMA)," *IEEE Transactions on Microwave Theory and Techniques*, vol. 51, no. 4, pp. 1067–75, 2003.

[35] Y. J. Kim and M. G. Allen, "Surface micromachined solenoid inductors for high frequency applications," *IEEE Transactions on Components, Packaging & Manufacturing Technology, Part C (Manufacturing)*, vol. 21, no. 1, pp. 26–33, 1998.

[36] S. Kanamaluru, M. yi Li, and K. Chang, "Coplanar waveguide low-pass filter using open circuit stubs," *Microwave and Optical Technology Letters*, vol. 6, no. 12, pp. 715–7, 1993.

[37] K. C. Lee, H. T. Su, and W. S. H. Wong, "Realization of a wideband bandpass filter using cascaded lowpass to highpass filter," in *2008 International Conference On Microwave and Millimeter Wave Technology*, pp. 14–7, 2008.

[38] T. L. Willke and S. S. Gearhart, "Liga micromachined planar transmission lines and filters," *IEEE Transactions on Microwave Theory and Techniques*, vol. 45, no. 10, pp. 1681–8, 1997.

[39] D. Ahn, J.-S. Park, C.-S. Kim, J. Kim, Y. Qian, and T. Itoh, "A design of the low-pass filter using the novel microstrip defected ground structure," *IEEE Transactions on Microwave Theory and Techniques*, vol. 49, no. 1, pp. 86–93, 2001.

[40] J.-S. Lim, C.-S. Kim, D. Ahn, Y.-C. Jeong, and S. Nam, "Design of low-pass filters using defected ground structure," *IEEE Transactions on Microwave Theory and Techniques*, vol. 53, no. 8, pp. 2539–45, 2005.

[41] Y. Qi and X. Liu, "Harmonic-suppressed elliptic-function low-pass filter using defected ground structure," in *IEEE 2007 International Symposium on Microwave, Antenna, Propagation and EMC Technologies for Wireless Communications*, pp. 419–22, 2007.

[42] A. Boutejdar, A. Omar, A. Batmanov, and E. Burte, "New low-pass filter design using compensated microstrip capacitor and coupled meander defected ground structure (DGS)," in *German Microwave Conference, GeMIC 2009*, (Munich, Germany), p. 4.

[43] J.-M. Kim, K. Chu, S. Lee, D.-K. Lee, Y. Kim, J.-M. Kim, C.-W. Baek, Y. Kwon, and Y.-K. Kim, "Novel compact low-loss millimeter-wave filters using micromachined overlay and inverted overlay coplanar waveguide transmission lines with defected ground structures," *Journal of Micromechanics and Microengineering*, vol. 16, no. 10, pp. 2183–91, 2006.

[44] N. M. Nguyen and R. G. Meyer, "Si IC-compatible inductors and LC passive filters," *IEEE Journal of Solid-State Circuits*, vol. 25, no. 4, pp. 1028–31, 1990.

[45] J. Fang, Z. W. Liu, Z. M. Chen, L. T. Liu, and Z. J. Li, "Realization of an integrated planar LC low-pass filter with modified surface micromachining technology," in *2005 IEEE Conference on Electron Devices and Solid-State Circuits, EDSSC*, (Howloon, Hong kong), pp. 729–31, 2005.

[46] J. D. Kraus, *Electromagnetic*. New York: McGraw-Hill, 4th ed., 1992.

[47] N. Ida, *Engineering Electromagnetics*. New York: Springer, 2000.

[48] W. H. Hayt and J. A. Buck, *Engineering Electromagnetic*. Boston: McGraw-Hill, 6th ed., 2001.

[49] C. P. Yue and S. S. Wong, "Physical modeling of spiral inductors on silicon," *IEEE transactions on electron devices*, vol. 47, no. 3, pp. 560–8, 2000.

[50] V. D. Desnica, L. D. Zivanov, O. S. Aleksic, M. D. Lukovic, and M. D. Nimrihter, "Comparative characteristics of thick-film integrated LC filters," *IEEE Transactions on Instrumentation and Measurement*, vol. 51, no. 4, pp. 570–6, 2002.

[51] F. W. Grover, *Inductance Calculations*. New York: D. Van Nostrand, 1946.

[52] H. M. Greenhouse, "Design of planar rectangular microelectronic inductors," *IEEE Transactions on Parts, Hybrids and Packaging*, vol. PHP-10, no. 2, pp. 101–9, 1974.

[53] J. C. Slater and N. H. Frank, *Electromagnetism*. New York: Dover Publications, 1969.

[54] D. M. Pozar, *Microwave Engineering*. New York: Wiley, 2nd ed., 1998.

[55] U. S. Inan and A. S. Inan, *Electromagnetic Waves*. Champaign, IL: Prentice Hall, 2000.

[56] X. Huo, P. C. H. Chan, K. J. Chen, and H. C. Luong, "A physical model for on-chip spiral inductors with accurate substrate modeling," *IEEE Transactions on Electron Devices*, vol. 53, no. 12, pp. 2942–9, 2006.

[57] X. Yu, "Modeling and analysis of thick suspended deep x-ray liga inductors on CMOS/BiCMOS substrate," Master's thesis, University of Saskatchewan, Saskatoon, Canada, 2006.

[58] G. M. Rebeiz, *RF MEMS: Theory, Design, and Technology*. Hoboken, NJ: John Wiley and Sons, 2003.

[59] C. P. Yue and S. S. Wong, "On-chip spiral inductors with patterned ground shields for Si-based RF ICs," *IEEE Journal of Solid-State Circuits*, vol. 33, no. 5, pp. 743–52, 1998.

[60] K. L. Su, *Analog Filters*. London; New York: Chapman & Hall, 1996.

[61] L. J. Geis, *Transform Analysis and Filters*. Englewood Cliffs, NJ: Prentice Hall, 1989.

[62] J. B. Hagen, *Radio-Frequency Electronics: Circuits and Applications*. Cambridge, UK; New York: Cambridge University Press, 1996.

[63] R. Schaumann and M. E. V. Valkenburg, *Design of Analog Filters*. New York: Oxford University Press, 2001.

[64] J.-S. Hong and M. J. Lancaster, *Microstrip Filters for RF/Microwave Applications*. New York: John Wiley & Sons, 2001.

[65] Ansoft Corporation. HFSS v10 documentation. [ONLINE]. Available: http://www.ansoft.com/ots/display_info.cfm?id=2929.

[66] D. Haluzan, "Microwave LIGA-MEMS variable capacitors," Master's thesis, University of Saskatchewan, Saskatoon, Canada, 2004.

[67] A. Kachayev, "Liga-micromachined tight microwave couplers," Master's thesis, University of Saskatchewan, Saskatoon, Canada, 2003.

[68] Ansoft Corporation. HFSS port series: Coplanar waveguide. [ONLINE]. Available: http://www.ansoft.com/ots/display_info.cfm?id=1163.

[69] S. Lucyszyn. (2008, June). Microwave characterization of nickel. *PIERS Online* [Online]. 4(6), pp. 686-90. Available: http://dx.doi.org/10.2529/PIERS080119215655.

[70] R. M. Bozorth, *Ferromagnetism*. New York: Van Nostrand, 1951.

[71] W. Arkadiew, "Über die absorption elektromagnetischer wellen an zwei parallelen drähten (the absorption of electromagnetic waves on two parallel wires)," *Annalen der Physik*, vol. 58, no. 2, pp. 105–38, 1919.

[72] J. B. Hoag and N. Gottleib, "The inner, initial permeability of iron and nickel from 98 to 410 megacycles," *Phys.Rev.*, vol. 55, no. 4, p. 410, 1939.

[73] K. F. Lindman, "Ueber die magnetische permeabilitaet des nickels fuer hertzsche schwingungen," *Zeitschrift fuer Technische Physik*, vol. 19, no. 10, pp. 323–324, 1938.

[74] D. Mohring, "Permeability of magnetic materials at h.f," *Hochfrequenztechnik und Elektroakustik*, vol. 53, pp. 196–9, 1939.

[75] J. L. Glathart, "Inner, initial, magnetic permeability of iron and nickel at ultra-high radio frequencies," *Physical review*, vol. 55, p. 833, 1939.

[76] G. Potapenko and R. Sänger, "Magnetische permeabilität der ferromagnetischen metalle bei sehr hoher frequenz," vol. 21, no. 46, pp. 818–9, 1933.

[77] I. Simon, "Magnetic permeability of nickel in the region of centimeter waves," *Nature*, vol. 157, p. 735, 1946.

[78] G. F. Hodsman, G. Eichholz, and R. Millership, "Magnetic dispersion at microwave frequencies," *Proceedings of the Physical Society.Section B*, vol. 62, pp. 377–90, 1949.

[79] S. Graham, J. Kelley, N. Yang, and T. Borca-Tasciuc, "The role of microstructure in the electrical and thermal conductivity of ni-alloys for liga microsystems," *Microsystem Technologies*, vol. 10, no. 6-7, pp. 510–16, 2004.

[80] J. R. Davis, *Metals Handbook: Desk Edition*. Materials Park, Ohio: ASM International, 2nd ed., 1998.

[81] W. H. Safranek, *The Properties of Electrodeposited Metals and Alloys: A Handbook*. Florida: American Electroplaters and Surface Finishers Society, 2nd ed., 1986.

[82] M. A. Meitl, X. Feng, J. Dong, E. Menard, P. M. Ferreira, Y. Huang, and J. A. Rogers, "Stress focusing for controlled fracture in microelectromechanical systems," *Applied Physics Letters*, vol. 90, no. 8, pp. 83110–1, 2007.

[83] Agilent Technologies. User's Guide Agilent Technologies 8719ES/20ES/22ES Network Analyzers. [ONLINE].
Available: http://cp.literature.agilent.com/litweb/pdf/08720-90392.pdf.

[84] Cascade Microtech, Inc. On-Wafer Vector Network Analyzer Calibration and Measurements. [ONLINE]. Available: http://www.cmicro.com/file/on-wafer-vector-network-analyzer-calibration-and-measurements.

[85] Y. Konishi, *Microwave Integrated Circuits*. New York: M. Dekker, 1991.

[86] D. Peroulis, S. Pacheco, K. Sarabandi, and L. P. B. Katehi, "Tunable lumped components with applications to reconfigurable MEMS filters," in *2001 IEEE MTT-S International Microwave Symposium Digest*, vol. 1, pp. 341–4.

[87] J. Zeng, A. J. Pang, C. H. Wang, and A. J. Sangster, "Flip chip assembled MEMS inductors," *Electronics Letters*, vol. 41, no. 8, pp. 480–1, 2005.

APPENDIX A. Denominator Polynomials and Element Values for Normalized Chebyshev Low-pass Filters

Table A.1. Denominator polynomials of normalized low-pass Chebyshev filters [60]. Pass-band ripple, $\alpha_p = 0.5$ dB, $\epsilon = 0.349$, n is the filter order.

n	Denominator Polynomials
1	$s + 2.8628$
2	$s^2 + 1.4256s + 1.5162$
3	$s^3 + 1.2529s^2 + 1.5349s + 0.7157$
4	$s^4 + 1.1974s^3 + 1.7169s^2 + 1.0255s + 0.3791$
5	$s^5 + 1.1725s^4 + 1.9374s^3 + 1.3096s^2 + 0.7525s + 0.1789$
6	$s^6 + 1.1592s^5 + 2.1718s^4 + 1.5898s^3 + 1.1719s^2 + 0.4324s + 0.0948$
7	$s^7 + 1.1512s^6 + 2.4127s^5 + 1.8694s^4 + 1.6479s^3 + 0.7557s^2 + 0.2821s + 0.0447$

Table A.2. Element values for normalized Chebyshev low-pass filters [61]. Pass-band ripple, $\alpha_p = 0.5$ dB, $\epsilon = 0.349$, n is the filter order.

n	$\frac{R_2}{R_s}$	C_1	L_2	C_3	L_4	C_5	L_6	C_7	L_8
2	0.5	1.5132	0.6538						
3	1.0	1.5963	1.0967	1.5963					
4	0.5	1.8158	1.1328	2.4481	0.7732				
5	1.0	1.7058	1.2296	2.5408	1.2296	1.7058			
6	0.5	1.8786	1.1884	2.7589	1.2403	2.5976	0.7976		
7	1.0	1.7373	1.2582	2.6383	1.3443	2.6383	1.2582	1.7373	
8	0.5	1.9012	1.2053	2.8152	1.2864	2.8479	1.2628	2.6310	0.8063
n	$\frac{R_s}{R_2}$	L_1	C_2	L_3	C_4	L_5	C_6	L_7	C_8

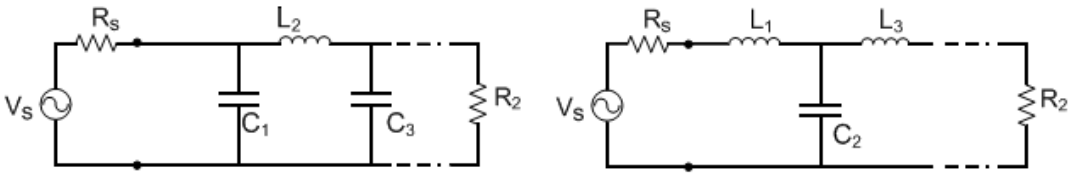

(a) Minimum inductor.

(b) Minimum capacitor.

Figure A.1. Low-pass filter realizations.

APPENDIX B. Complete Inductor Simulation and Measurement Results

B.1 Summary of Inductor Performance

Simulation and measurement results for nickel inductors on an alumina substrate and comparisons between different samples using medium-sized 1-loop and 2-loop inductor were already presented in Chapter 5. The results for the remaining inductor samples will now be presented.

Table B.1 and B.2 summarize the performance parameters of the 1-loop and 2-loop gold inductors on an alumina substrate respectively. Table B.3 and B.4 list the performance parameters of the 1-loop and 2-loop nickel inductors on a quartz glass substrate. Plots of the measurement data for these four inductors can be found in the sections to follow.

As an effort to facilitate comparisons, Table B.5 gives the performance parameters of the small inductors with different metals and substrates while Table B.6 presents those for the large inductors. The graphs of S-parameters for these comparisons can be found in section B.4.

Table B.1. Performance parameters of the 1-loop gold inductors on an alumina substrate (Meas.= measurement values, Sim.= simulation values).

Type		Operating Frequency (f_0, GHz) @ $X_L = 50\,\Omega$	Inductance L (nH) @ f_0	Resistance $R\,(\Omega)$ @ f_0	Q-factor @ f_0	Self-resonant Frequency SRF (GHz)
Small	Meas.	18	0.44	1.8	28	> 26.5
	Sim.	16	0.51	0.66	75	33
Medium	Meas.	6.7	1.2	0.91	55.0	18
	Sim.	6.6	1.2	0.49	102	17
Large	Meas.	2.7	3.0	1.1	45	11
	Sim.	3.6	2.2	0.54	93	10

Table B.2. Performance parameters of the 2-loop gold inductors on an alumina substrate (Meas.= measurement values, Sim.= simulation values).

Type		Operating Frequency (f_0, GHz) @ $X_L = 50\,\Omega$	Inductance L (nH) @ f_0	Resistance $R\,(\Omega)$ @ f_0	Q-factor @ f_0	Self-resonant Frequency SRF (GHz)
Small	Meas.	9.7	0.82	1.2	42	22
	Sim.	9.2	0.88	0.86	59	20
Medium	Meas.	2.9	2.7	1.6	32	7.9
	Sim.	3.0	2.6	0.90	56	7.1
Large	Meas.	1.5	5.3	1.6	31	4.4
	Sim.	1.6	5.1	0.92	54	4.1

Table B.3. Performance parameters of the 1-loop nickel inductors on a quartz glass substrate (Meas.= measurement values, Sim.= simulation values).

Type		Operating Frequency (f_0, GHz) @ $X_L = 50\,\Omega$	Inductance L (nH) @ f_0	Resistance $R\,(\Omega)$ @ f_0	Q-factor @ f_0	Self-resonant Frequency SRF (GHz)
Small	Meas.	20	0.40	1.1	48	> 26.5
	Sim.	17	0.47	1.0	49	44
Medium	Meas.	7.4	1.1	2.2	23	26
	Sim.	7.0	1.1	1.1	46	23
Large	Meas.	3.3	2.4	2.5	20	15
	Sim.	3.8	2.1	1.8	27	14

Table B.4. Performance parameters of the 2-loop nickel inductors on a quartz glass substrate (Meas.= measurement values, Sim.= simulation values).

Type		Operating Frequency (f_0, GHz) @ $X_L = 50\,\Omega$	Inductance L (nH) @ f_0	Resistance $R\,(\Omega)$ @ f_0	Q-factor @ f_0	Self-resonant Frequency SRF (GHz)
Small	Meas.	11	0.76	2.2	23	> 26.5
	Sim.	9.8	0.82	1.2	42	27
Medium	Meas.	3.0	2.6	3.4	15	11
	Sim.	3.1	2.5	3.1	16	9.6
Large	Meas.	1.5	5.3	4.1	12	6.4
	Sim.	1.6	5.1	4.1	12	5.4

Table B.5. Measured performance parameters of the small inductors with different metals and substrate materials.

Type	Operating Frequency (f_0, GHz) @ $X_L = 50\,\Omega$	Inductance L (nH) @ f_0	Resistance $R\,(\Omega)$ @ f_0	Q-factor @ f_0	Self-resonant Frequency SRF (GHz)
Ni/ Alumina (1-loop)	18	0.44	1.5	34	> 26.5
Au/ Alumina (1-loop)	18	0.44	1.8	28	> 26.5
Ni/ Quartz (1-loop)	20	0.40	1.1	48	> 26.5
Ni/ Alumina (2-loop)	9.5	0.84	2.5	20	22
Au/ Alumina (2-loop)	9.7	0.82	1.2	42	22
Ni/ Quartz (2-loop)	11	0.76	2.2	23	> 26.5

Table B.6. Measured performance parameters of the large inductors with different metals and substrate materials.

Type	Operating Frequency (f_0, GHz) @ $X_L = 50\,\Omega$	Inductance L (nH) @ f_0	Resistance $R\,(\Omega)$ @ f_0	Q-factor @ f_0	Self-resonant Frequency SRF (GHz)
Ni/ Alumina (1-loop)	3.2	2.5	2.9	17	11
Au/ Alumina (1-loop)	2.7	3.0	1.1	45	11
Ni/ Quartz (1-loop)	3.3	2.4	2.5	20	15
Ni/ Alumina (2-loop)	1.5	5.5	4.4	11	4.4
Au/ Alumina (2-loop)	1.5	5.3	1.6	31	4.4
Ni/ Quartz (2-loop)	1.5	5.3	4.1	12	6.4

B.2 Inductor Parameters of 1-loop and 2-loop Inductors (Gold on Alumina)

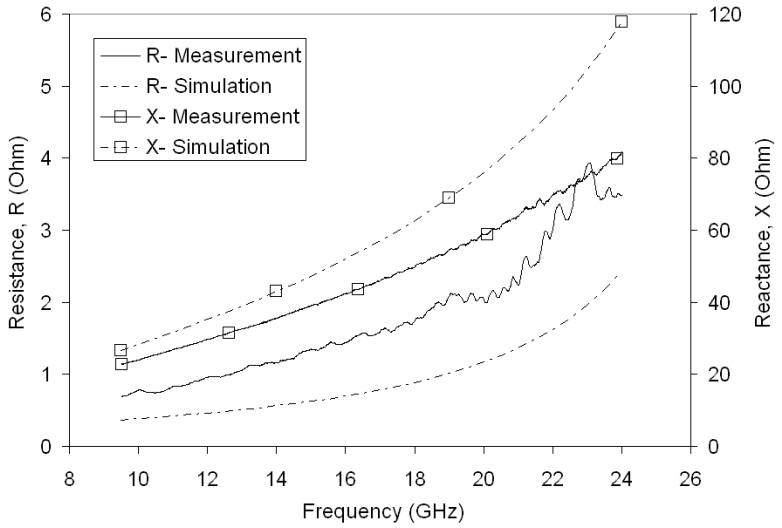

(a) Resistance and inductive reactance.

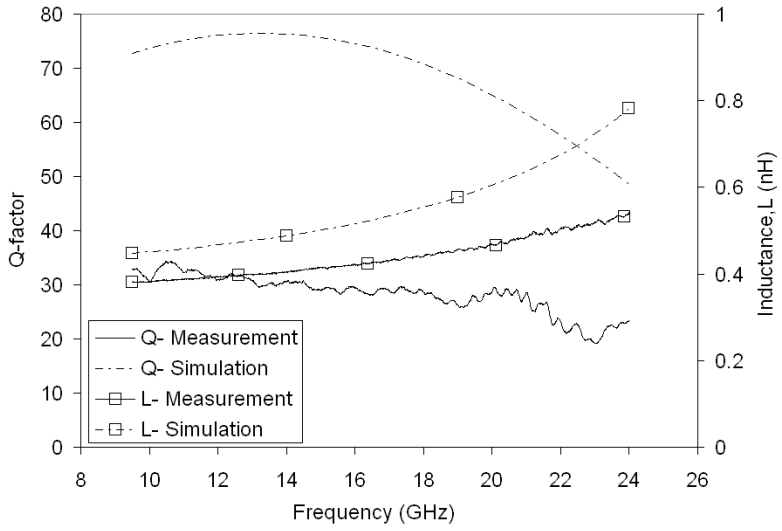

(b) Q-factor and inductance.

Figure B.1. Inductor parameters of small 1-loop inductor (gold on alumina).

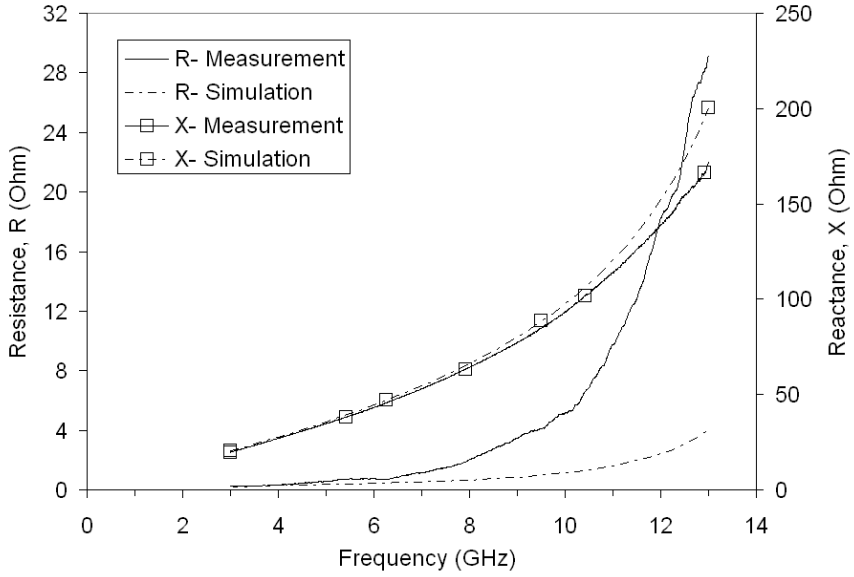

(a) Resistance and inductive reactance.

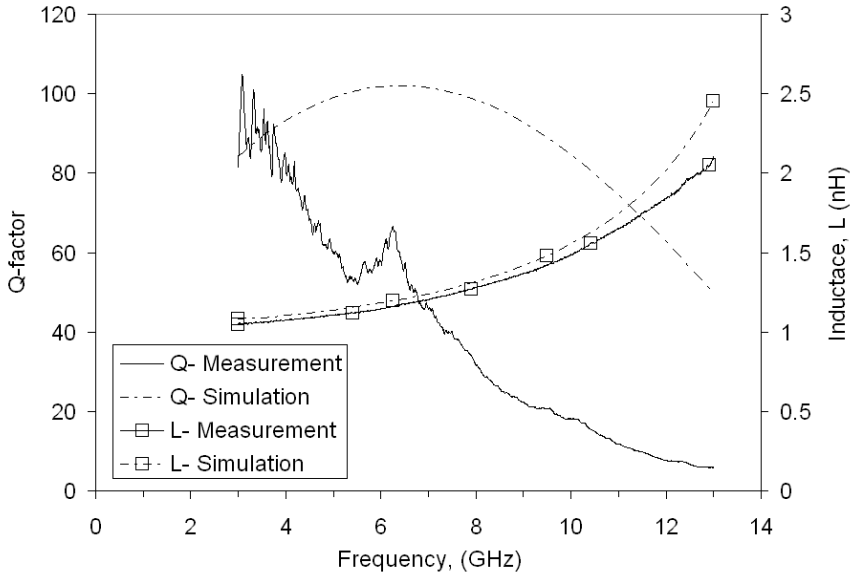

(b) Q-factor and inductance.

Figure B.2. Inductor parameters of medium 1-loop inductor (gold on alumina).

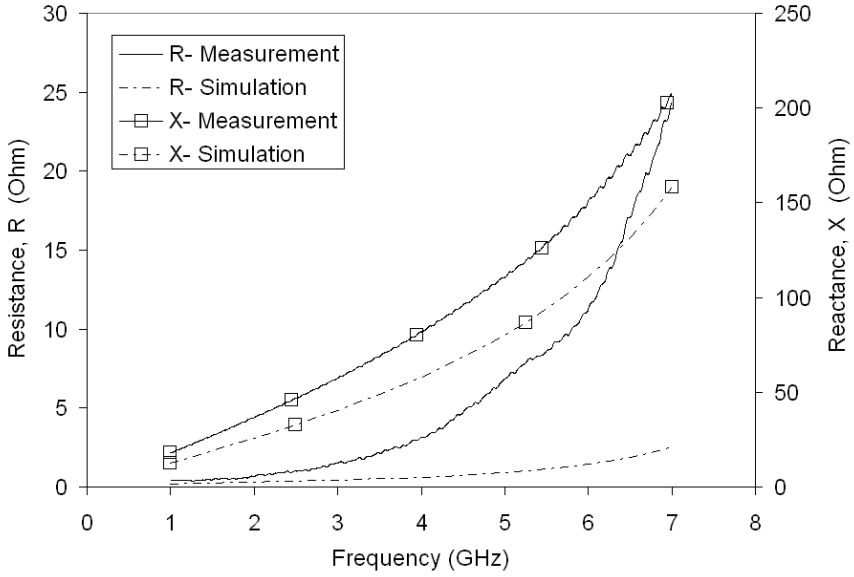

(a) Resistance and inductive reactance.

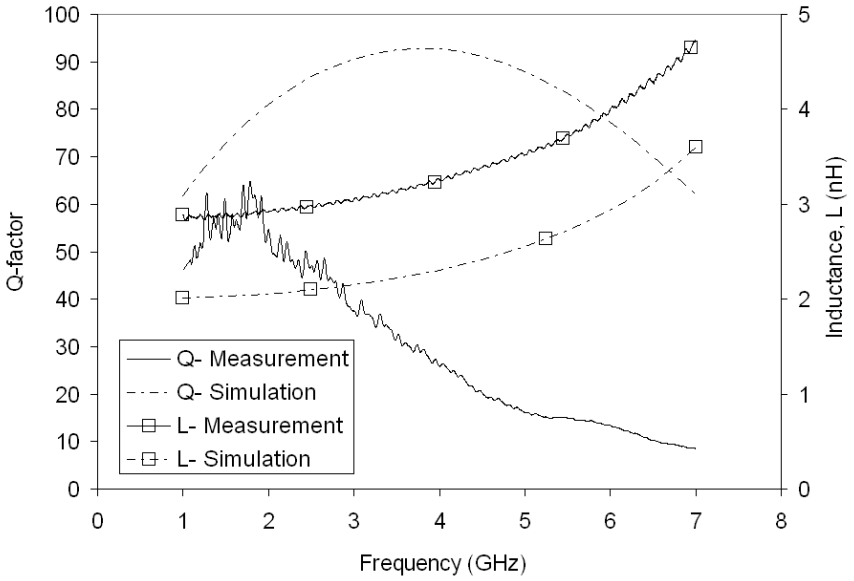

(b) Q-factor and inductance.

Figure B.3. Inductor parameters of large 1-loop inductor (gold on alumina).

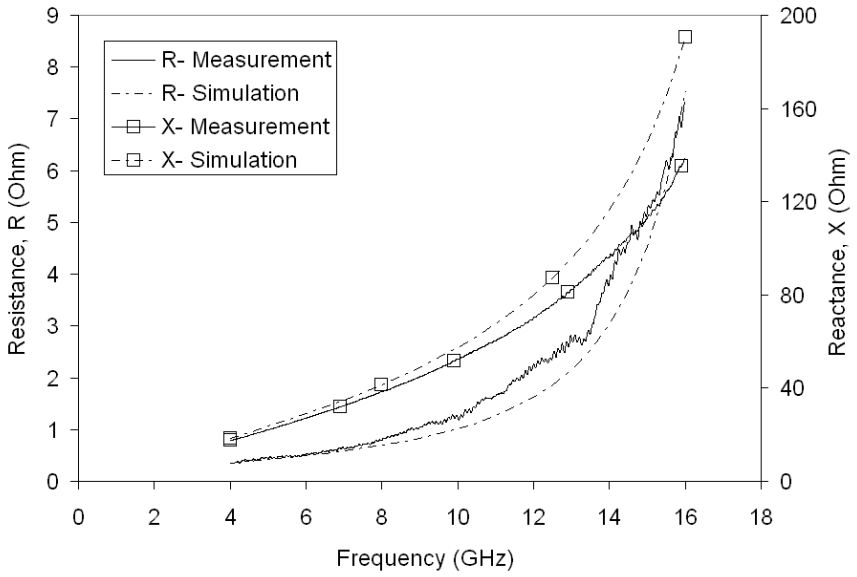

(a) Resistance and inductive reactance.

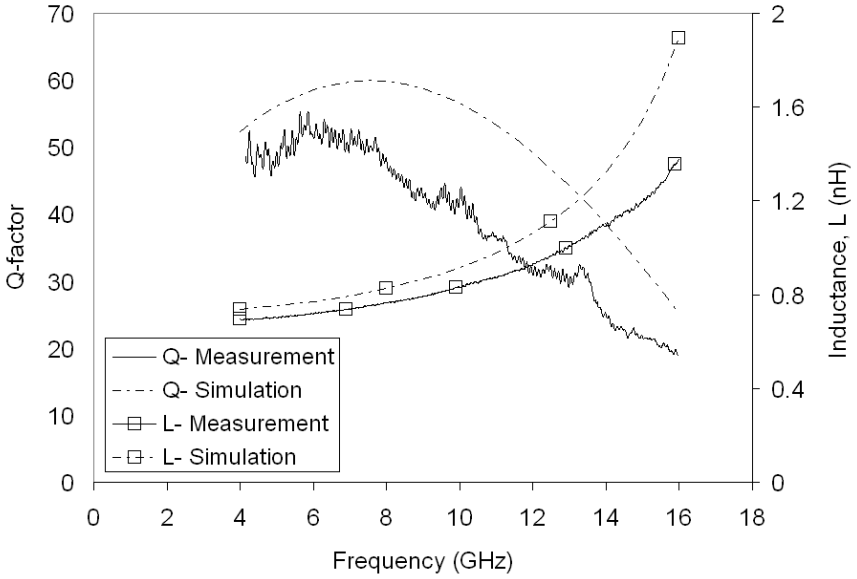

(b) Q-factor and inductance.

Figure B.4. Inductor parameters of small 2-loop (gold on alumina).

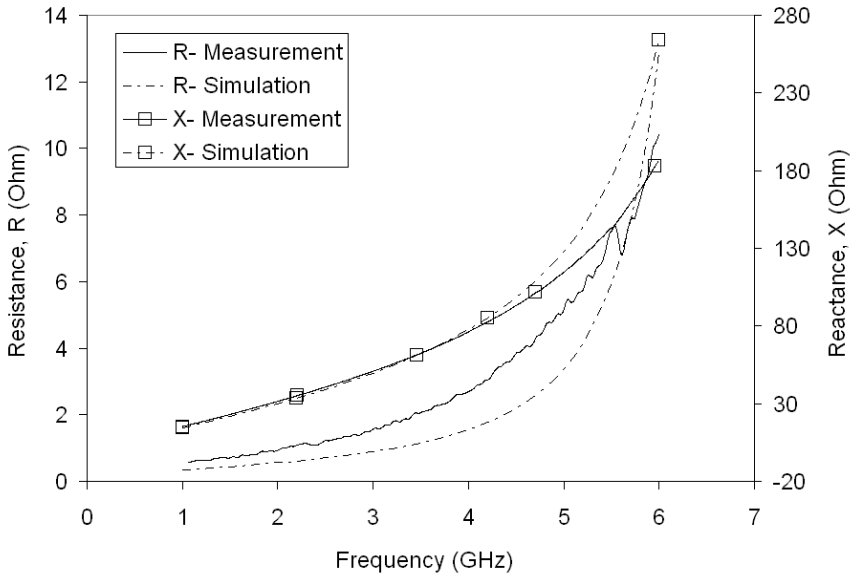

(a) Resistance and inductive reactance.

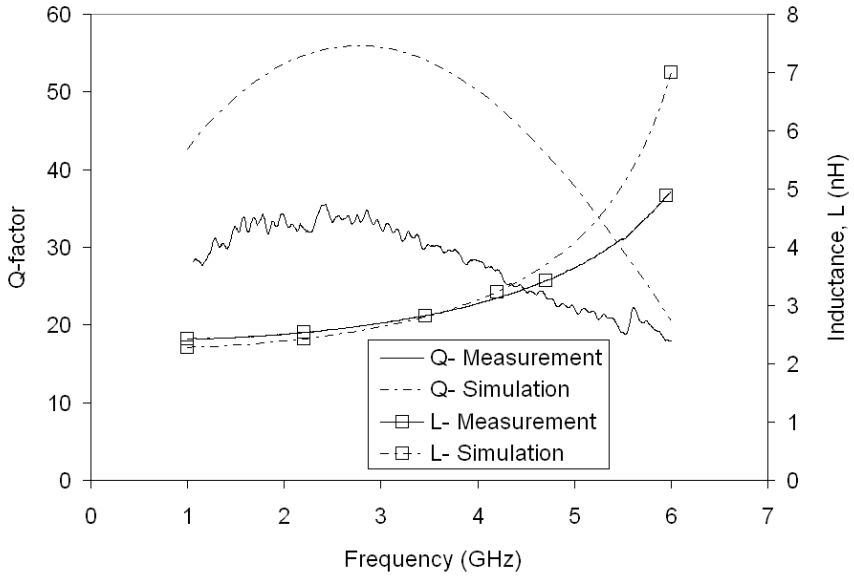

(b) Q-factor and inductance.

Figure B.5. Inductor parameters of medium 2-loop (gold on alumina).

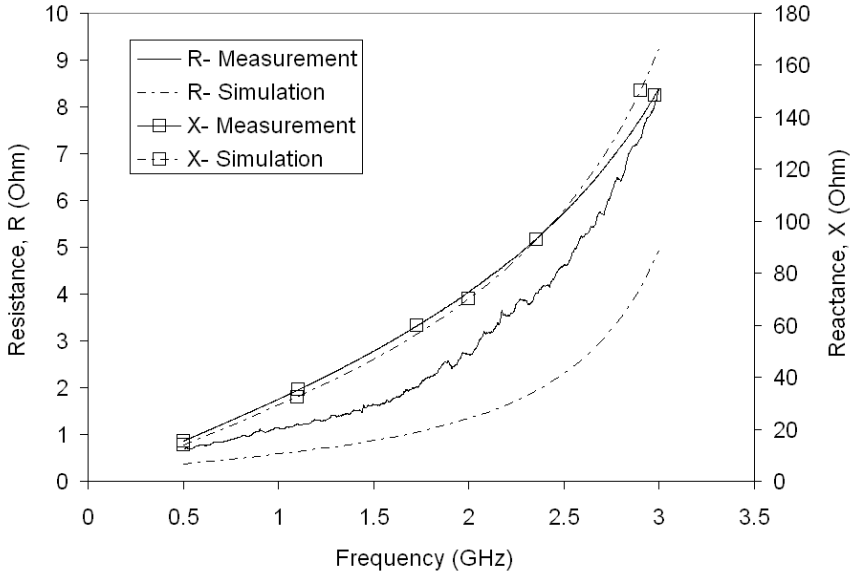

(a) Resistance and inductive reactance.

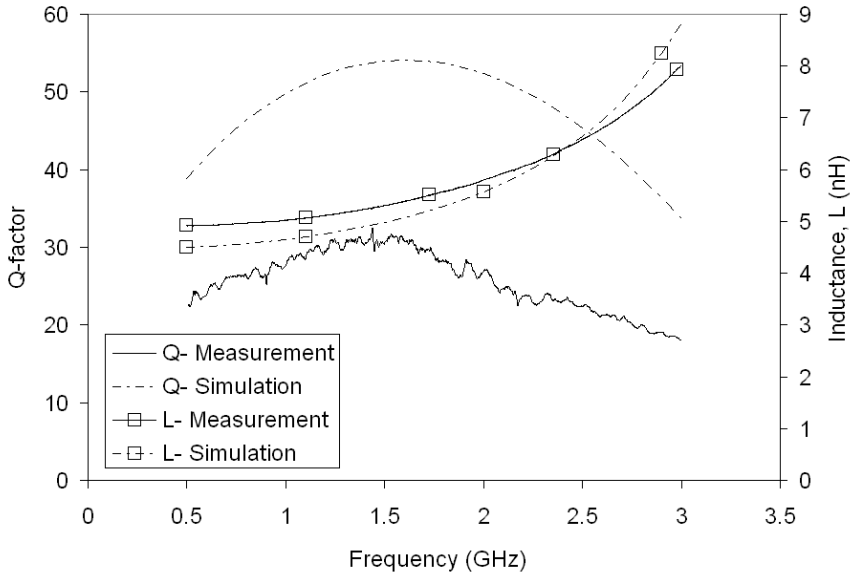

(b) Q-factor and inductance.

Figure B.6. Inductor parameters of large 2-loop (gold on alumina).

B.3 Inductor Parameters of 1-loop and 2-loop Inductors (Nickel on Quartz Glass)

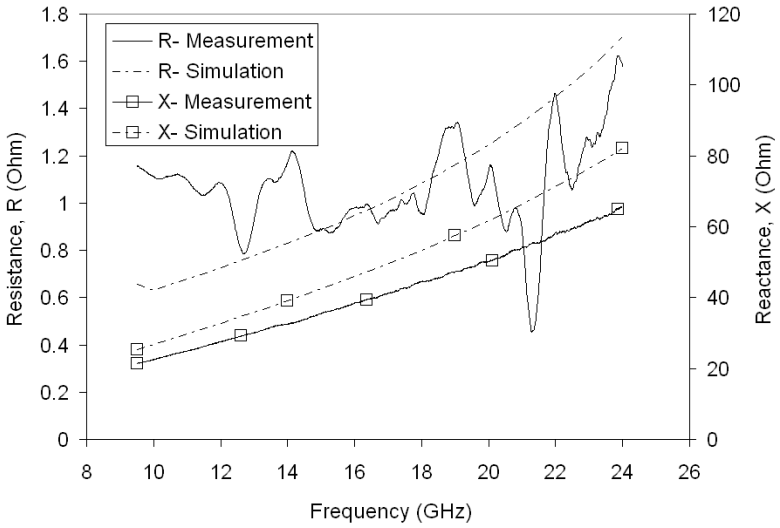

(a) Resistance and inductive reactance.

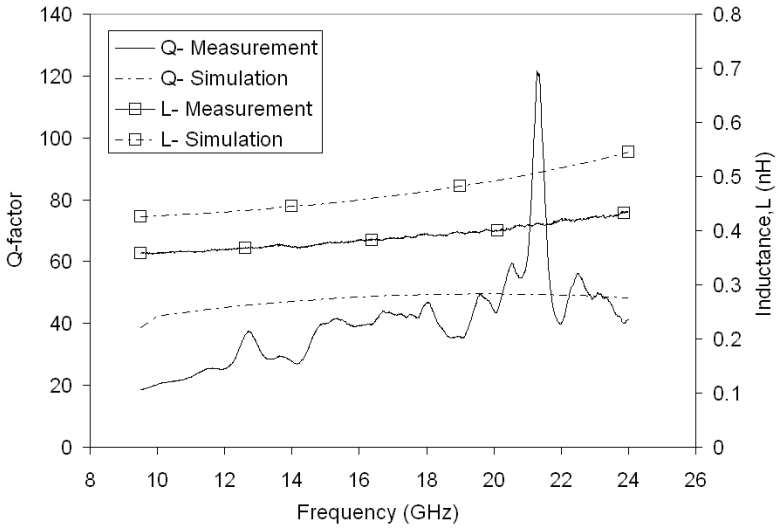

(b) Q-factor and inductance.

Figure B.7. Inductor parameters of small 1-loop inductor (nickel on quartz glass).

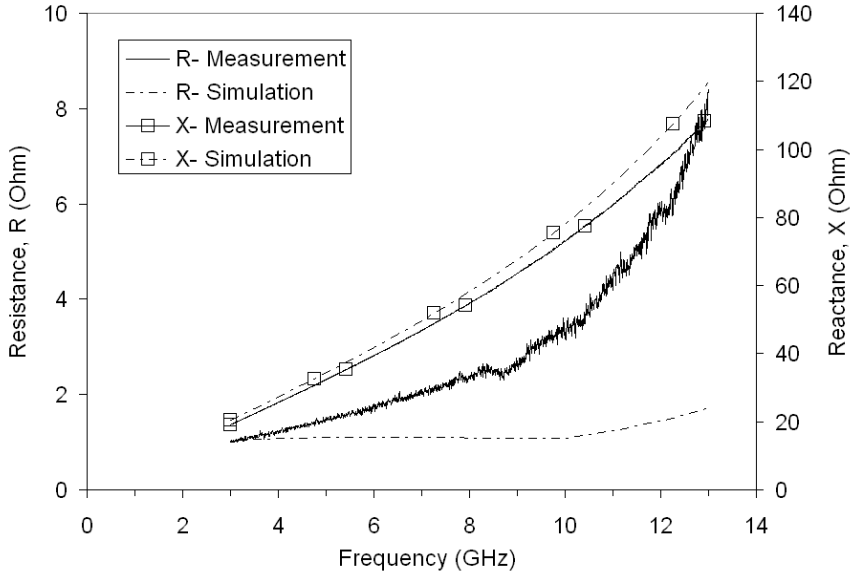

(a) Resistance and inductive reactance.

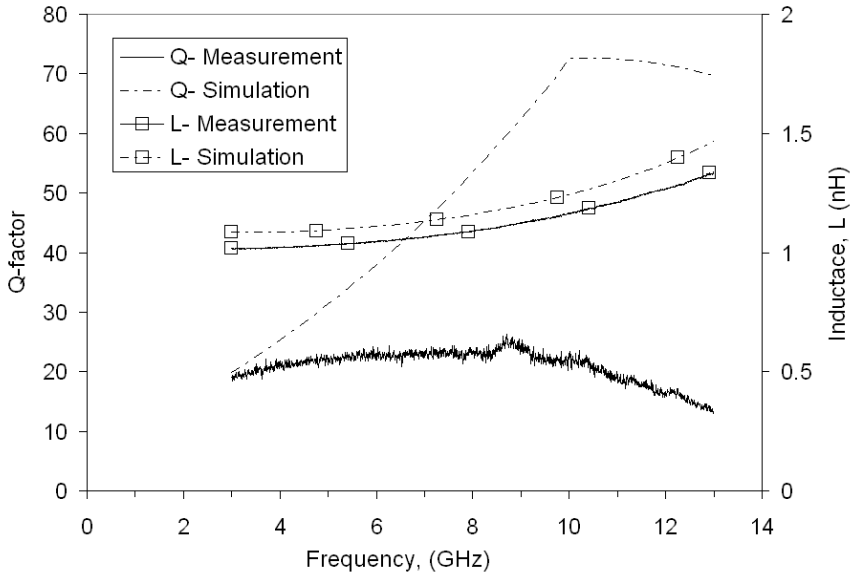

(b) Q-factor and inductance.

Figure B.8. Inductor parameters of medium 1-loop inductor (nickel on quartz glass).

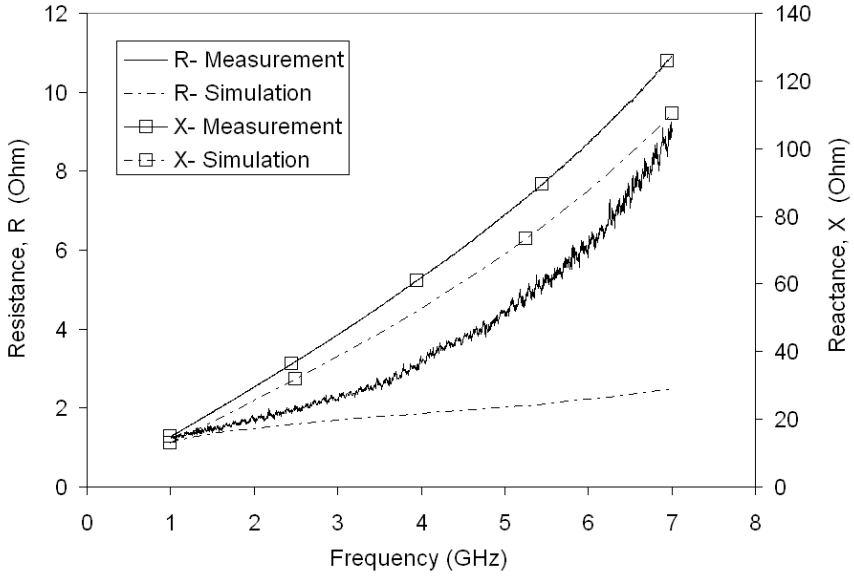

(a) Resistance and inductive reactance.

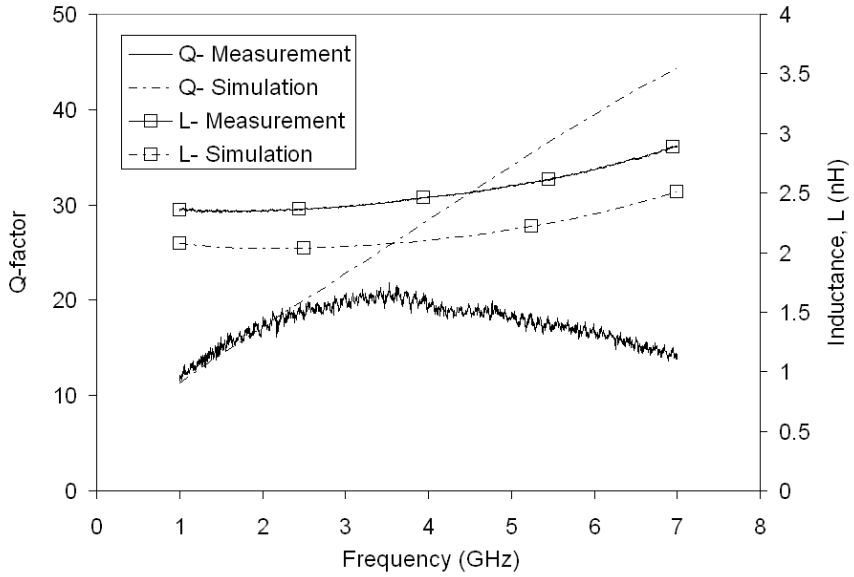

(b) Q-factor and inductance.

Figure B.9. Inductor parameters of large 1-loop inductor (nickel on quartz glass).

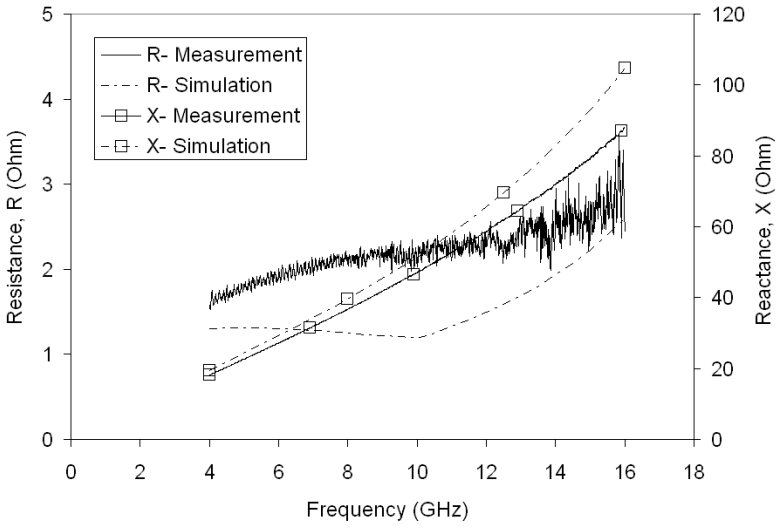

(a) Resistance and inductive reactance.

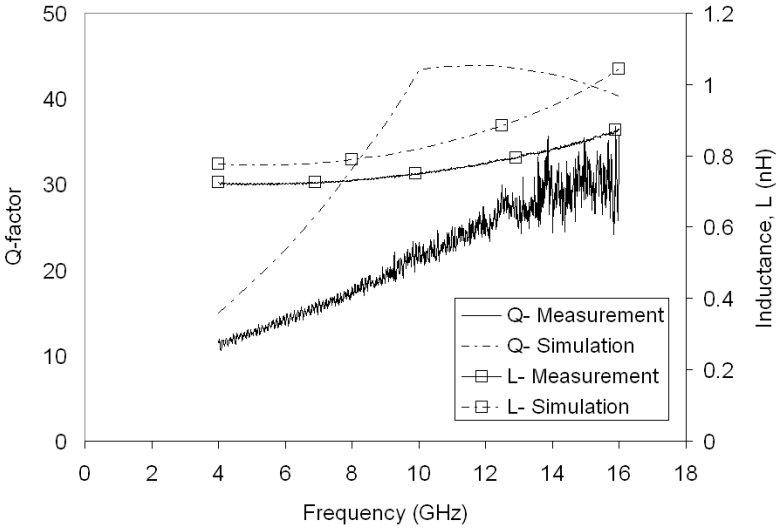

(b) Q-factor and inductance.

Figure B.10. Inductor parameters of small 2-loop inductor (nickel on quartz glass).

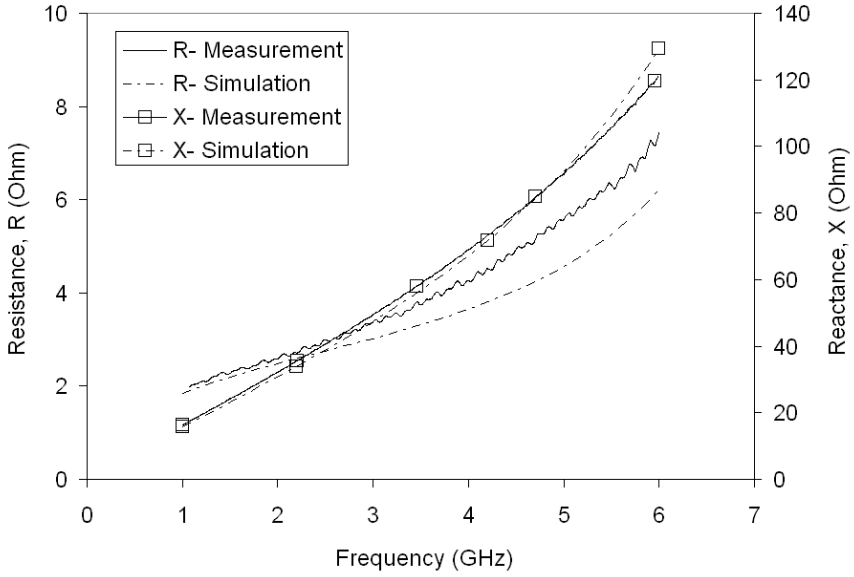

(a) Resistance and inductive reactance.

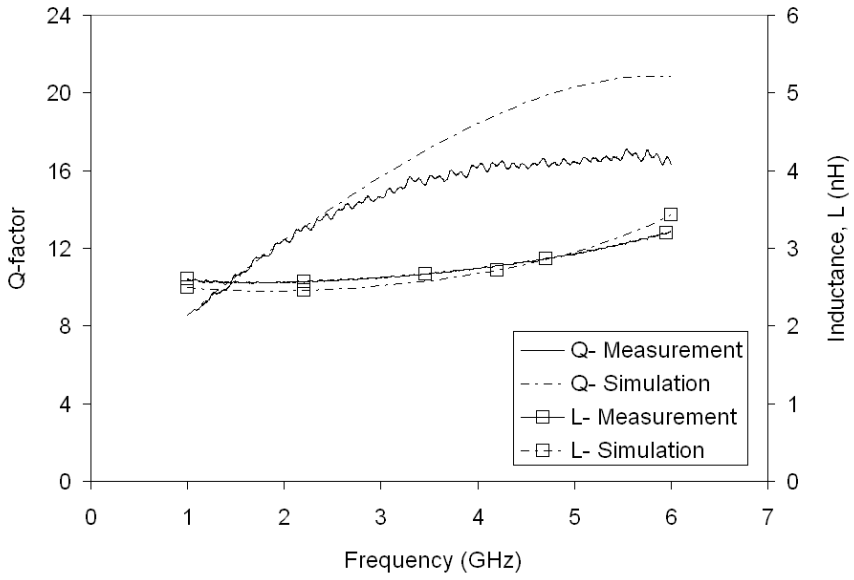

(b) Q-factor and inductance.

Figure B.11. Inductor parameters of medium 2-loop inductor (nickel on quartz glass).

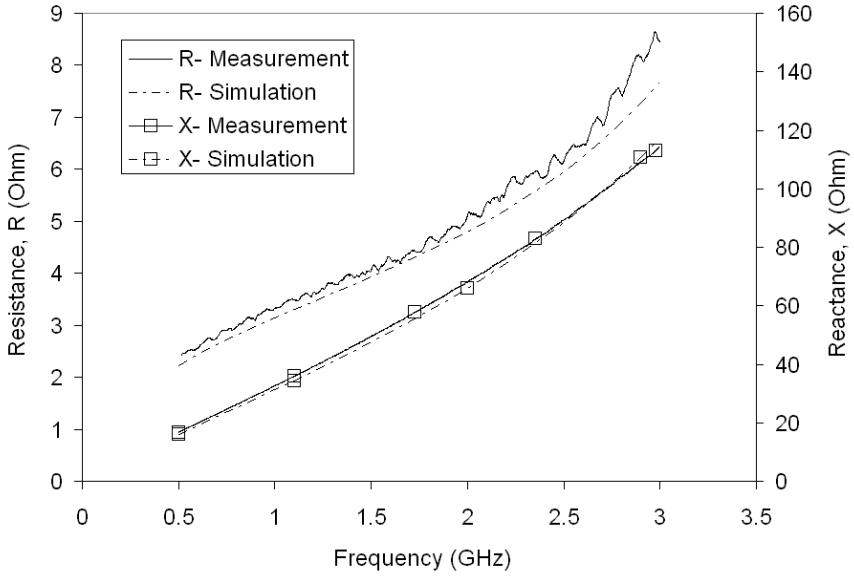

(a) Resistance and inductive reactance.

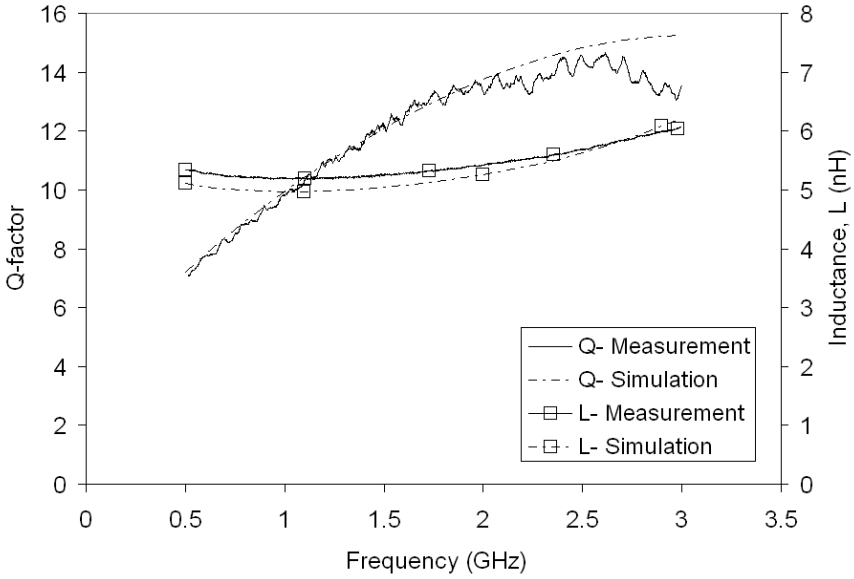

(b) Q-factor and inductance.

Figure B.12. Inductor parameters of large 2-loop inductor (nickel on quartz glass).

B.4 Comparisons of Small and Large inductors From Different Samples

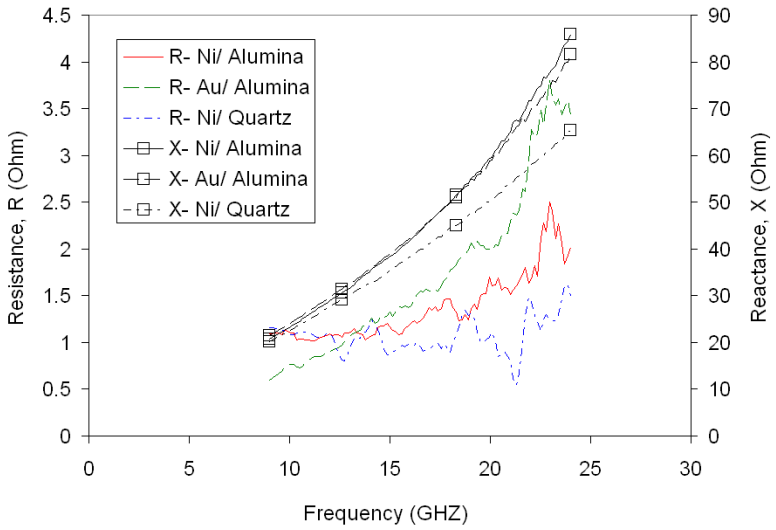

(a) Resistance and inductive reactance.

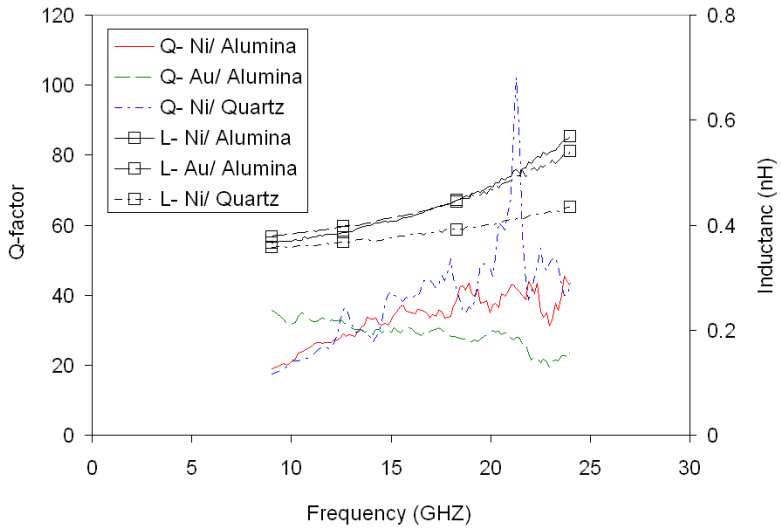

(b) Q-factor and inductance.

Figure B.13. Measured inductor parameters of small 1-loop inductors from different samples.

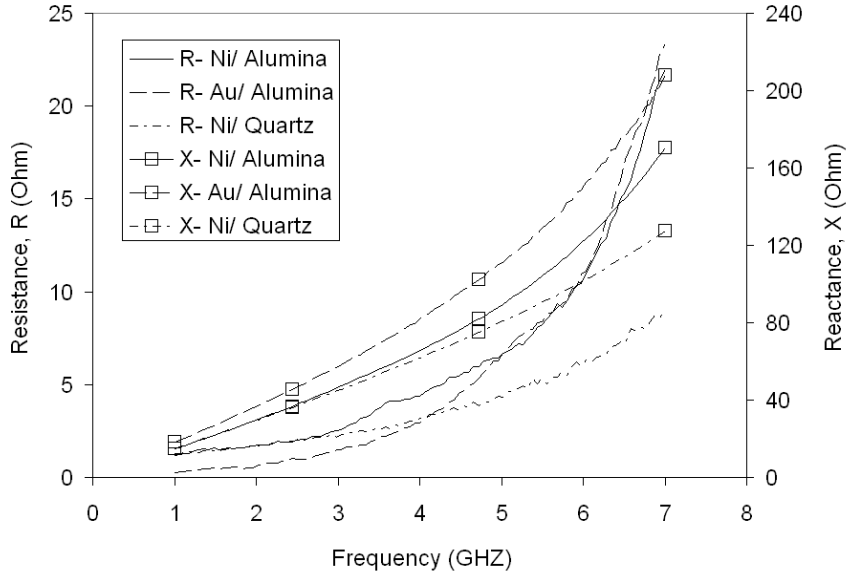

(a) Resistance and inductive reactance.

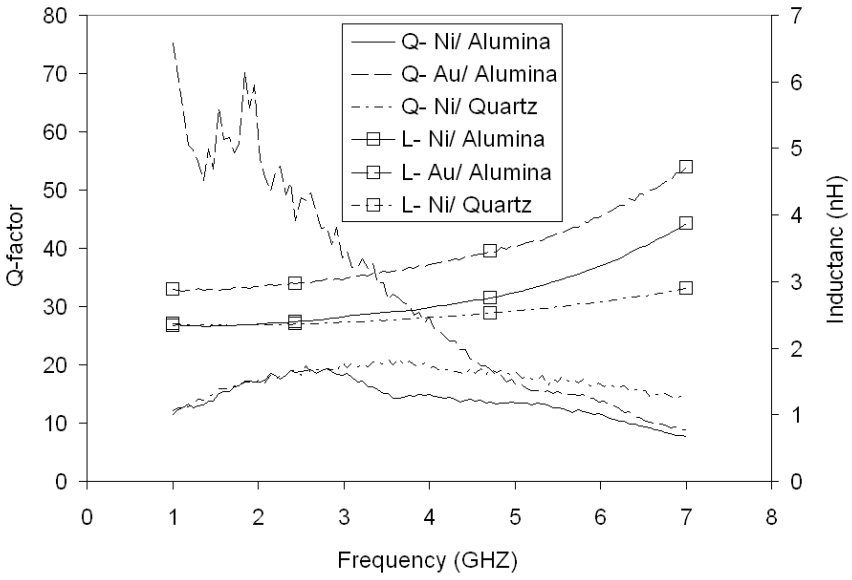

(b) Q-factor and inductance.

Figure B.14. Measured inductor parameters of large 1-loop inductors from different samples.

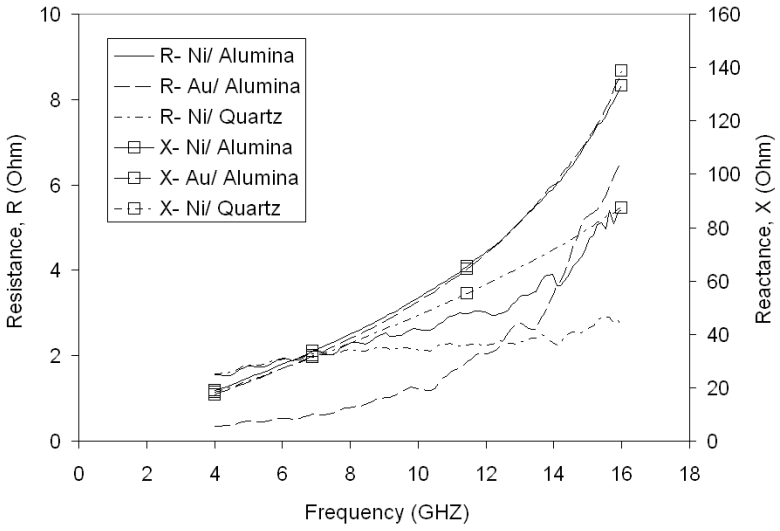

(a) Resistance and inductive reactance.

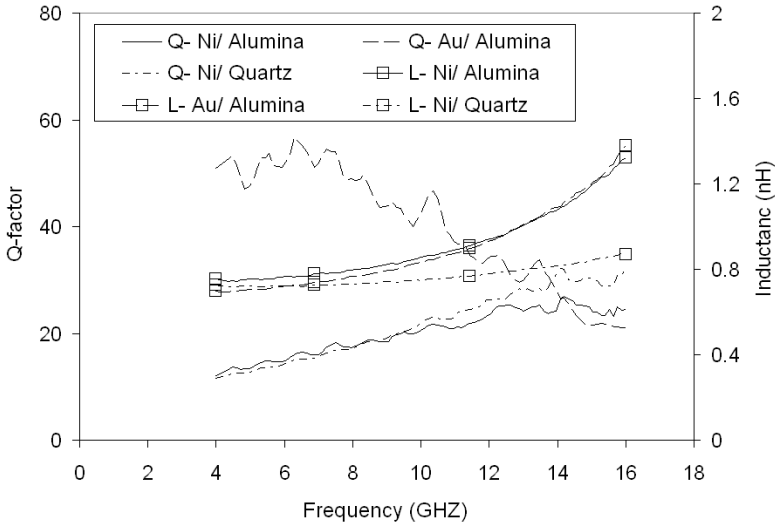

(b) Q-factor and inductance.

Figure B.15. Measured inductor parameters of small 2-loop inductors from different samples.

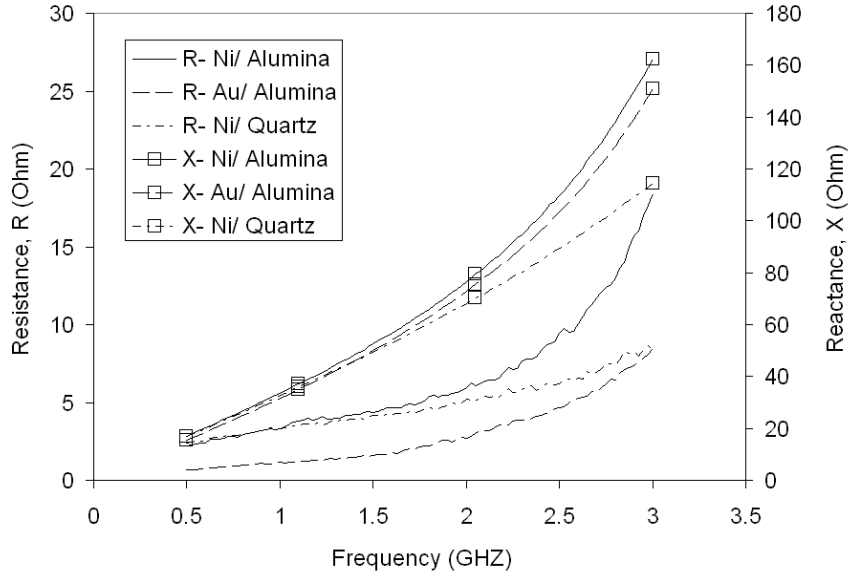

(a) Resistance and inductive reactance.

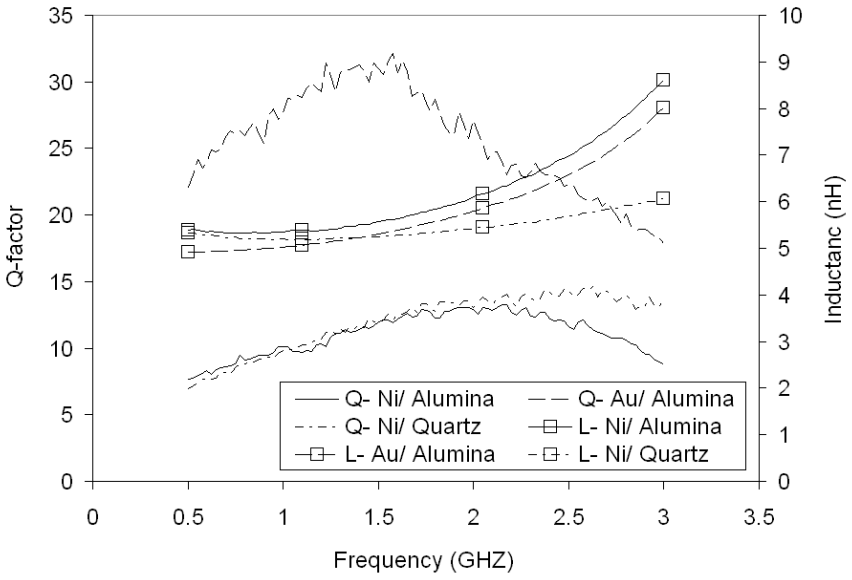

(b) Q-factor and inductance.

Figure B.16. Measured inductor parameters of large 2-loop inductors from different samples.